University of Nevada, Reno

Photoionized Neon Plasma Experiments at Z: Data Processing and Analysis Development

A thesis submitted in partial fulfillment
of the requirements for the degree of
Master of Science in Physics

by

Daniel C. Mayes

Dr. Roberto C. Mancini/Thesis Advisor

December, 2014

THE GRADUATE SCHOOL

We recommend that the thesis
prepared under our supervision by

DANIEL C. MAYES

Entitled

Photoionized Neon Plasma Experiments At Z:
Data Processing And Analysis Development

be accepted in partial fulfillment of the
requirements for the degree of

MASTER OF SCIENCE

Dr. Roberto Mancini, Advisor

Dr. Yasuhiko Sentoku, Committee Member

Dr. George Bebis, Graduate School Representative

David W. Zeh, Ph.D., Dean, Graduate School

December, 2014

Abstract

Photoionized plasmas are a special class of plasma common in astrophysical environments, such as x-ray binaries and active galactic nuclei, but they are a relatively unexplored regime of laboratory plasmas. This thesis discusses an experimental effort using the Z-Machine at Sandia National Laboratories to study the atomic kinetics in photoionized plasmas via K-shell line absorption spectroscopy. The experiment employs the intense x-ray flux emitted by the collapse of a Z-pinch to heat and backlight a neon photoionized plasma contained within a cm-scale gas cell placed at various distances from the Z-pinch and filled with neon gas with pressures in the range from 3 torr to 30 torr. High-resolution spectra show absorption by several ionization stages of neon, including Be-, Li-, He-, and H-like ions. A suite of IDL programs have been developed to process the experimental data to produce transmission spectra. Analysis of these spectra yields ion areal-densities and charge state distributions, which can be used to benchmark atomic kinetics codes. In addition, the electron temperature is extracted from level population ratios of Li- and Be-like ions, which can be used to test heating models of photoionized plasmas. Multiple aspects of the processing and analysis methods are tested to identify areas that show improvement or must be improved upon. These include the method of zero-level of absorption estimation, correspondence between known gas filling pressure and measurements totals, temperature extraction from Li-like and Be-like level populations, and the use of Voigt line profiles and Stark broadened line profiles to model the absorption spectra. Finally, we discuss trends visible in the analysis results.

Acknowledgments

First and foremost, I would like to thank my advisor, Dr. Roberto Mancini, for his continued support, guidance, and patience throughout this project. He has been a considerable influence in the way I approach problem solving and research, and he has taught me a tremendous amount. He is an excellent mentor.

To my Master's thesis committee members, Dr. Yasuhiko Sentoku and Dr. George Bebis, I extend my deepest gratitude for your participation in this endeavor and for your work in reading my manuscript.

Tom Lockard and Dr. Iain Hall have been essential to making these experiments happen and run smoothly in order to produce the data on which this thesis is based. I thank them for all of their hard work regarding these experiments. All of the scientists and technicians at Sandia National Laboratories with whom we collaborate, including Jim Bailey and Greg Rochau, also deserve my gratitude for making these experiments possible.

I want to also thank a long time mentor of mine, Professor Robert Collier, for inspiring me to pursue physics and astronomy. His encouragement and support throughout the years has led me to where I am. He has put me on the path that I am on.

Finally, without the support of my family and friends, none of this would have come to be. I thank my mom, dad, and sister for being awesome and always encouraging me to go further. My friends, I thank for everything they have ever been and for dealing with my incessant need to tell them about science. I also thank my girlfriend,

Lindsay, for being so understanding and supportive over the last few months so that I could complete this thesis.

This work is sponsored in part by the National Nuclear Security Administration under the High Energy Density Laboratory Plasmas grant program through DOE Grant DE-FG52-09NA29551, the Z Facility Fundamental Science Program, and Sandia National Laboratories.

Contents

List of Tables

List of Figures

Chapter 1

Introduction

In our everyday, earthly lives there are few naturally occurring plasmas. They are very extreme environments, as far as living things are concerned. Yet a large fraction of the material in the universe is in the form of a plasma. From the material of the stars to the ionized gases of the interstellar medium to the outer regions of Earth's atmosphere, plasmas are ubiquitous. When I was first introduced to the idea of a plasma in an astronomy class, it was described as "obliterated matter". This seems appropriate, since many of these environments are so energetic that even tightly bound electrons are ripped from their parent atoms; a hostile environment indeed, even for atoms. But plasma environments are also very complex and diverse, and thus present a wide range of challenges and possibilities for research. Plasmas have begun to benefit humanity in many ways in modern times, and will surely provide more benefits in the future as we strive to harness the power of the sun and much more. In our ever deepening quest to understand the universe in which we live, plasmas are a fundamental part of that understanding.

There are many different types of plasmas with conditions varying over enormous ranges, and there are many different ways that plasma environments can be created. The type of plasma this thesis will be concerned with are photoionized plasmas.

These are a special class of plasma created in the presence of a strong source of high-energy radiation. To be considered a "photoionized" plasma, as opposed to a "collisional" plasma, the density must also be low enough that the rate of radiation driven ionization dominates over electron collisional ionization [1].

Photoionized plasmas are observed in many different places throughout the universe. For example, they are observed in planetary nebulae [2,3], active galactic nuclei (AGN) [3], and x-ray binary systems [4] to name a few. To begin the process of understanding these systems, astronomers record x-ray spectra using space telescopes, such as the Chandra X-Ray Telescope and XMM-Newton. Atomic kinetics codes, such as Xstar [5], Cloudy [6], or Galaxy [7] can then be used to try to replicate the spectra in order to determine the conditions inside the system. There are also atomic kinetics codes that were developed for modeling laboratory plasmas, such as PrismSpect [8], Spect3D [9], and Cretin [10], that can also be used similarly. Though, due to the extreme nature of this type of plasma and the difficulty in creating it, there is a dearth of experimental data for validation of atomic kinetics codes that deal with photoionization; therefore, these codes are based only on theoretical models.

To help remedy this problem, an experimental platform utilizing a Neon gas filled cell has been developed for use on the Z-Machine (Z) at Sandia National Laboratories (SNL) in Albuquerque, New Mexico within the Z Astrophysical Plasma Properties (ZAPP) collaboration to produce benchmark data to test these codes [11, 12]. ZAPP [13] is a collaboration of four experiments all dedicated to advancing our understanding of astrophysical plasmas where radiation is an important player. Each experiment uses the intense radiation created by a Z-pinch to irradiate a sample of material. Besides the Neon photoionized plasma experiment on which this thesis is focused, there are two other experiments that use the radiation emitted from the side of the Z-pinch. One of these is also focused on studying photoionization, but this

experiment uses a silicon foil. The second of these aims to study the plasma in the photospheres of white dwarf stars, and it uses a larger, Hydrogen filled gas cell placed further from the pinch and irradiated by the re-radiation of a gold coating [14]. The fourth experiment in this collaboration uses the radiation emitted from the top of the Z-pinch to irradiate a tamped iron/magnesium foil. This experiment aims to study stellar opacities [15].

In the past, there has been a few other experiments done in effort to begin investigating the regime of photoionized plasmas [16–18] [19, 20] [21]. These experiments were limited to producing only single points within the relevant irradiance versus density space that affects the ionization parameter value. However, the Neon gas cell experiments on Z allows for the exploration of trends within this space.

A useful parameter for characterizing photoionized plasmas is the "ionization parameter", ξ. It was originally defined in the 1960's as [22]

$$\xi = \frac{L}{Nr^2} \tag{1.1}$$

where L is the luminosity of the "small", central radiation source with the spectral shape of thermal bremsstrahlung of temperature T_X, N is the uniform particle number density of the medium (i.e. photoionized plasma) with "cosmic" elemental abundances, and r is the distance from the source.

The ionization parameter is meant to reflect the competition between photoionization and recombination for a photoionized plasma in equilibrium [22]. But it can also be considered to represent "the degree of over-ionization caused by the radiation [in a photoionized plasma], relative to the ionization characteristic of a collision-dominated plasma" [1]. Due to the low density characteristic of this type of plasma, the amount of collisional recombination would be reduced allowing the radiation driven ionization to raise the average ionization of the plasma. Being that the collisional ionization rate

would also be reduced due to the low density, the plasma would appear over-ionized from the standpoint of collisional atomic kinetics alone.

For the purpose of laboratory experiments, the ionization parameter can be rewritten as

$$\xi = \frac{4\pi I}{N_e} \tag{1.2}$$

in terms of the irradiance $I = L/4\pi r^2$ and the electron number density N_e [11]. Note that the usage of N in Equation 1.1 has the assumption of cosmic abundances, which means that the majority of the particles are Hydrogen, and therefore $N_e \approx N$. However, in the experiments this is not the case, and it is important to specify that the denominator is actually the electron number density.

As a first step to producing useful benchmark data, one must first have a clear understanding of the experiments and how they apply. Namely, the plasmas being created in these experiments must first be well characterized. The radiation fields, densities, and temperatures in the experiments must be measured and understood. There must also be an understanding of non-uniformities, time-dependence, and the various things that cause the experiments to stray away from the ideal case. Along with this, it is important to understand what effects these have on the relevance of the experiments to simulations that are done with the different atomic kinetics codes, and vice versa. One must also gain an understanding of the atomic kinetics codes themselves, what assumptions they make, and where they are and are not applicable. This is the phase that this experimental campaign is currently in.

This thesis will be focused primarily on the development of processing and analysis methods for use with the data from these experiments. There will be results shown, but I must stress that these are measurement results extracted mainly from the results of testing the various processing and analysis methods that have been developed. They do however begin to give an idea of the properties of the plasmas

being created in the these experiments. To begin, Chapter 2 will provide an overview of the experiment, and it will discuss how the data is recorded and what effects there are on the data from various components in the experiment. Chapter 3 will discuss the methods and the suite of programs developed in the Interactive Data Language (IDL) during the course of this project to handle the processing and reduction of the experimental data. Details of the analysis methods explored will be discussed in Chapter 4. A sampling of results will be given and discussed in Chapter 5. Finally, Chapter 6 will conclude this thesis.

Chapter 2

The Experiment

In this chapter, the details of the experiment will be discussed. The chapter begins with a brief history of the Z-Facility and its capabilities. This is followed by a description of the experiment and some history regarding that. Beginning with Section 2.4, the experimental setup and the spectrometer used to collect data are discussed. Finally, components within the light path and their effects on the data are discussed.

2.1 Z-Machine

The Z-Machine at Sandia National Laboratories (SNL) in Albuquerque, New Mexico is the world's most powerful laboratory radiation source. It was originally constructed as the Particle Beam Fusion Accelerator II (PBFA II) for the Light Ion Fusion Program, taking its first shot in 1985 [25]. It was modified in 1996 from its previous configuration to enable pulsed power Z-pinch experiments for further fusion research and other high-energy density physics applications. In this configuration, renamed "PBFA II-Z" and later simply "Z", it was designed to deliver up to 20 MA of current to a cylindrical wire array containing a few hundred thin Tungsten wires. With this, Z was capable of producing x-ray peak powers of more than 200 TW [26] [27]. A

(a)

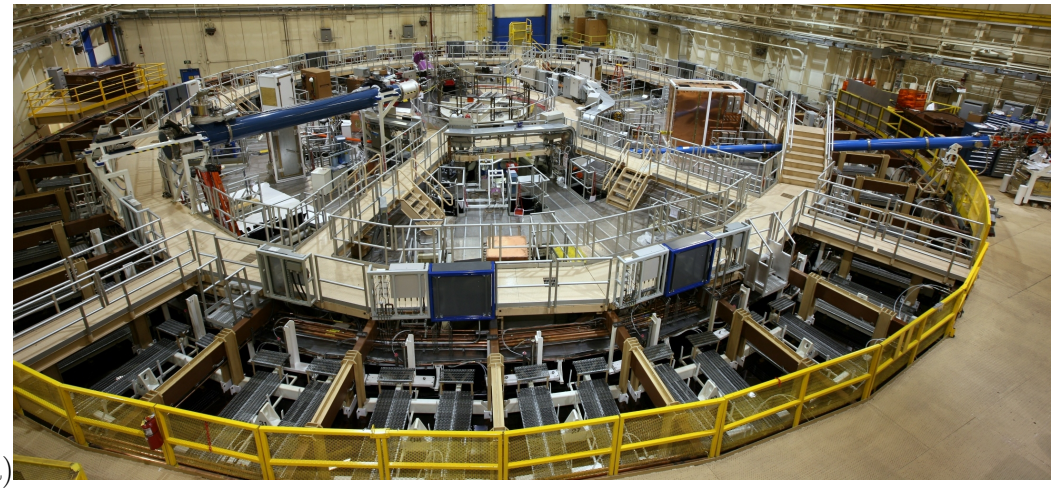

(b)

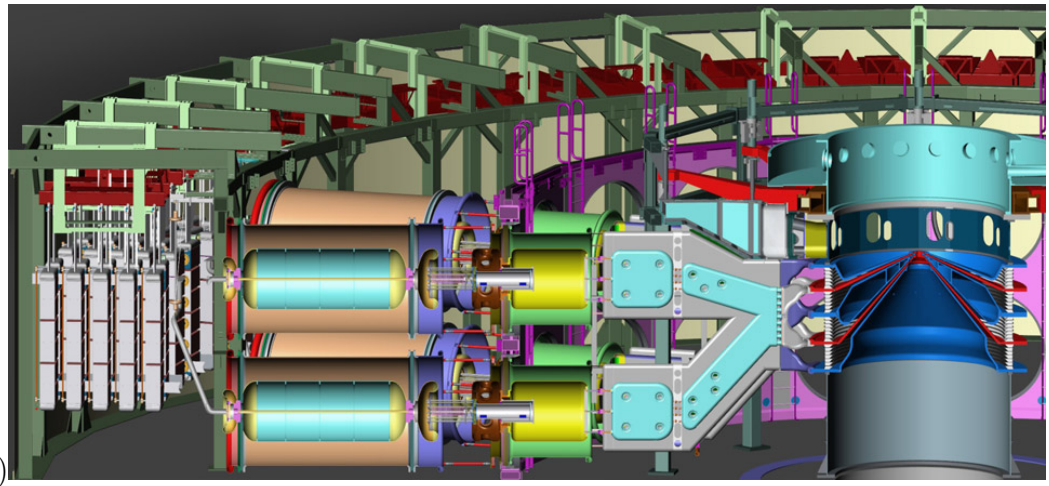

Figure 2.1: (a) The Z-Machine [23]. (b) Cross-section of the Z-Machine [24]. Beginning from the left, there are the *Marx bank generators*, which initially store the energy. The energy is discharged into the *intermediate store-capacitors* (salmon and cyan colored), which effectively compress the electrical pulse in time, increasing the current and reducing the current rise-time. These are dumped by *laser-triggered gas switches* into the *pulse-forming line* (green and yellow), which are another set of capacitors that compress the pulse further. These are discharged through *self-break water switches* (grey and cyan), through the *vertical to horizontal convolute* outside the vacuum insulator and into the *magnetically insulated transmission lines* (blue and red), which deliver the current to the wire-array load at the center of the Z chamber.

refurbishment of Z completed in 2007 upgraded it to deliver 26 MA of current to the wire array increasing the x-ray peak power to around 300 TW [28].

As the current flows through the wire array, they heat up and begin to turn into a plasma. This is the ablation phase. A large azimuthal magnetic field is created around the array by the current flow, and the $J \times B$ force causes the mass of the wires to accelerate in toward the central z-axis of the array. The mass is accelerated to supersonic speeds during this implosion or run-in phase. These first two stages correspond to the approximately 100 ns current rise-time. In the final stage of the Z-pinch implosion, collapse and stagnation, the wire mass arrives at the central z-axis where the kinetic energy from the inward motion is converted to heat and radiation. This results in an x-ray burst which can release energies of around 1.8 MJ and peak powers of 300 TW. The full width at half max (FWHM) of this burst in time is typically around 6 ns [11, 28, 29].

The wire array used in this experiment is made up of 360, 11.5 μm tungsten wires arranged in two cylindrical nest arrays. The inner array is 20 mm in diameter and contains 120 wires, and the outer array is 40 mm in diameter and contains 240 wires. At the center of the array, a 6 mm diameter, 12 mm tall, 14.5 mg/cc foam cylinder is placed on axis.

2.2 Photoionized Plasma Experiment

This experiment utilizes the intense, broadband x-ray radiation field created from the side of the Z-pinch to drive a Neon photoionized plasma. To do this, a metal gas cell is set a few centimeters away from the central axis of the Z-pinch. See Figure 2.2 for a cartoon illustrating the arrangement of the gas cell with respect to the Z-pinch in the experimental setup. The gas cell has two windows along the radial direction to allow radiation to propagate through the cell. The “front” window is on the side closest to

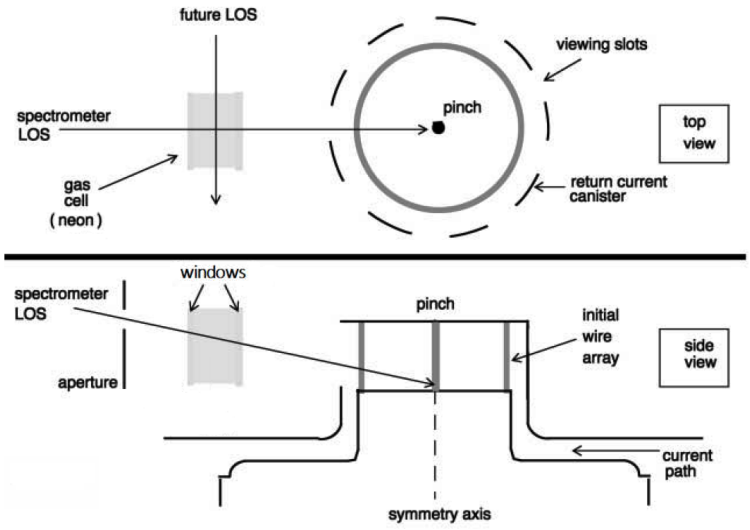

Figure 2.2: Illustration depicting a top view and side view of the experimental setup [11]. The gas cell is placed a few centimeters from the pinch axis with windows and an aperture along the LOS. The spectrometer's LOS through the gas cell to the pinch is 12° from horizontal.

the central axis, and the "rear" window is on the opposite side of the gas cell toward the spectrometer. This gas cell is filled with neon gas of a given pressure. There are two distances that can be used to place the gas cell, which affects the intensity of radiation reaching the gas cell. There is a spectrometer looking along the line of sight (LOS) through the windows of the gas cell directly at the Z-pinch. This spectrometer uses two x-ray crystals to simultaneously observe two sets of spectra. There is a set of six slits associated with each crystal that creates six separate spectra in each set for a total of twelve spectra. Each set of spectra can then be recorded independently by two different types of detectors or by two detectors of the same type.

The first proof of principle experiment to demonstrate that this would work was described in Ref. [11]. Since that time, the experiment has evolved and has gone through multiple improvements. The set of experiments before June 2011 are referred to as the first generation (GEN1) of experiments, while experiments from June 2011

and after are referred as the second generation (GEN2) of experiments.

2.3 Radiation Field

The radiation field produced by the Z-pinch plasma is approximately Planckian. Therefore, the radiation field at the surface of the Z-pinch plasma can be approximately characterized by a radiation temperature T_R. The Planck function B_ν describes the distribution in frequency ν of photons radiated by a blackbody of temperature T_R.

$$B_\nu(T_R) = \frac{2h\nu^3}{c^2}\frac{1}{\exp(h\nu/kT_R) - 1} \tag{2.1}$$

where h is Planck's constant, c is the speed of light, and k is Boltzmann's constant. This is the energy radiated from a surface per unit time per unit area per solid angle per unit frequency. The total thermal radiation flux F (i.e. total thermal energy radiated per unit time per unit area) is obtained by integrating B_ν over all frequencies and over solid angle, as emitted from a small unit of surface.

$$F = \int_0^\infty B_\nu d\nu \int_{2\pi} \cos\theta d\Omega = \pi \int_0^\infty B_\nu d\nu \tag{2.2}$$

where the solid angle is integrated over half the sphere and $\cos\theta$ is included because the intensity falls off as the cosine of the angle from the surface normal. Performing this integral gives the Stefan-Boltzmann Law, which tells that F is proportional to the fourth power of the temperature.

$$F = \sigma T_R^4 \tag{2.3}$$

where σ is the Stefan-Boltzmann constant [30].

The gas cell, however, is located some distance away from the Z-pinch. This means

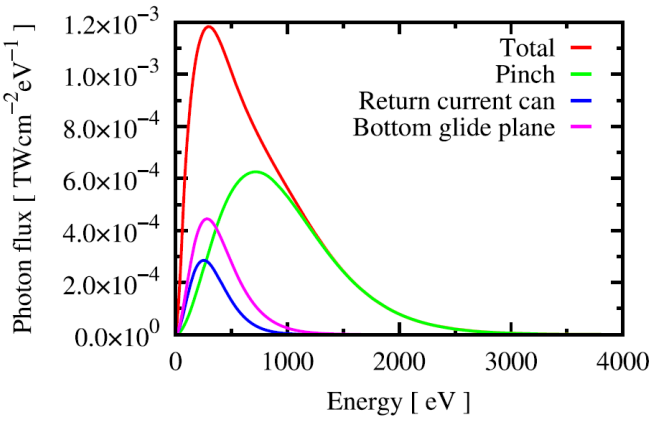

Figure 2.3: Contributions to the radiation drive seen by the gas cell at the time of peak emission [31].

that the radiation field as seen by the gas cell would be a diluted Planckian, which can be described by two temperatures, the color temperature T_C and the brightness temperature T_B. T_C relates to the placement of peak of the Planck function in frequency, and therefore $T_C = T_R$ always. The dilution effect reduces the intensity of the Planck function with distance and is captured in T_B, where $T_B \leq T_C$. Of course, at the surface of the pinch, $T_C = T_B = T_R$. The total thermal energy radiated per unit time per unit area F_B for the diluted Planckian is

$$F_B = \sigma T_B^4 = \kappa \sigma T_C^4 = \kappa F, \tag{2.4}$$

where κ is a scaling factor relating the total power flux of the Planckian at the pinch surface with that of the diluted Planckian. It follows that

$$\kappa = \left(\frac{T_B}{T_C} \right)^4. \tag{2.5}$$

There have been efforts to characterize the radiation field as seen by the gas cell using the VisRad view-factor code [32]. This was done for earlier experiments (GEN1)

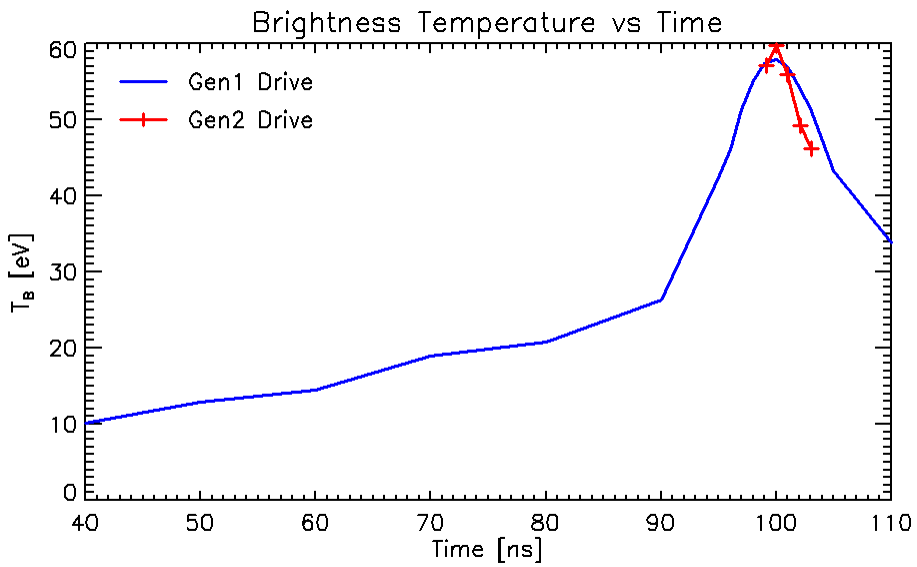

Figure 2.4: Time history of brightness temperatures for the radiation drive from GEN1 [31] and GEN2 [33] experiments calculated from a VisRad model.

by [31] and for later experiments (GEN2) by [33]. Even though the Z-pinch is the main contributor, it is not the only source of radiation that contributes to the x-ray flux reaching the gas cell. The hardware surrounding the Z-pinch also heats up and re-radiates during the experiment contributing more at lower photon energies. VisRad allows for this to be included. Each component is assumed to radiate as a Planckian and the sum of the contributions gives the total radiation field as viewed from some position, which is not necessarily Planckian. A breakdown of the contributions can be seen in Figure 2.3. The effective color temperature T_C, relates to the spectral distribution of the radiation field and is determined from the location of the peak of the distribution in frequency space. The effective brightness temperature T_B is found by integrating the total radiation flux F_ν in a similar manner as in Equation 2.2 by replacing B_ν with F_ν and then using Equation 2.4 to extract T_B.

A history of T_B over the course of an experiment is shown in Figure 2.4. The peak of the drive is located at 100 ns in time. The drive for the GEN2 experiments has been

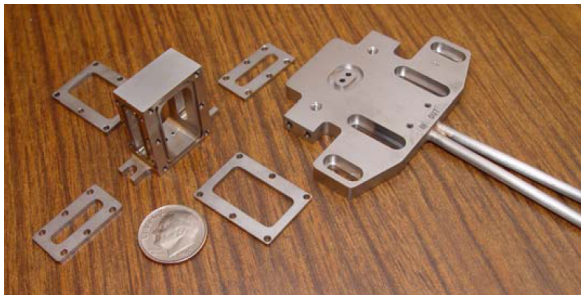

Figure 2.5: A gas cell in pieces (old design).

shifted in time to match the peak of the GEN1 drive. The information here for the GEN2 experiments' drive is limited due to data from extra constraints from images of the Z-pinch that were included to improve the calculation. One can see that the peak values of T_B are similar for both (58 eV for GEN1 and 60 eV and GEN2); however, the color temperatures are different (103 eV for GEN1 and 62 eV for GEN2). This difference is primarily due to larger openings in the return current canister in the GEN2 experiments, which would allow more of the lower energy, re-radiated x-rays to get to the gas cell, reducing the overall color temperature.

2.4 Gas Cell

The basic design for the gas cell that is used today was developed at SNL for the proof of principle discussed above [11]. It is constructed from stainless steel and is machined in the machine shop of the Physics Department at the University of Nevada, Reno. Figure 2.5 shows an older gas cell design (we do not currently use side windows) laid out in pieces on a table, and Figure 2.6 shows a GEN1 style gas cell mounted in Z-Machine chamber. The gas cell consists of the main cell body of dimensions $1 \times 2 \times 2.34$ cm (LOS depth $\times$ width $\times$ height), which is attached to a baseplate. The baseplate is how the gas cell is secured in place in the Z-Machine chamber. Gas fill tubes are also mounted in the baseplate, which allows the gas cell to be filled and

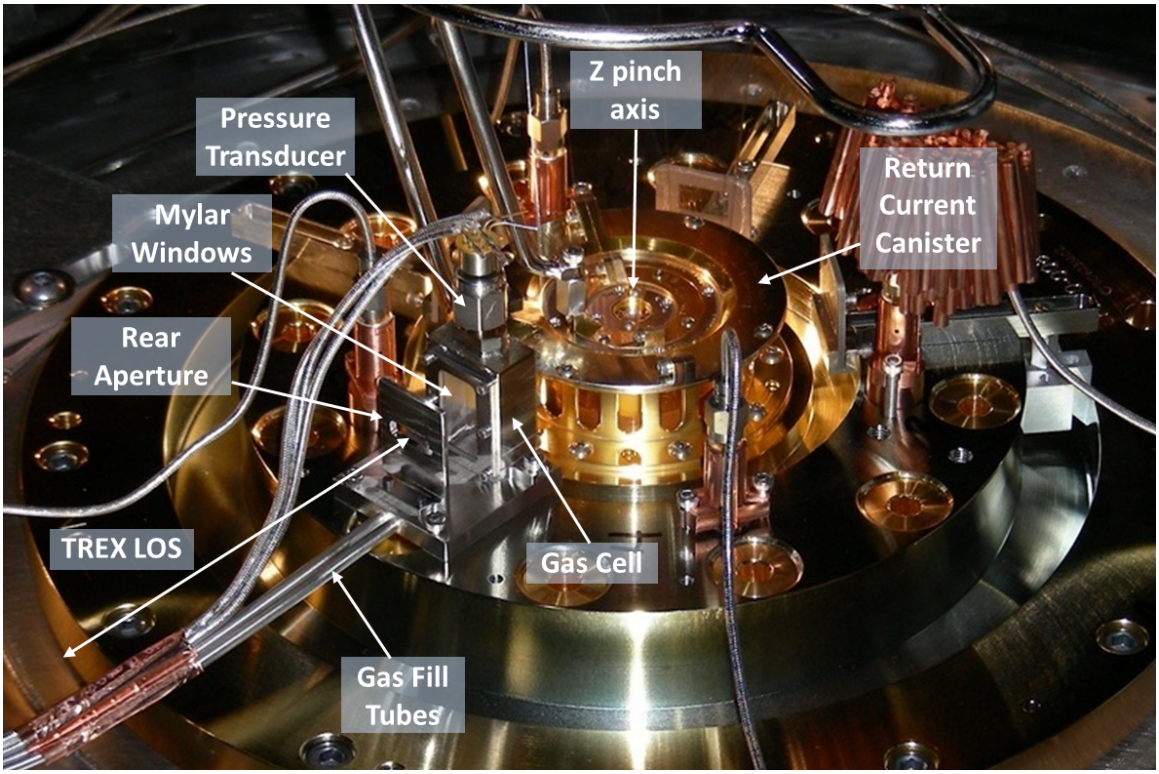

Figure 2.6: An GEN1 style gas cell with Mylar windows in the close position in the Z Machine chamber.

purged in-situ by a fill station located outside the Z chamber. The fill station has two pressure sensors, one on the input line and another on the output line connecting to the gas fill tubes. In addition, a port for a pressure transducer is welded to the top of the main body of the gas cell. This transducer outputs a variable voltage that relates to the pressure inside the gas cell and this produces an independent pressure measurement from that of the fill station.

Two window frames, in the GEN1 style, were used to secure Mylar windows in place. In the newer GEN2 setup (see Figure 2.7), Si_3N_4 windows are epoxied into place in depressions in window plates, which are mounted to the sides of the main gas cell body. O-rings are used between each mounting interface to make the gas cell vacuum tight. There is also an aperture plate mounted to the baseplate behind the gas

Figure 2.7: GEN2 Gas cell with the newer Si_3N_4 windows.

cell, with respect to the pinch, in order to limit the field of view of the spectrometer.

The gas cells are assembled and pressure tested at SNL before being installed into the Z-Machine chamber for a shot. They are pressure tested in a small vacuum chamber to check for leaks and to calibrate the pressure transducer. Once installed into the Z chamber, the cell is filled and purged several times (see Figure 2.8) in order to make sure that only neon gas remains in the system, to check that the cell is not leaking, and that the pressure sensors and fill station are working properly.

As was mentioned above, Mylar windows were used for the gas cells in the past during the GEN1 experiments. 1.5 μm Mylar was stretched over the entire extent of each face of the cell body, and it was secured in place by the window frame and O-ring. This left the whole area on each side of the gas cell open for radiation to pass through the Neon gas. Some problems with the Mylar include the following. The windows often leaked or broke, especially with the higher filling pressures. They also would bow outward substantially while it was pressurized in the vacuum chamber. This contributes uncertainty to the column length of gas along the LOS, which is an important parameter to be well known and reproducible. Additionally, the lower transmission of Mylar relative to that of Si_3N_4 reduces the radiation drive seen by

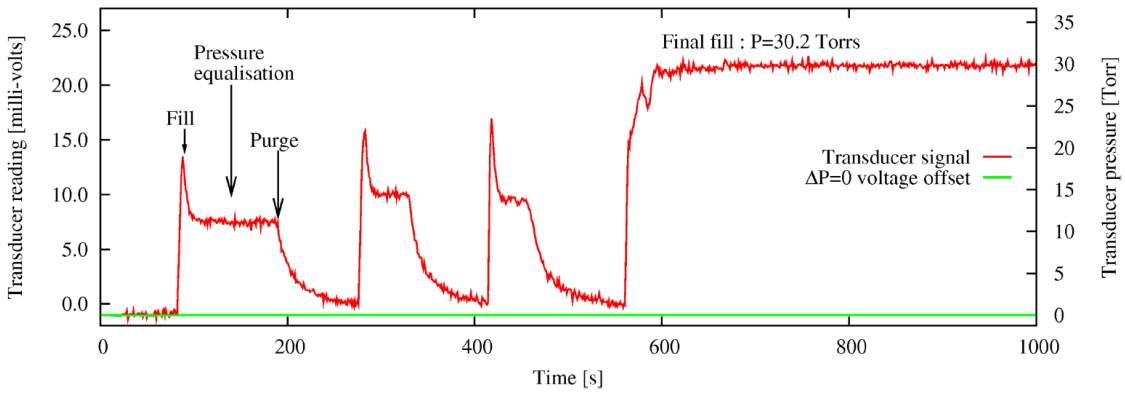

Figure 2.8: Before filling the gas cell to the desired pressure, it is filled and purged several times to make sure that only neon gas remains in the system and to check that everything is working properly. Then the gas fill pressure is monitored up until shot time.

the neon gas, and its behavior during heating adds more uncertainty to the problem of how much radiation flux is passing through the Neon gas. This will be discussed in more detail below. Another issue relates to the fact that when the radiation drive interacts with the windows, they are turned into a plasma and subsequently will expand rapidly. This compresses the Neon gas inside the cell and it sends shock waves through the gas. This adds still another level of uncertainty to experimental parameters.

A solution to some of these issues was found in the prospect of using the Si_3N_4 windows shown in Figure 2.7. These windows are smaller in area, more rigid, and much thinner (i.e. 50 to 75 nm) than the Mylar. As received, they consist of a Silicon frame with the Si_3N_4 material attached to it. The frame is a 10×10 mm square that is 200 μm thick with a 5×5 mm opening in the center. Attached to one side of the frame is a 10×10 mm square of Si_3N_4 material. These are epoxied into place, with the Si_3N_4 material out, in a similarly sized depression in each gas cell window plate, which also has a 5×5 mm opening machined in the center. Their size and rigidity prevents them from bowing out as the Mylar did. Since the LOS to the spectrometer

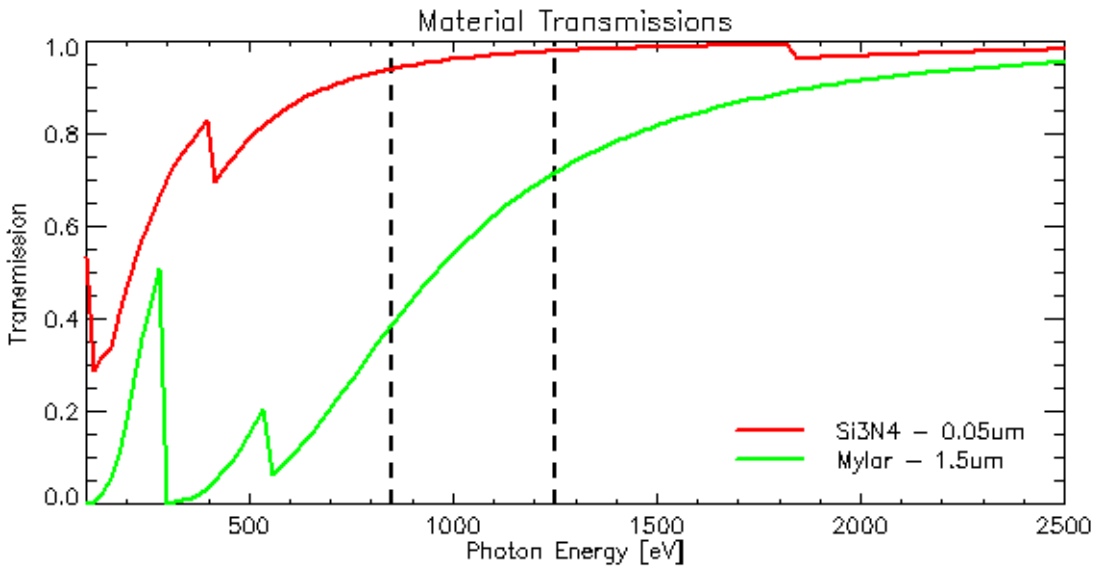

Figure 2.9: Material transmissions versus photon energy of 50 nm of Si_3N_4 (red) and 1.5 μm of Mylar (green) at room temperature [34].

is at a 12° angle to the horizontal, the front and back windows are offset in the vertical direction to accommodate this. The fact that these windows are much thinner means that they are also much less massive (i.e. ∼10 times less mass per unit area than Mylar) and therefore, that their expansion should have less influence on the Neon during the experiment.

Another benefit is in the transmission. Figure 2.9 shows a comparison of the room temperature transmissions as a function of photon energy for 1.5 μm of Mylar in green and 50 nm of Si_3N_4 in red [34]. The vertical dashed lines indicate the spectral range of the spectrometer for reference. As can be seen, the transmission of the Si_3N_4 is much higher all across the spectrum, so more of the radiation drive will get to the neon gas, at least while the Si_3N_4 is cool. Figure 2.10 shows two calculations done by Ref. [35] using the LASNEX code [36]. These show the time dependent, total photon energy integrated transmission in red for (a) Mylar and (b) Si_3N_4 as they are heated by the Z-pinch radiation drive, shown as the side power in blue. The transmission

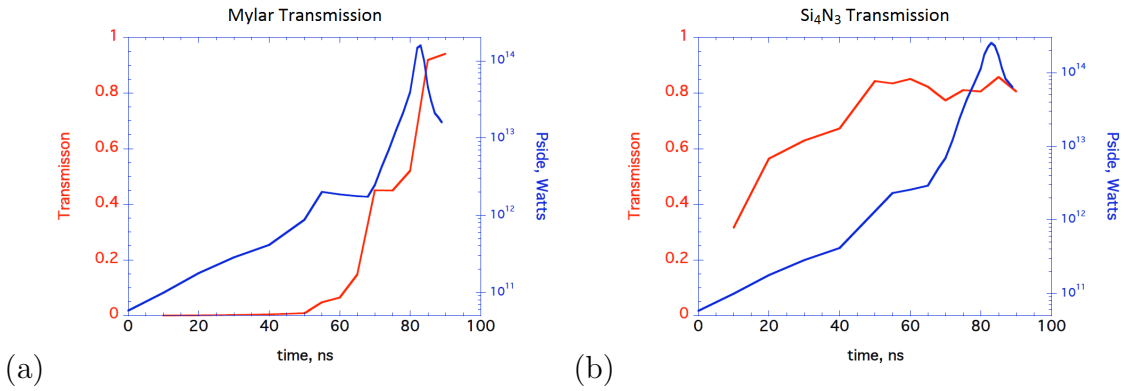

Figure 2.10: Total photon energy integrated transmission of (a) Mylar and (b) Si_3N_4 windows while they are heated during a shot [35].

of Mylar rises quickly late in time and tops off after the peak of the drive. Whereas the transmission of Si_3N_4 rises early on and becomes relatively stable near 80% long before the peak of the drive, providing a much better idea of how much radiation is making its way through the window to drive the neon gas.

For lower filling pressures (i.e. 15 torrs or less), 50 nm thick Si_3N_4 windows can be used, but for the higher pressures, such as 30 torr, 75 nm thick windows must be used. Unfortunately, there is still the issue of windows occasionally leaking or breaking. But in going to the Si_3N_4 windows at least three sources of uncertainty have been reduced, namely relating to the column length of Neon gas, perturbations due to the expansion of the windows, and the x-ray transmission through the windows. A fourth area that these Si_3N_4 windows affect is in the source of the radiation throughout the extent of the gas cell. It was mentioned in Section 2.3 that when the pinch goes off, there is re-radiation from the surrounding hardware. This can have a large effect on the radiation drive seen by the gas inside the cell. Since these Si_3N_4 windows are much smaller in area than the old Mylar windows, they also act as apertures to restrict the source of radiation. At the front of the gas cell, there will be some contribution to the radiation drive from the re-radiation of the hardware, but further in the gas

cell, more of the radiation field will be from the pinch alone due to the limiting view of the front window. This may create some extra uncertainties, since the radiation field changes over the extent of the gas cell length, but the radiation field is restricted more to only that of the Z-pinch.

There are a few parameters that can be varied in the experiment in order to explore different plasma conditions. These parameters directly affect the ionization parameter ξ in a few ways. Recall from Equation 1.2 that

$$\xi = \frac{4\pi I}{N_e}, \tag{2.6}$$

where I is the irradiance and N_e is the electron number density. N_e can be related to the Neon ion number density N_i by $N_e = \bar{Z}N_i$, where $\bar{Z}$ is the average ionization. There are two different distances where the gas cell can be mounted inside the Z-Machine chamber. The front window of the gas cell can either be at 4.3 cm or 5.9 cm from the central axis of the Z-pinch. This effectively changes the radiation field intensity incident on the neon gas, affecting the numerator of ξ.

The filling pressure can also be changed to affect the denominator of ξ. At this point, approximately an order of magnitude in number density has been explored in this series of experiments. Earlier experiments concentrated on higher filling pressures, including 30 torr, 15 torr and 7.5 torr, which correspond to Neon number densities of roughly 10^{18} cm^{-3}, 5×10^{17} cm^{-3}, and 2.5×10^{17} cm^{-3} respectively. More recently shots using 3.5 torr and 2 torr (i.e. 1.1×10^{17} cm^{-3} and 6.5×10^{16} cm^{-3} respectively) have been attempted. With lower filling pressures, the uncertainty in the pressure increases. A new method of measuring the pressures that has recently been developed by Ref. [37] may show that these lowest pressures were not quite as low as originally hoped. The above two ways of varying the value of ξ allows for the investigation of trends in the properties of photoionized plasmas as a function of ξ,

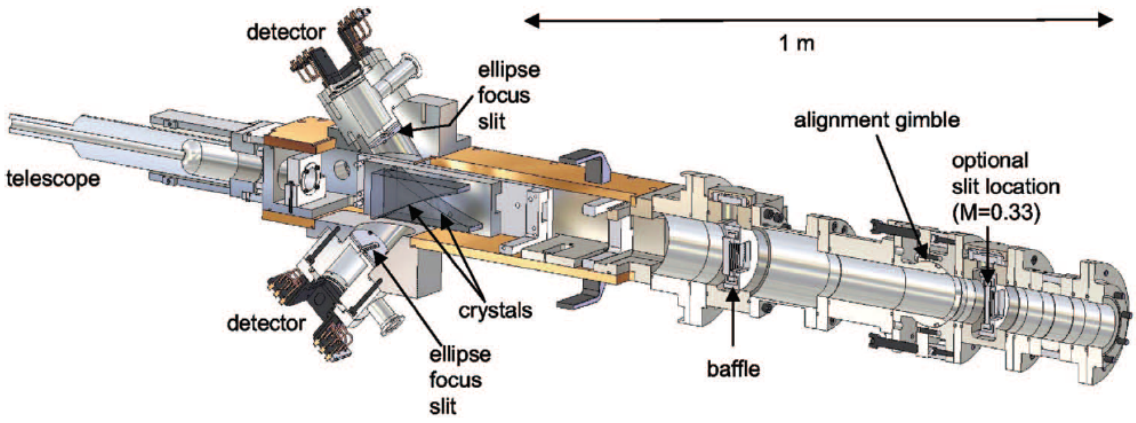

Figure 2.11: Twin elliptical x-ray crystal spectrometer (TREX) [39].

as well as trends as a function of irradiance and number density. A third way of similarly investigating trends with regard to ξ is to vary both the irradiance and the number density simultaneously while keeping ξ constant.

Experiments involving mixtures of Hydrogen and Neon have also been tried. This more closely mimics (1) the astrophysical scenarios where these plasmas exist, since Hydrogen is ubiquitous in space, and (2) the required input for astrophysics atomic kinetics codes, since they usually require or assume that Hydrogen is present.

2.5 TREX Spectrometer

The spectrometer that is used is a twin elliptical x-ray crystal spectrometer and has the capability of being both time- and space-resolved [38, 39]. It is called the TREX spectrometer and can be seen in Figure 2.11. The spatial resolution is not utilized because the spectrometer view is limited to the central area of the Z-pinch by the aperture behind the gas cell and by the smaller size of the windows for GEN2 gas cells. The spectrometer is located about 4 meters from the Z-pinch and the LOS is angled at about 12° from the horizontal.

For the spectral range of interest for the Neon, Potassium Acid Phthalate (KAP)

crystals are used, which gives the spectral range between approximately 850 to 1250 eV in photon energy with a resolution power of about 1000. During a shot, there is the potential for debris to make it up into the spectrometer and damage the crystals and other equipment even though it is 4 meters away, so protection from this is important. At the front end of the spectrometer, at the location marked as "optional slit location" in Figure 2.11, a filter of Mylar is placed to help block possible debris. Further up the spectrometer shaft, at the "baffle" location, the two sets of slits are placed, which can also help to prevent debris from getting too far into the TREX. The slits are oriented with respect to the x-ray crystal so that the light transmitted through each slit is later diffracted along the length of that slit image. The orientation of the TREX also means that the slits are oriented parallel with the Z-pinch. Often times, there is extra filter of Kimfol attached to the slit plate covering two of the slits. This is discussed in more detail in Section 2.6. Occasionally, debris will still make it past this point, in which case it might damage the x-ray crystals since they are the next components in the light path. The crystals are oriented such that the spectra from each are directed toward opposite sides of the TREX spectrometer. The top side is generally referred to as "side a" and the other is "side b". This allows for two independent detectors to be associated with each set of spectra. Since the crystals are elliptically bent, they have two foci, one located at the Z-pinch and the other near the crystal, on the way to the detector. The latter is shown in Figure 2.11 as the "ellipse focal slit". There is one for each crystal. It is also referred to as the "crossover" slit and is perpendicular to the dispersion axis of the crystals. At this point, there is an aluminized Lexan filter attached to the detector housing. These act as light tight filters for the detectors during transport between the film processing area and the Z-Machine. This along with the small aperture of the crossover slit helps further protect the detectors from possible damage.

There are two choices for what type of detectors to use on each side. One option is to use a piece of Kodak RAR 2492 x-ray film [40, 41]. In this case, time-resolution is forfeited, so a time-integrated measurement is obtained spanning the whole duration of the experiment. The other option is to use a micro-channel plate (MCP) detector [38, 42, 43], which can be used to obtain spectra with time-resolution. The MCP detector consists of many small channels that amplify a signal of light in a similar manner as photomultiplier tubes. On the back side of the array of channels, electrons impinge upon a phosphor plate, which scintillates releasing visible light, which is then captured by a recorder. In this experiment Kodak TMAX 400 black and white film is used. The MCP is coated with six gold strips to which a bias voltage can be applied, allowing the device to capture separate images at different times from each strip. Since two detectors can be used on the TREX, a given experiment can use either two of one type of detector, or one of each type.

At the end of the TREX, there is a telescope that is used for pointing the spectrometer. Between the slit plates and the crystals, there is an alignment crosshair which indicates where the center of the spectrometer shaft is pointing. This crosshair creates a small absorption-like feature in the spectra. This feature does not appear in precisely the same place in photon energy in every shot and in each spectrum, so is of no use there, but it should be noted that it is visible. The crosshair, as visible from the telescope view, is aligned with the center of the foam cylinder at the center of the wire arrays during the preparation for a given shot.

2.6 The Light Path

Between the time that the Z-pinch collapses and releases the radiation drive to when that light is incident on the detector, the light interacts with several components. These interactions need to be taken into account during the processing and analysis

of the data to accurately characterize the plasma. In this section, the light path and the effects of the elements within it on the radiation drive and spectral data are discussed.

The first thing that the radiation drive interacts with is the front window of the gas cell. Some of the radiation drive will be absorbed here and won't make it into the Neon gas. The window will also be heated and turn into a plasma, which will cause it to expand, while the transmission of the window material also changes as it is heated. The radiation that makes it through the front window will then interact with the Neon gas. This is the radiation drive that actually drives the photoionized plasma. As was discussed in Section 2.4, the radiation field changes in both intensity and spectral shape with distance through the cell; therefore, the radiation drive seen by the gas at the front edge of the cell is different from that seen by the gas at the rear edge. Next, this radiation must pass through the rear window. This window will also be heated, turned into a plasma, and will similarly expand as did the front window. When each window expands, it does so not only in the outward direction with respect to the gas cell, but they also expand inward into the Neon gas, compressing and sending shocks through the gas. This is an important thing to consider in these experiments, and some hydrodynamic simulations have been done in the past by Ref. [31], and some newer simulations are being run by [44]. These simulations have shown that around the time of the peak of the drive while the majority of the backlight radiation is propagating through the gas cell, much of the region inside the neon gas ($\sim$80%) is still unperturbed by the expansion and shocks.

The aperture behind the gas cell, as well as the smaller Si_3N_4 windows, limits the field of view of the spectrometer to the central portion of the gas cell and Z-pinch. This helps reduce any contribution to the recorded spectrum from re-radiation from the experiment hardware. It also helps to block debris, which could enter the

spectrometer and cause damage.

Following this, the radiation propagates toward the TREX spectrometer. The first thing it reaches in the TREX is the 1.5 μm Mylar filter near the front of the spectrometer. This is now far enough away that the radiation does not change the properties of the filter during the experiment. After this, are the slits. Each slit is 50 μm in width and about 4 cm in length. The slits separate the incoming light into six thin lines of light, each of which will end up producing a slit spectrum at the detector. For time-integrated measurements, two of the slits are covered with an extra filter of Kimfol material attached to the slit plate. The purpose of this extra filter is to provide a second measurement of the spectrum having a different ratio of contributions from 1^{st} and 2^{nd} order reflection photons as compared to the main spectra. Having this, along with the difference in transmission due to the extra filter, should allow for the relative contributions from each spectral order to be determined. In the end, we only want to include the contribution from 1^{st} order photons.

The next element in the light path is the x-ray crystal, which is the spectrometer's dispersive element. According to Bragg's Law of diffraction from a crystal lattice with separation d,

$$n\lambda = 2d\sin\theta, \tag{2.7}$$

photons of a given wavelength λ and integer multiples $n\lambda$ of that wavelength will be diffracted through the angle θ, which will correspond to some position on the detector. Recall that wavelength λ relates to photon energy $h\nu$ or E by $E = h\nu = hc/\lambda$. The integer n is referred to as the order of reflection. At a given position on the detector there will be photons from different orders of reflection all contributing to the brightness of the image. However, the reflectivity of the crystal drops quickly for orders of reflection above $n = 1$ and it also varies according to photo energy. For example, for the KAP crystals used in this experiment the reflectivity of 1000 eV

photons in 1^{st} order is more than 10 times that of the 2000 eV photons in 2^{nd} order that would be refracted through the same angle by the crystal.

Because the crystal is elliptically bent and the location of the Z-pinch is at the far focus of the ellipse, the reflected photons will come to a focus at the nearby focal point of the ellipse. At the crossover slit which is placed at this focal point, a filter of aluminized Lexan (1 μm Lexan with 0.2 μm of Aluminum) is used.

The final element in the light path is the detector that is being used to capture the spectra. Both types of detectors available to this experiment respond to the x-ray signal in a way that is dependent upon both photon energy and intensity. This can be taken into account by using Henke's model [40,41] for the x-ray film response, and by using Rochau's model [43] for the MCP detector response.

Chapter 3

Data Processing

The data obtained from the photoionization experiments performed on the Z Machine are rich in information. But before being able to extract it, the data must be reduced to a form that will allow for the desired information to be extracted. For the type of analysis that will be done with these data, each spectrum needs to be in the form of a transmission spectrum, which tells the fraction of radiation transmitted through the column of Neon plasma along the line of sight of the spectrometer during a given experiment. This chapter will discuss the sequence of steps taken during the data processing phase and the rationale behind these steps.

3.1 The Data

The TREX spectrometer allows us to obtain both time-integrated and time-resolved x-ray spectra in the 850 - 1250 eV photon energy range. An example of each of these is shown in Figure 3.1.

The time-integrated data shown in Figure 3.1(a) can have up to six nominally identical slit spectra. The photon energy axis is increasing from left to right. The slit images are referred to by number from "Slit 1" through "Slit 6" from top to

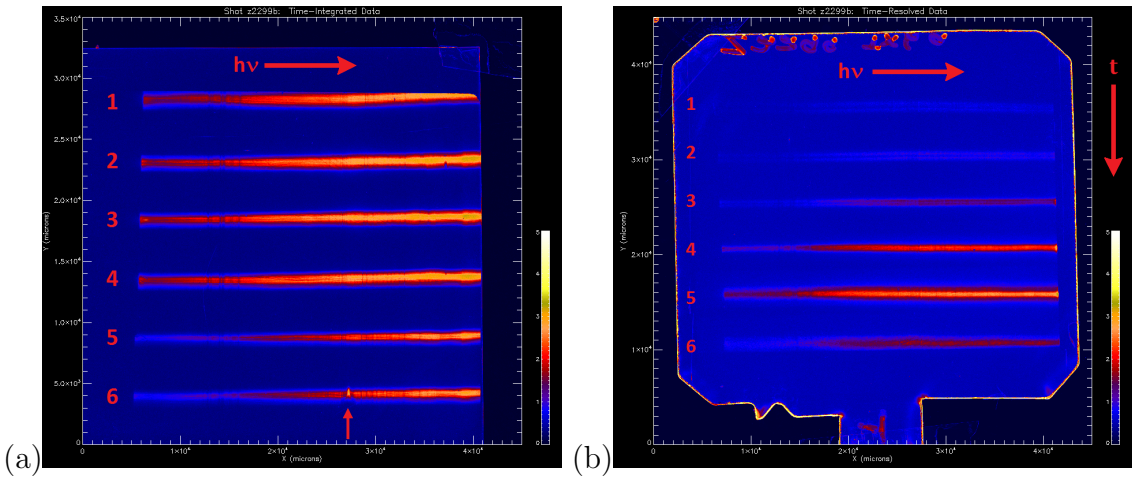

Figure 3.1: Two types of spectral data recorded with TREX, both from shot z2299: (a) time-integrated and (b) time-resolved. In (a), notice there are two slit spectra that are dimmer than the other four. These slits contain an extra Kimfol filter. The arrow indicates an artifact that results from imperfections in the x-ray crystal. There are other artifacts also visible, including the top slit being slightly cutoff. In (b), the time axis increases downward. In both examples, the photon energy increases toward the right.

bottom. As was mentioned in Section 2.6, two of the slits, Slits 5 and 6, contain an extra Kimfol filter, which allows for the determination of how much of the incident radiation came from 2nd order reflection photons from the KAP crystal. As can be seen in Slit 6, there are often defects or artifacts in the spectra which may affect the processing and analysis. In addition, as can be seen in Slit 1, sometimes the slit images get cut off by something interfering inside the spectrometer. Since these are time-integrated measurements, each slit spectrum contains information over the entire course of the experiment. The line of sight is approximately the same for all of the slits, so the slit spectra of each kind (i.e. with Kimfol and without) contains approximately the same information and are nominally identical. It follows that the spectra of each kind can be averaged in order to reduce noise and increase the signal to noise ratio.

The time-resolved data shown in Figure 3.1(b) can also have up to six spectra, but each spectrum is a different snapshot in time. The time axis goes from top to

bottom, and the photon energy axis is again increasing from left to right. However, since these are capturing spectra from different times throughout the experiment, they cannot be averaged to reduce the noise. The focus during the time over which this thesis work has been conducted has been on the time-integrated data, so the time-resolved data will not be referred to very often. Though it's important to note that the time-resolved data contains very important information about the evolution of the plasma in these experiments.

The data is received as digitized images of film optical density, which is basically a measure of how dark the impingent radiation made the film at a given position.

3.2 Procedure Sequence

In order to process these data, we have written a suite of programs in Interactive Data Language (IDL) to handle the different steps throughout the procedure. This programming language makes the use of graphics for images and plots very easy. It also has many built-in functions that are widely useful, and it is ideal for working and interacting with data. In this section, the sequence of steps taken in processing and reducing the data into a form which will allow for the extraction of the information wanted in the end will be discussed. Here, the focus will be on the procedure used for the time-integrated data, which differs from that of the time-resolved data.

The data is received in the form of the images shown in Figure 3.1, but for the analysis, it is necessary that the data be in the form of a transmission spectrum. The reasons for this will be discussed in Chapter 4. The processing, outlined in Figure 3.2, can be broken down into 3 major steps, each of which will contain several smaller sub-steps. These major steps are:

1. Photon energy calibration

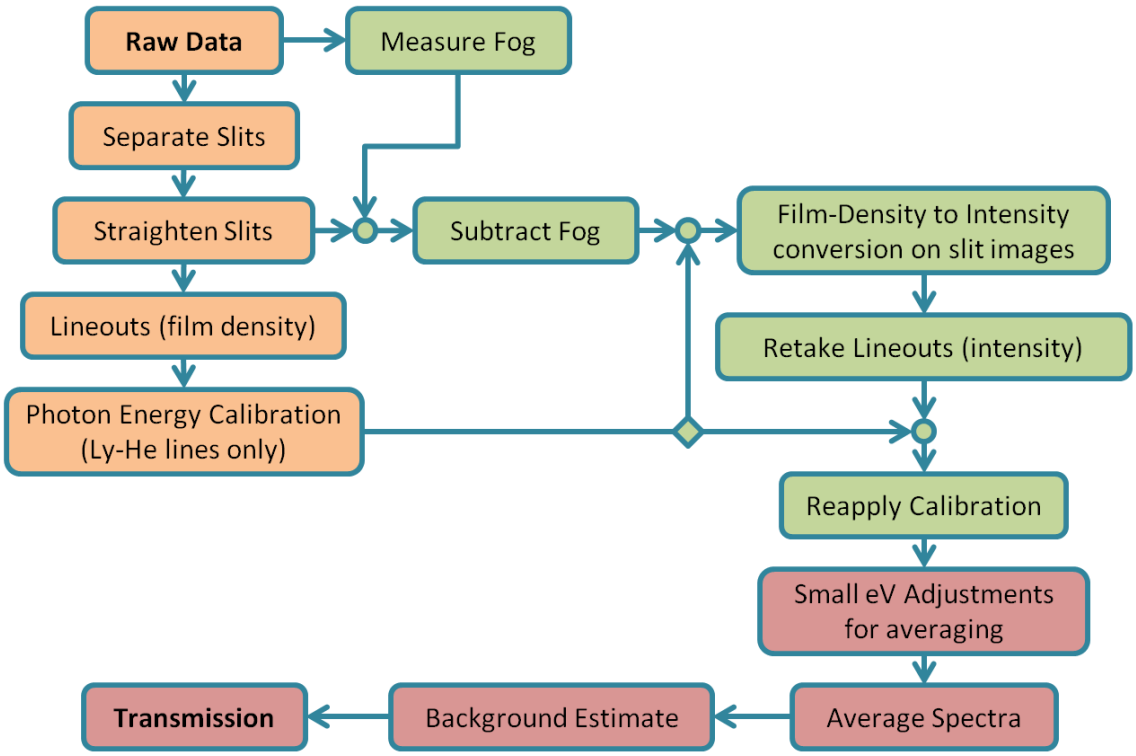

Figure 3.2: Flowchart of steps performed to process the time-integrated data. Each major step is identified by a different color. Orange relates to the photon energy calibration. Green relates to the film-density to intensity conversion. Red includes the final steps to obtain the experimental transmission. The arrows indicate the direction of flow, and the circles indicate where multiple pieces of information come together to be used in the following step.

2. Film density to intensity conversion

3. Zero level of absorption estimate.

3.2.1 Photon Energy Calibration

The first major step (Figure 3.2 in orange) is to establish the photon energy axis calibration for each slit spectrum. For this, a lineout or horizontal profile is needed from each spectrum, but the slit images are generally bent to some extent, as illustrated in Figure 3.3(a). This is caused by non-uniformities in the elliptically bent crystals. To extract the lineout, the image must be straightened first or the lineout must be

(a) 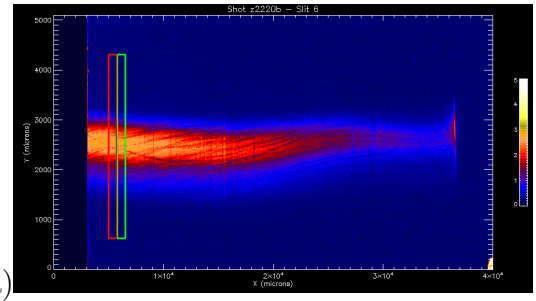 (b) 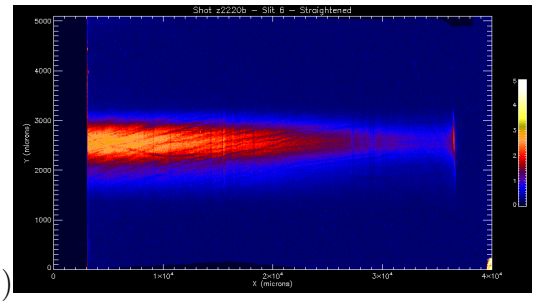

Figure 3.3: An example of a slit image (a) before and (b) after straightening. Also shown in (a) are the areas used for two adjacent lineouts used for straightening. The one in red represents the "reference" lineout, and green represents the "comparison" lineout.

taken in a way that follows the curvature of the slit image. There are different ways to accomplish each of these approaches, and a few have been tested.

The method that has become standard is straightening by minimum difference. The method begins with the separation of each slit image into its own individual image so they can be worked with separately. In order to find the variance in the vertical position of the slit image in one of these images, a series of adjacent vertical lineouts are taken across the entire length of the slit image. Starting from the bright end of the slit image (left) and working toward the dimmer end (right), each adjacent pair of lineouts are compared to find what vertical shift would be required to align the second of these with the first. Figure 3.3 (a) shows the areas from which two such lineouts were taken. The particular pair shown would be after several had already been compared. The lineout outlined in red is referred to as the "reference" lineout, and the one outlined in green is referred to as the "comparison" lineout. The best comparison between these two lineouts is done by finding the minimum of the sum of the square of the differences as a function of the shift.

$$Q^2(s) = \sum_i \Big(D_{ref}(y_i) - D_{comp}(y_i + s) \Big)^2 \tag{3.1}$$

$D_{ref}(y)$ refers to the values (i.e. average film density) in the reference lineout as a function of vertical position y in pixels on the image plane, and $D_{comp}(y)$ is for the comparison lineout as a function of the same vertical positions. To obtain the set of values for $Q^2(s)$, s is varied in integral steps (i.e. pixels) in Equation 3.1. The result of this is shown as the red dots in Figure 3.4. The minimum of this set is found, then the 7-point neighborhood about this minimum is fitted with a parabola, which is shown in green. The shift s for which the parabolic fit is at its minimum, indicated by the vertical blue line in the figure, is used as the shift that best centers the comparison lineout onto the reference lineout.

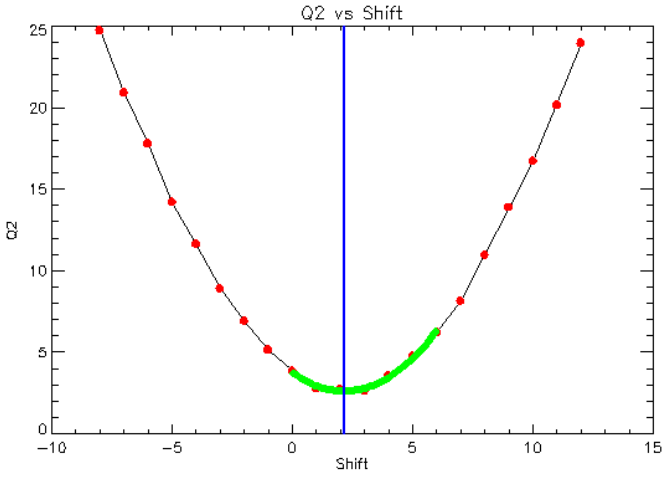

Figure 3.4: Q^2 versus vertical shifts. The red dots show the results of varying s in Equation 3.1. The green line shows the parabolic fit to the 7 point neighborhood about the minimum point. The blue vertical line shows the s value at the vertex of the parabolic fit.

This sequence is continued, using adjacent lineouts, until the user selects some lineout to be the reference for the whole set. This lineout becomes the lineout of zero shift, and all the shifts associated with the previously examined lineouts are adjusted to be measured relative to this one. All further lineouts to the right are just compared directly to the reference lineout. The result of this process can be seen in Figure 3.5 giving a set of vertical shifts as a function of the horizontal axis of the slit image

plane.

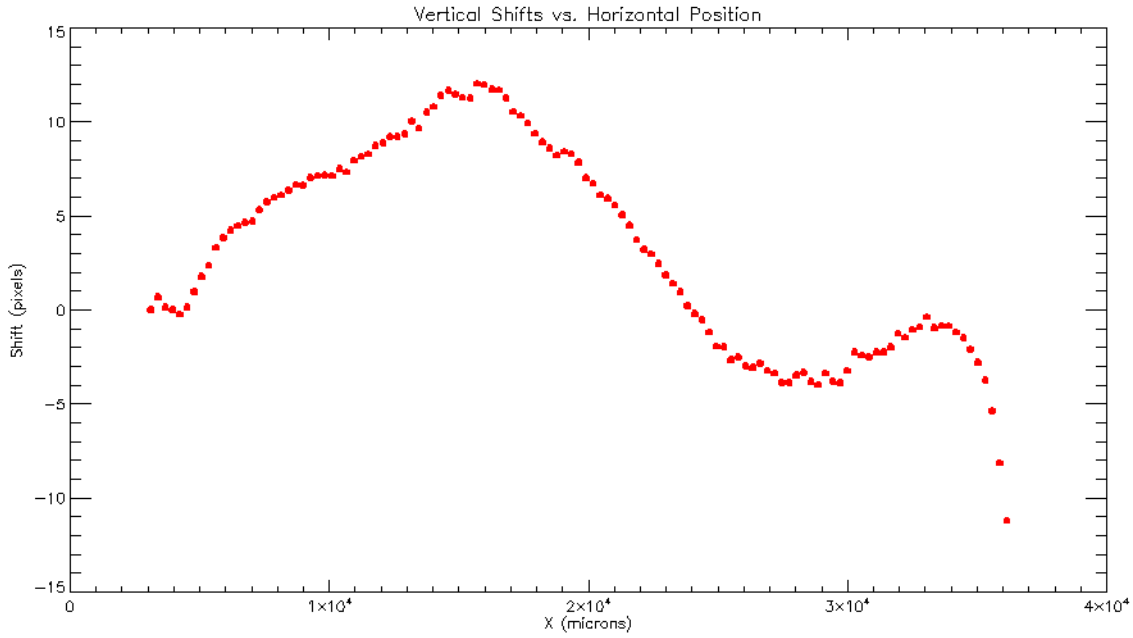

Figure 3.5: Shifts found for each vertical lineout across the slit image plane.

The reason this approach is taken is because sometimes the dim end will be very near the background level, and comparing two lineouts that have a higher fraction of noise (i.e. lower signal to noise ratio) will likely produce more errors than if one lineout is "nice" (i.e. high signal to noise ratio) and the other is more noisy. This is why a reference lineout is chosen near the brighter end of the spectrum. There are occasional errors that may occur at some points when trying to find the shifts, especially in dim areas, but these points are removed. The remainder of the shifts are fitted by a spline to obtain a set of shifts covering each pixel along the horizontal axis of the slit image. These values are then rounded to the nearest integer and the final shifts are applied to the slit image by shifting each pixel column up or down accordingly. The result can be seen in Figure 3.3(b). From this, the spectral profile can be easily extracted.

As was mentioned above, there are a few different ways of handling the fact that

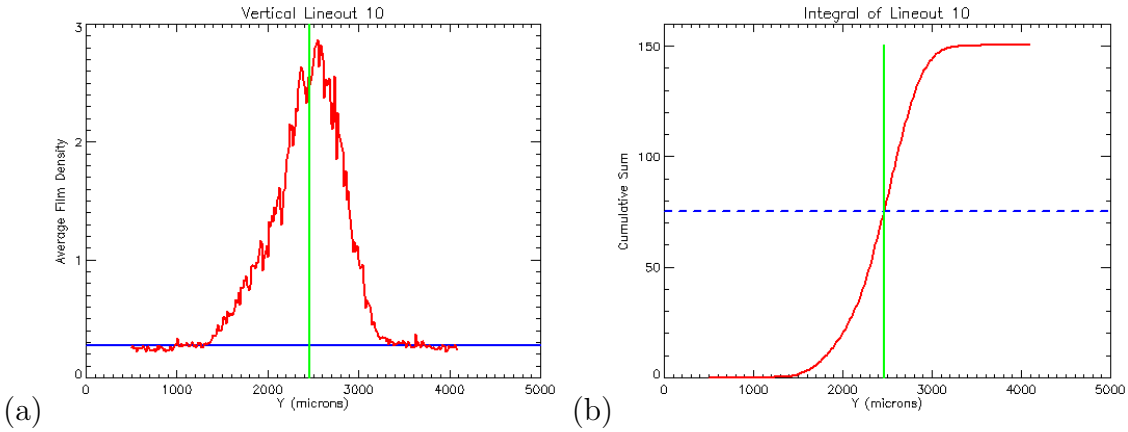

(a) (b)

Figure 3.6: (a) Vertical lineout from a slit image (red) with a baseline (blue) to be subtracted out and the centroid position (green). (b) Cumulative sum (red) of the lineout in (a), half of the total integral value of the lineout (dashed blue), and the centroid position (green).

the slit images are bent. Two other methods of approaching this problem should be briefly discussed as well. The first of these is another straightening method, straightening by centroids. This method was created before the straightening by minimum difference method explained above. For the most part, the procedure is the same. Where it differs is in the way that the shifts are retrieved from the set of vertical lineouts that were taken across the length of the slit image. This method computes a centroid for each vertical lineout. The centroid calculation is summarized in Figure 3.6. Each centroid is calculated by integrating the baseline subtracted lineout from one end to the other, while keeping track of the cumulative sum as a function of position. This is essentially the cumulative distribution of the lineout, and it is monotonically increasing because any values that go below zero when the baseline is subtracted out—typically only at each edge—are just set to zero. The centroid is determined as the position where this distribution reaches half of the maximum value (i.e. the total integral of the vertical lineout). The set of centroids from all of the vertical lineouts is fitted by a spline to obtain the centroids associated with each pixel column. Finally, the average of the set of centroids is computed, and each pixel

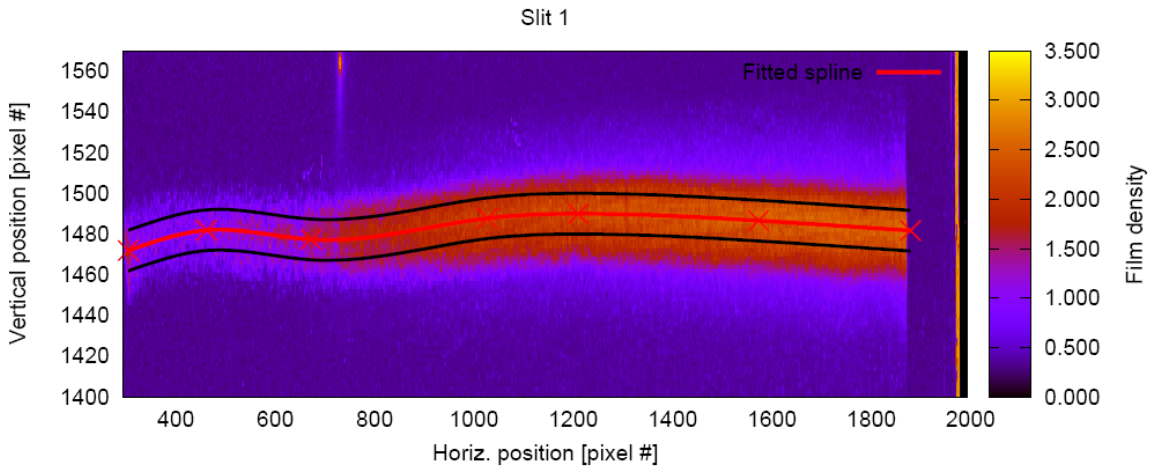

Figure 3.7: A curved lineout taken from slit 1 of shot z2030 [45].

column in the image is shifted so that the centroids are moved to the location of the average to straighten the image.

The other method involves finding the curvature of the slit image and taking the lineout using that information [45]. For a given slit image, a small set of points are defined along the center of the slit following the curvature of the slit. This set is used as an initial guess for a genetic algorithm search. The points are fitted by a spline and a width tells what vertical area around the curve is to be included in the lineout. The mission of the genetic algorithm is to vary the individual positions of the initial points in the vertical direction in order to maximize the intensity of the resulting lineout. Figure 3.7 shows an image that illustrates the curved lineout method [45].

All three of these methods produce very similar results. The main reason for choosing the straightening by minimum difference method for standard use is that it was the easiest to automate the longest part of the process in IDL, which made it significantly faster than the centroid straightening method. This is important when dealing with a large volume of data.

Once the slit images are straightened, it's straight forward to take the lineouts for each slit spectrum. What must be determined in order to do it is the vertical position

of the lineout and the vertical width over which to average. These are estimated automatically by the program created for taking lineouts. First, an initial estimate for the vertical center of the lineout is determined. This is done by taking, arbitrarily, 25 evenly spaced vertical lineouts or cross sections across the length of the slit image and finding the centroid of each one. All centroids outside one sigma standard deviation are disregarded and the remainders are averaged. The pixel closest to this average is the initial estimate for the lineout center in the vertical direction. For the width, the full width half max (FWHM) of the slit image cross section is a good place to start, so first the actual horizontal extent of the slit spectrum is found by looking at the horizontal profile along the estimated central pixel row. The slit cross section comes from the inner 90% of what is found to be the extent of the slit spectrum. The baseline of the cross section is found by putting the different cross section intensities into bins like a histogram and then averaging the bin containing the most values. The half max is half way between the baseline and the cross section peak. The FWHM is found by going down the slopes of the cross section from the peak and finding the distance to the pixels with values just lower than the half max on each side. The sum of these distances is the FWHM, which is made odd by adding one if necessary, so that there is a central pixel, and the lineout center that was estimated above is offset to match the new found center. These parameters are generally well estimated by the program, but the user can change them if necessary before saving the lineouts.

The resulting lineout from each slit is then used to obtain an initial photon energy calibration for each slit spectrum. An example of a photon energy calibrated lineout is shown in Figure 3.8. There are several spectral lines that are almost always visible in the spectra. These include line transitions in the H-like Neon Lyman series and the He-like Neon series. The primary lines used here are Ly-α (1s - 2p), He-α ($1s^2$ - 1s2p), He-β ($1s^2$ - 1s3p), and so on through the He-like series up to a maximum of

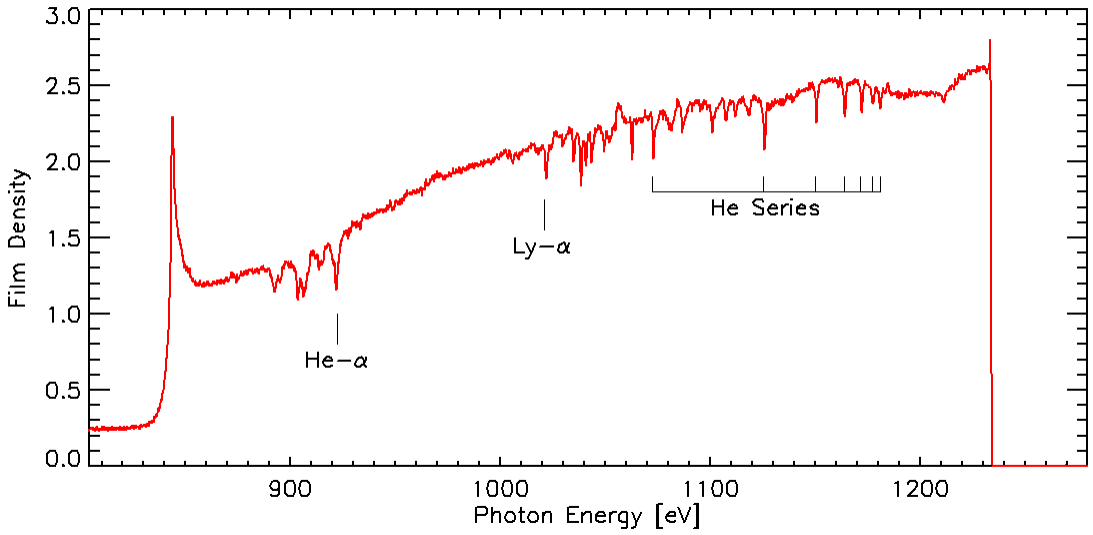

Figure 3.8: Photon energy calibrated spectral lineout in film density units.

$n = 10$. Refer to Section 4.1 for a more detailed description of the spectral range and what absorption features are available. The first several transitions from the He-like Neon series are pretty much always visible, and Ly-α is usually visible.

The calibration begins by using a position versus wavelength theory curve that was generated by a program developed at SNL called EXRAY [46]. EXRAY uses the theoretical design of the instrument with nominal distances in the experiment to calculate a theoretical dispersion curve as it would be expected to be recorded on the film. This curve gives a good initial estimate of position versus wavelength of x-ray photons incident on the film, but since the calculation is dependent on many different lengths and positions that may or may not stay perfectly consistent from shot to shot, it is not perfect. The first step is to align this position versus wavelength curve with the data using the position of one spectral line feature. If the Ly-α is available, it will be used it for alignment because it is near the center of the spectral range. Otherwise, He-β could be used, or sometimes He-α. Following this, the theoretical spectral dispersion curve is adjusted to match the line locations in the slit spectrum

data. To do this, there is a program that allows the user to shift the rest of the H-like and He-like transition lines to match a reference spectrum, for which a synthetically generated absorption spectrum containing only H-like and He-like transitions is used. This reference spectrum is created in the same way as explained in Chapter 4 in the spectral analysis but using dummy values for the number densities. For each line feature to be aligned, a position in the slit spectrum is selected, and then a position in the reference is selected. To be clear, these do not have to correspond to actual data points in the each spectrum. The reference position is, by default, set to be the local minimum near the actual position selected, but there is also an option to leave it as the actual position selected. The local minimum is the default because the synthetic spectrum is smooth and this is a simple way to find the peak of the reference line. Later, after all of the position pairs have been selected, the wavelengths of the slit spectrum positions will be shifted to match the reference positions. In the areas between where this direct matching of positions occurs, the shifts come from linear interpolates based on the shifts of the two chosen positions on either side of a given position. On each edge of the spectrum, where there is only one neighboring shift, this shift is just repeated out to the end of the spectrum.

The result of the above is a set of spectra of average film density versus photon energy. The photon energy axis is an initial calibration for the purposes of the next section, and later it may need a little adjusting for the same reason that straightening the slit images was necessary earlier.

3.2.2 Film Density to Intensity Conversion

In this step (Figure 3.2 in green), the film density of the raw data must be related to the actual flux of photons that were impingent upon the film during the experiment. The connection between film density and intensity is non-linear and it is dependent

not only on the film density (or intensity, depending on which direction the conversion is going), but also on the photon energy. This is why the photon energy calibration for each spectrum needed to be obtained first. More importantly, because the relationship is non-linear, average film density does not convert directly to average intensity. Therefore, at this point, one must go back to the slit images and work directly with them.

The data has some non-zero background level for at least two reasons, and this background level must be removed before the film density to intensity conversion is performed. The first reason that this non-zero background level exists is because the developed x-ray film, even with zero incident radiation, is not perfectly transparent, so it does not measure as zero film density. This inherent film density is referred to as "fog", and it relates to how the film is handled in preparation for the experiment and while it is being developed since any stray light during this time may darken the film. The second reason is that there is some finite level of stray x-ray radiation that makes its way through the spectrometer and onto the film during the experiment. The approach taken to remove the non-zero background in the data makes the assumption that both of the above contributions can be lumped into one measurement of the average film density in the background regions of the image (i.e. areas where no spectral signal is apparent). This value can then be subtracted out of the data image before performing the film density to intensity conversion. When subtracting this fog level out, any pixel values that go negative, because they are below the average film density value used, are set to zero. This is only likely to occur in areas of the image with no spectral signal, and it is done because the film density to intensity conversion only makes sense for positive values. This approach to removing the "fog" may be an oversimplification because the second contribution discussed may need to be handled individually and more carefully, but this still needs to be looked into.

The model used for the film density to intensity conversion is described in two papers by Henke et. al. [40, 41]. The mathematical model is described in the first of these, and in the second, the experimental characterization for the model. The units of the resultant intensity are photons per square micron. This model is utilized by assuming that each pixel column in the slit image corresponds to one photon energy from the calibration above. Going pixel by pixel through the image the formula given by Henke et. al. for a thin emulsion, which is applicable for the type of film used in this experiment, is applied. The relevant formula given in Henke et. al. [40] for conversion from film density D to intensity I is

$$\beta I = (1/b)\frac{\exp(\alpha D/a) - 1}{1 - \exp(-\mu' T/\sin\theta)\exp(\alpha D/a)} \tag{3.2}$$

where

$$\beta = [1 - \exp(-\mu_1 d)]\exp(-\mu_0 t/\sin\theta), \tag{3.3}$$

$$\alpha = \mu'/(\sin\theta + \mu' d_0), \tag{3.4}$$

and

$$\mu' = \mu_0 - (1/d)\ln\Big(1 - V\big\{1 - \exp[-(\mu_1 - \mu_0)d]\big\}\Big). \tag{3.5}$$

In the above equations, T is the thickness of the film emulsion, d is the effective AgBr-grain thickness, d_0 is an effective emulsion-surface-layer thickness, V is the AgBr volume fraction, t is the thickness of the gelatin-like overcoat on the film, and θ is the angle of incidence. The photon energy E enters the formula through the linear absorption coefficients for gelatin μ_0, AgBr μ_1, and for the heterogeneous emulsion mixture μ'. a and b are empirically determined parameters. Values for μ_0 and μ_1 as a function of E and values for t, d, d_0, V, T, a, and b are provided in tables in Henke

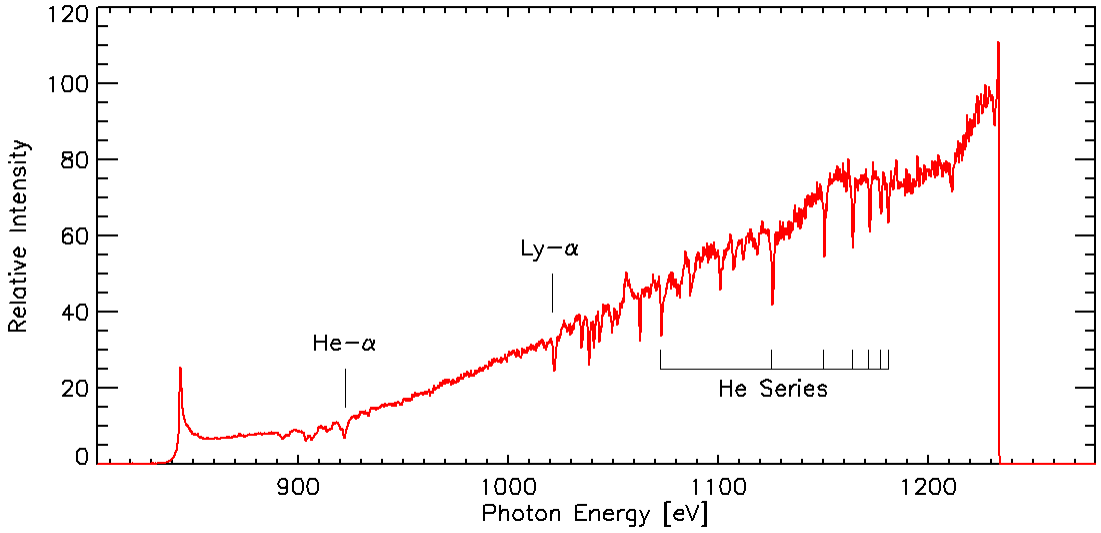

Figure 3.9: Photon energy calibrated spectral lineout after conversion from film density to intensity.

et. al. [41]. The inverse formula for conversion from intensity to film density is

$$\alpha D = a \ln \left[\frac{1 + b\beta I}{1 + b\beta I \exp(-\mu' T / \sin\theta)} \right] \tag{3.6}$$

These formulas are used with the simplifying assumption of normal incidence so that $\sin\theta = 1$.

Once each slit image has been converted to intensity, new lineouts must be taken. It should be noted that because of the non-linear nature of the conversion, the FWHM of the slit cross-section will be reduced. This is due to the fact that higher film densities tend to be amplified more than lower film densities. The new FWHM is used as the width for the new lineouts, which are now averages in intensity. Finally, the photon energy calibration from before is reapplied. The result of this conversion for the spectrum in Figure 3.8 is shown in Figure 3.9.

3.2.3 Zero-Level of Absorption Estimate

In this section, the final stages of the data processing (Figure 3.2 in red) are discussed, in which the slit spectra are averaged and the zero-level of absorption is determined in order to extract a transmission spectrum. This section is a little complicated because there are multiple paths that can be followed in the sequence and there are multiple methods for some of the steps. All of the possibilities and dependencies will be briefly outlined in the next few paragraphs before delving into the details.

This area of the processing can be done in two different sequence arrangements. Namely, the averaging of the slit spectra can be done before finding the zero-level of absorption ("averaging first"), or it can be done after each spectrum has been converted to transmission ("averaging last"). Additionally, the determination of the zero-level of absorption, also referred to as the background, has gone through a few improvements throughout this project. There are two different methods for this, "BKGD" and "BKGD-Null". The first of these attempts to estimate the zero-level of absorption from neighboring continuum regions, and this has gone through two notable versions, "BKGD-v1" and "BKGD-v2". The second method uses null data (i.e. data from an experiment with no Neon gas) to estimate the zero-level of absorption. This section will begin by discussing how and why the averaging is done, along with some considerations that need to be made before averaging. Then it will discuss each method for the zero-level of absorption estimate including considerations regarding the sequence of steps.

First of all, the reason for averaging the slit spectra in the time-integrated data is as follows. Since the noise in a spectrum is randomly distributed, averaging multiple nominally identical spectra together will tend to reduce the noise level because noise above and below the mean value (i.e. the signal) will tend to cancel out with more samples. This increases the signal to noise ratio and allows the spectral line features

to become more pronounced and clear.

Depending on which sequence arrangement is used, the spectra will be averaged either as spectra of intensity (when averaging first) or as transmission spectra (when averaging last). In each case, the averaging is performed in the same way. But before the slit spectra can be averaged, there are three considerations that need to be made. These may or may not be affected by the sequence arrangement. First, all of the spectral line features must be aligned properly in order to avoid any artificial broadening of the lines that would result from misalignment. When averaging last, this can be done using centroids because the shape and depth of absorption features has been constrained relative to the transmission value of 1, meaning that the centroids can be calculated more definitively. When averaging first, it is done differently at this time because the zero-level of absorption has not been found yet. Second, some spectra may have artifacts that one might want to remove before averaging. The averaging is done differently when this occurs. Third, in the case of averaging first, the spectra may need to be normalized in order to give each spectrum equal weight in the average. This does not apply when averaging last. These three considerations are discussed next, followed by the two methods for averaging.

The spectral line feature alignment is important to do before averaging the spectra to avoid artificial broadening due to misalignment. These adjustments are particularly relevant for the Li- and Be- series since these were not taken into account in the initial photon energy calibration, but the other series may need small adjustments as well. For much of the time during this project, the averaging first sequence has been used because the BKGD method was developed first and reducing the noise through averaging made the BKGD method easier to apply. Also, it meant that only one zero-level of absorption estimate was necessary in total rather than one for each slit spectrum, which saved time. So the centroids method for spectral feature alignment

was not developed nor used until more recently. The method used when averaging first is similar to the latter part of the photon energy calibration from Section 3.2.1. This process starts by visually comparing all of the slit spectra that are to be averaged and finding which lines have misalignments with respect to the set as a whole. The aim is for all of the spectra to be consistent with each other, not necessarily with theoretical values. Any variations with regard to theoretical positions can be dealt with later during the analysis as discussed in Section 4.4. Part of that same program from Section 3.2.1 is used to make the adjustments. For each line that needs to be adjusted, the spectrum wherein the line is nearest to the rough average position with respect to the set is found, and this spectrum is used as the reference while making the adjustment. The adjustment is just done "by eye" for the time being by selecting a point in the spectrum to be adjusted and then a position in the reference spectrum for that point to be moved to. This can be quite time consuming sometimes, but some adjustments can be grouped to save time. It can also be kind of subjective when one is working with spectra where the lines are not very strong and artifacts might be mistaken for a line. In the end, an attempt is made to minimize and limit adjustments made in this manner, and adjustments are only made if it is clearly necessary.

The centroids method for spectral line feature alignment was developed more recently because for the BKGD-Null method it seems to be better to do the zero-level of absorption estimate for each slit spectrum individually and then do the averaging last. The reason for this will be explained when the BKGD-Null method is discussed. The centroids method was developed to be used with transmission spectra because it is easy to relate the absorption line depths to the maximum transmission value of 1. A similar approach can also be developed for use with non-transmission spectra, but this is still future work. The program made for this method works with all of the spectra simultaneously. One at a time, the user defines regions in the spectral range where

adjustments are to be made. For each region, two anchor points indicate the limits of the region. Outside of these points, no shift will be done, and between these points shifts will be made. Next, the number of lines to adjust within the region is supplied by the user. This is followed by the specification of positions identifying the limits of where each line feature is in each spectrum. These limits are used for calculating the centroids for each of the lines in the region. The centroids are calculated using the following formula:

$$x_{cent} = \frac{\sum_i \left[(1 - y_i)x_i\right]}{\sum_i (1 - y_i)}, \tag{3.7}$$

where the index i includes the data points within the limits of the given line feature in one of the spectra, y_i are the transmission values, and x_i are the photon energy values. The average of the centroids for a given line is also found, and this is where that line in each spectrum is shifted to. Similar to the photon energy calibration, points between lines and/or anchors are shifted according to linear interpolates. The result must be checked by the user and can be redone if necessary before continuing on to the next region. This sequence is repeated until all necessary adjustments have been made.

The second of the three considerations to be made before averaging spectra is whether there are artifacts that should be removed from the slit spectra. If there are artifacts in the spectra that interfere with line features used in the analysis, then those artifacts should be removed prior to averaging the spectra. The points can simply be removed from the spectrum files, leaving gaps in the spectra where the artifacts used to be. The result is that in areas where, say, points were removed from one spectrum, there will be one less spectrum contributing to the average in that area. Because the original method used for averaging uses interpolation, a different method is required to handle these gaps in the spectra. This will be discussed as the second method for averaging. The most sensitive part of this removal process is where the endpoints of

removed regions are located. The user wants to avoid creating edges or jumps in the averaged result at places where removed regions begin or end. This is easier to deal with when the spectra are in transmission, but it can also be done carefully when the spectra are not transmission. One must note in the latter case, that normalization of the spectra, which is discussed in the next paragraph, may affect the choice of endpoints for removed regions, therefore extra care is necessary if normalization is to be done also.

The third of the three considerations needed before averaging spectra is with regard to normalization of spectra so that they have approximately equal weight in the averaged spectrum. This is only relevant when averaging first. Often times, the level of the spectra are close enough that the difference whether this is done or not is small. But there are cases where one or more of the spectra are brighter or dimmer than the rest. In these cases, if the outlying spectra are to be included, normalization is important to do. The program used for normalization is such that it can be done while in the process of averaging or it can be done separately. The way this normalization is done is as follows. Two boundaries of integration are determined by the user. Within these boundaries, each of the spectra are integrated to produce a scalar value representing the area under each spectral curve. The average of these values is found and each spectrum is scaled such that the integral under the scaled version matches the average.

Once these three considerations have been made, the spectra are ready to be averaged. In earlier experiments, the x-ray crystals were newer and they produced few artifacts that would be considered necessary to remove, and so at that time, it was not a consideration that was made. It was later that cases began requiring removal of artifacts. Thus, in the first averaging technique that was used, all of the spectra were continuous, and there were no gaps or holes in them. Still, the

averaging cannot simply be done pixel by pixel because the photon energies of the pixels in one spectrum do not map to the same photon energies in the other spectra. For this reason, the approach used to perform the averaging is as follows. The range of overlap between the spectra and the minimum separation of points in eV is found. The range is divided by the minimum separation and the nearest whole number is used to create a new, uniform grid for the photon energy axis. Each spectrum is linearly interpolated onto this grid, and the results are then averaged pixel by pixel to produce the final averaged spectrum.

The second method of averaging became necessary once artifacts were removed from the spectra, creating gaps and holes. If the first method were to be used with these gaps, the linear interpolation would create a flat, linear area in the regions where points were removed, rather than simply ignoring those areas, as is desired. For this reason, a more discrete approach is taken. To start, the full range of all the spectra is determined, and this range is cut into equally sized "bins". The points from each spectrum are placed into the bins according to where they are in photon energy. If two or more points from one spectrum fall into a single bin, then these points are averaged before being put into the bin. In this way, each spectrum can contribute only one or zero values to a given bin. The values in each bin are averaged to produce the final spectrum. If, in the end, a bin contains zero values, then it is ignored and will not be included in the final spectrum. The values of the photon energy axis of the final spectrum come from the center value of each bin. What to choose for the bin size is not easily apparent, and what has been chosen for now may not be the best choice, but here is how it is found. The bin size is determined from the inter-point spacing. The spacing in a typical spectrum from these experiments varies from about 0.10 eV at the low-energy end to about 0.25 eV at the high-energy end of the spectrum. The median spacing is found for each spectrum. The minimum

of these is multiplied by two, and this is used as the bin size. This has typically resulted in bins of around 0.3 eV in size, and the average spectra that result have thus far seemed quite reasonable. The original reason behind using a larger bin size was that if, for example, the minimum spacing were used, then toward the higher-energy end of the spectrum, it is likely that less averaging would occur because less points would fall into each bin. Even if one of the median values were used, this would still happen. However, another, possibly more logical bin size to use might be the maximum spacing. On the other hand, at the low-energy end of the spectrum, the effect will be that multiple points from each spectrum will end up averaged in each bin, which could affect the spectral resolution. This makes smaller bin sizes desirable. However, since the instrumental resolution is about 1 eV, this is not likely to be a problem, but it reinforces the idea of using the maximum spacing as the bin size instead of what is currently done.

Lastly, there are the zero-level of absorption or background estimate methods to discuss. The final product of all of this processing is a transmission spectrum. A transmission spectrum tells the fraction of radiation at a given photon energy that was, in the case of this experiment, transmitted through the column of Neon plasma along the LOS of the spectrometer during the experiment. A transmission can be obtained by taking the ratio of an absorption spectrum to the background level at which there is zero absorption. During a given experiment, there is no direct, simultaneous measurement of the background level without the Neon plasma present which also takes into account everything else along the LOS, including the peculiarities of each x-ray crystal. Therefore, the background level must be estimated in some other way.

There are two different methods that will be discussed that have been developed and employed during the course of this project. The first method, “BKGD”, attempts

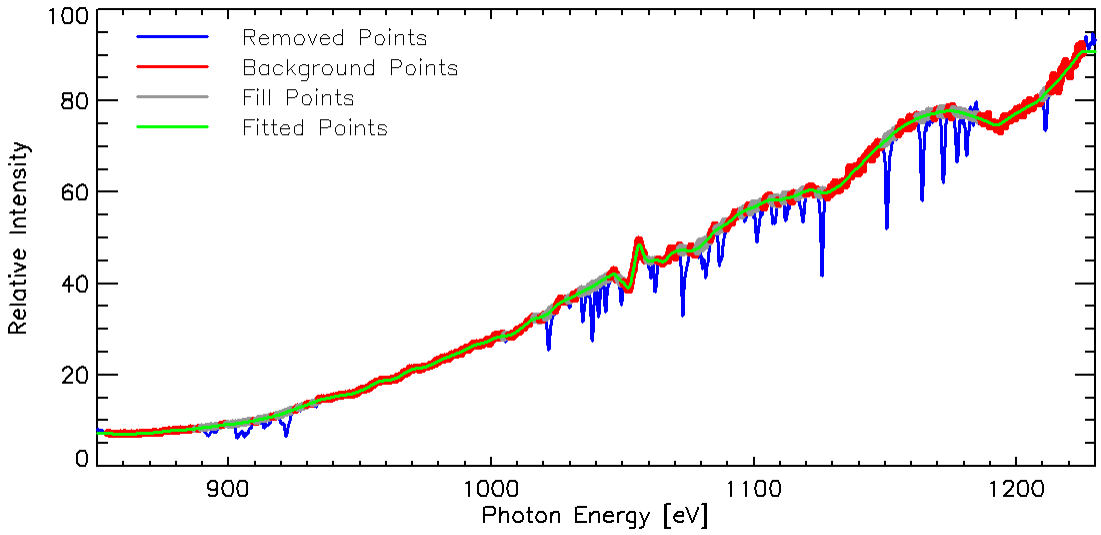

Figure 3.10: Plot illustrating the BKGD method of zero-level of absorption estimation. The original spectrum is plotted in blue showing areas that were removed, including known line features and features not considered to be part of the "background". Shown in red are parts from the original spectrum considered to be part of the background. In gray are areas where removed points were replaced by fill points obtained from fitting the nearby background and adding noise (BKGD-v2). Finally, in green is the result of smoothing the background with the Butterworth filter. The green line is then divided into the original spectrum to obtain the transmission spectrum.

to estimate the background level from the neighboring continuum by removing known line features and replacing them with something smooth, which is determined from the neighboring continuum regions. There have been two different programs developed using this method with differing sophistication, "BKGD-v1" and "BKGD-v2". The second of these was created as an improvement upon the first, but it does not invalidate results from the first. There are analysis results from transmissions created from both programs, and there are significant differences between the programs, so both will be discussed here. Figure 3.10 illustrates the BKGD method in general, using results from BKGD-v2.

In BKGD-v1, line features are first removed from the spectrum. In the areas where points were removed, they are replaced by points along a line connecting the

two adjacent remaining points. After this, a low-pass Butterworth filter [47] is applied to obtain a smooth curve that gives the basic curvature of the background level. The reason for choosing to use a Butterworth filter rather than some other type of smoothing filter is that since it works in frequency space, features in the spectrum below a certain length can be completely removed leaving features longer than that unaffected. Secondly, the Butterworth filter has a sloped cutoff edge, which mitigates the ringing effect that occurs with an ideal filter. The equation used for filtering in frequency space is

$$F(\omega;\lambda,n) = \frac{1}{1+(\omega\lambda)^{2n}} \tag{3.8}$$

where ω is the frequency, λ is the cutoff length in pixels, and n is called the order, which determines the slope of the cutoff. The parameters of the Butterworth filter, λ and n, can be adjusted to produce a smooth curve. These parameters are set by the user and vary according to the data, but generally $n = 2$ is used. The curve resulting from this filtering can then be divided out of the spectrum to give the transmission spectrum. There are several issues in this version that warranted the development of the second version. First, the subprogram used to remove points was not good, one reason being that points could not be unremoved. Second, simply filling removed areas by linear interpolation between remaining points is not very good because it places too much importance on the particular points that are left at the edge of the removed section. The noise exacerbates this problem. Third, some of the areas where lines are removed have clearly curved backgrounds in which case curves would be better to use than lines.

BKGD-v2 is based on the ideas from the first version, but it includes the improvements mentioned above plus some others. In this version, each area where there are points to be removed will be associated with a "region". Within each region, points can be removed and unremoved. The remaining background points within each region

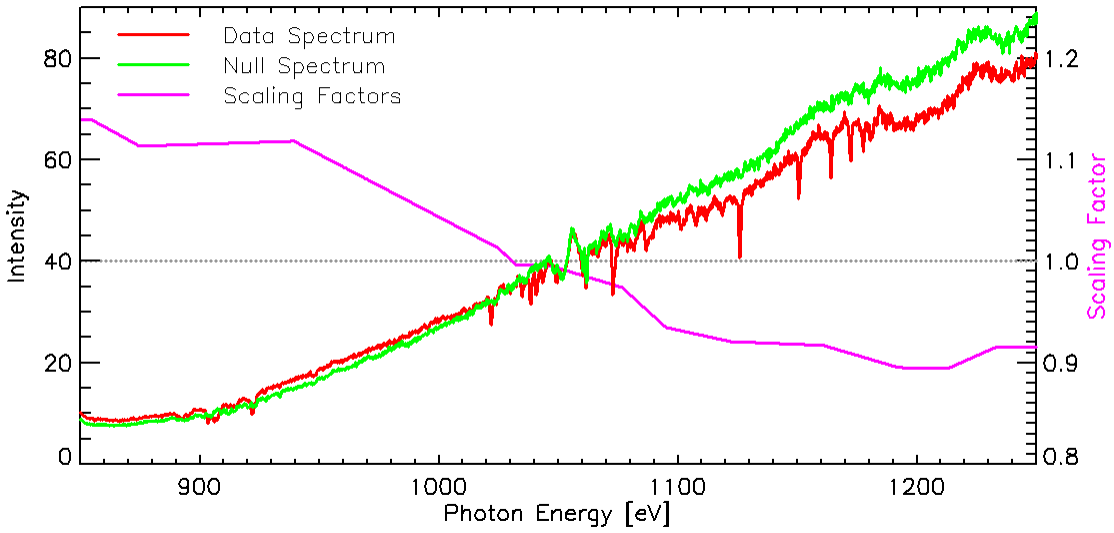

Figure 3.11: Illustration of the BKGD-Null method of zero-level of absorption. The data spectrum is plotted in red, while the null spectrum before smoothing with the Butterworth filter is plotted in green. The scaling factors necessary to scale the smoothed null spectrum to match the level of the data spectrum are shown in pink.

are fitted with a polynomial of degree specified by the user, around which randomly generated "noise" is created to fill in the removed points. This noise is based on the standard deviation of the remaining background points from the polynomial fit in the region, and it is smoothed slightly to more closely emulate the noise of the data itself. After the line features have been removed, BKGD-v2 also uses the Butterworth filter to find a smooth curve to represent the zero level of absorption, but it has a slight improvement in that you can have regions that use different parameters for the Butterworth filter for that region. This can be useful when there are areas where the background is sharper than in other areas.

The second method for the background estimate, "BKGD-Null", is based on using null data from different shots from the Z-Machine to estimate the background level for a given set of data. An illustration is shown in Figure 3.11. The term "null data" refers to data from a shot in which there was no Neon gas in the gas cell at the time of the shot. Everything else in this type of shot (e.g. along the LOS, etc.) is just as if a

regular shot was taking place. This is the preferred method primarily because of the existence of crystal artifacts. As more experiments have been done, the crystals have aged and have developed some defects that are visible in the data. There has also been some difficulty in replacing the crystals. Some of these defects overlap important line features in the spectra. It is much more difficult to account for this when using the BKGD method. However, the use of null data is not guaranteed to work well. Recall that each slit spectrum is associated with light passing through a particular slit in the spectrometer. That slit image is reflected from a particular area of the crystal, which may vary slightly from shot to shot. Ideally the position would be identical on each shot, but a difference occurs due to mechanical uncertainties from having to replace the Mylar on the slits and from sliding the crystals out of the way and back in order to aim the spectrometer between each shot. This slight difference in where the slit image falls on the crystal can have an important effect on the detailed shape of the background continuum in a given shot. One null shot is obtained during each shot series, but depending on the difference in position of the slit images with respect to crystal artifacts between the shots, the null data may be of limited use for a given shot. There are some possible solutions to this issue that will be discussed in Chapter 6. In the case where there is no suitable null data for the background estimate of a given shot, the BKGD method is the most reasonable option.

For the BKGD-Null method, the first step is to find null data that is likely to work well with the experimental shot in question. If available, a null shot from the same shot series is likely to be best, and obviously, the data must be from the same x-ray crystal. Other variables that should be considered in the null data are the window thicknesses and cell distance, especially if it is necessary that the null data provide correct levels where Silicon lines from the windows interfere with the Be-like Neon series. The radiation flux, in terms of general spectral shape, is generally fairly stable,

but occasionally the shape will inadvertently vary, so this needs to also be considered. The most important thing that must be considered, as mentioned above, is that the slit image positions with respect to crystal artifacts is close.

The BKGD-Null method basically requires processing another entire shot while taking into account specifics relating to the shot with which the background is to be used. A single program that guides the user through the processing of the null data while relating it to the experimental data has been developed to ease the process. It was developed to be used when averaging first, and this is how it will be explained, but it can easily be used when averaging last by including only one slit spectrum.

The process begins after the initial lineouts have been taken for the null data. The items needed for this method are the null data slit lineouts, each fully calibrated experimental slit spectrum, the straightened null slit images, and the final averaged experimental spectrum (this would be the same as the fully calibrated experimental slit spectrum when only including one spectrum). The first step is to roughly establish the photon energy axis for each null slit lineout. This is done by presuming, to start, that the photon energy axis from the corresponding experimental slit spectrum can be used and simply shifted to match some distinct feature that appears in both spectra. This makes having at least some artifacts in the data a bit useful, since there are no line features in the null data to use for the initial alignment. Note that when doing this, the null slit lineouts are being compared to the intensity calibrated experimental spectra, so there are significant differences between them, but it is still possible to tell which features can be aligned or not. After this, the rough photon energy calibration for each null slit spectrum is complete. The film density to intensity conversion procedure is identical to that of the experimental data, except that the fog level is obtained from the edge of the null slit lineouts, outside the range of the spectral data. After this is complete, the set of spectra are on a more even footing for comparison, so

the photon energy axis is checked to see whether there are any obvious adjustments that need to be made to make the null spectra better align with the experimental spectra. All of the above is done separately for each null slit in a loop. After all the slits are done, they are averaged together just as is done for the experimental spectra when averaging first. If only one slit spectrum is provided, in the case when the user is planning on averaging last, this step is skipped. Next, the Butterworth filter is used to obtain a smooth curve representing the null background.

The final step that must be done is to scale this null background curve to match the level of the final averaged experimental spectrum. One might expect that a single constant could be used across the entire spectrum, but this is rarely the case anymore. Generally the required scaling factors vary across the spectrum. Possible reasons for this could include variances in the Z-pinch power or spectral shape, effects from the aging crystals, or variance in the position of slit images on the crystals. An attempt is made to minimize the slope of variance in the scale factors. Currently, the way the scaling factors are found is by selecting a number of points in the spectrum in continuum areas. A region around each point of user specified width will be used to calculate the scaling factor required to minimize the difference between the null background curve and the experimental spectrum by least squares minimization. The scaling factor found for each region is associated to the center point of the region. Between each specified point, linear interpolates are used as the scaling factors. At each end of the spectrum, the scaling factor of the nearest specified point is used. This can be seen if Figure 3.11. Generally using several points across the spectrum gets them lined up pretty well. However, this method for finding the scaling factors should be improved upon. Once the null background curve is scaled to the level of the final averaged experimental spectrum, it can be divided into it to obtain the transmission spectrum.

Each of the two zero-level of absorption estimates has a tendency toward one or the other of the two sequence arrangements possible for this section. The BKGD method has a tendency toward averaging first. Whereas the BKGD-Null method has a slight tendency toward averaging last. Additionally, in writing this section, it began to become clear that there may be more benefits to using the averaging last sequence arrangement in general. There are at least two reasons the BKGD method favors averaging first. The major reason relates to noise. The BKGD method requires specifying where line features are, which is made more uncertain and difficult with more noise. Averaging first reduces the noise and simplifies this process. The second reason is that performing the background estimate for each spectrum individually takes longer than doing it only once at the end. However, the centroids method of photon energy adjustment speeds up that process and probably helps its accuracy, and the BKGD-v2 helps to mitigate the need for exact specification of line feature points, so it may be more beneficial to begin using the averaging last sequence with the BKGD method. As for the BKGD-Null method, it favors averaging last mainly because in the sequence of averaging first, the photon energy adjustments are done prior to averaging and prior to processing the null data. This means that those adjustments are included in the rough photon energy calibration for the null data, which are then adjusted again. In an effort to minimize adjustments to the data, adjustments on top of adjustments is not desirable. For that reason, averaging last is better.

Chapter 4

Analysis Method

The objective of the analysis is to characterize the plasma that is created in these experiments. It is important to emphasize that because a goal of this project is to provide data for the benchmarking of atomic kinetics codes, the analysis must be independent of any atomic kinetics calculations. The primary characteristics of interest are the ion charge-state distribution and the electron temperature. This chapter will discuss the approach taken to obtain these quantities.

4.1 Neon Spectrum

The spectral range that the KAP x-ray crystals provide covers approximately 400 eV of photon energy between 850 - 1250 eV. Within this range, there are absorption line transitions arising from the ground and low excited states of four different ions of neon. Namely, there are features from H-, He-, Li-, and Be-like neon ions. Thus far, there have been no instances where transitions from lower ionization stages have been visible in the data, therefore populations associated with ions lower than Be-like neon are considered negligible during the time interval of the measurement. An example spectrum is shown in Figure 4.1 with the nomenclature that will be used for labeling

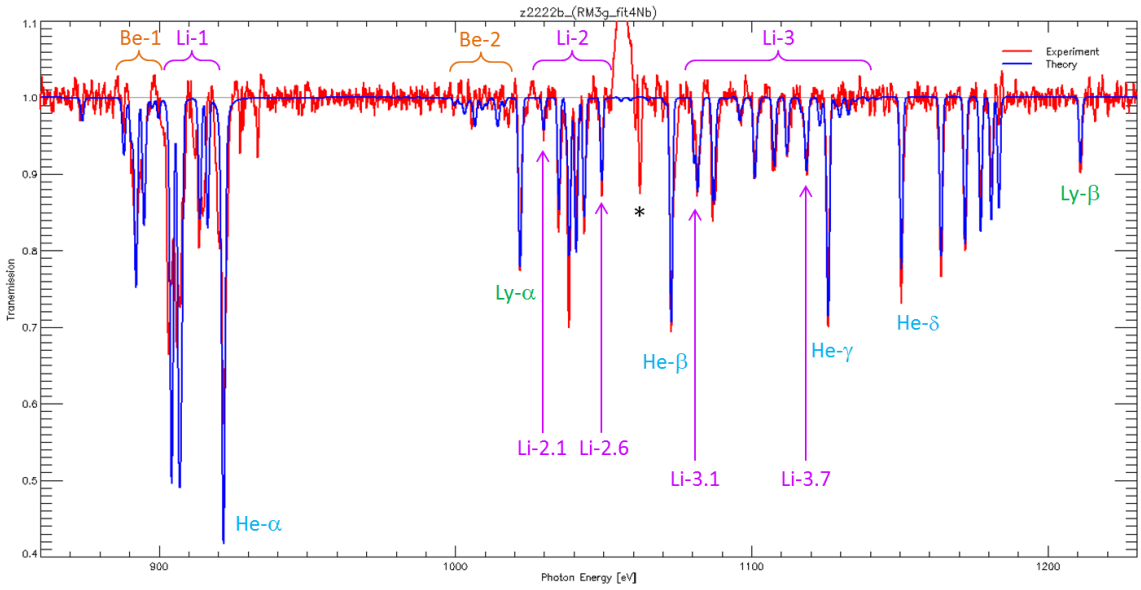

Figure 4.1: Experimental neon transmission spectrum (red) with a synthetic transmission spectrum overlaid (blue). The nomenclature for the visible transition lines is indicated. The feature marked by the asterisk (*) is produced by the alignment cross-hair within the TREX instrument. The feature just to the left of that is a large crystal artifact.

the line features. Figure 4.2 shows a sampling of the atomic structure in the different ion stages visible in the spectra.

Two transitions are visible in H-like neon. These are indicated in green in Figure 4.1 as Ly-α and Ly-β. These transitions arise from the ground state (1s) of H-like neon. The Ly-α line (i.e. the transition from 1s to 2p) is nearly always visible in the spectra, while Ly-β (i.e. the transition from 1s to 3p) is more likely to be visible in shots with higher filling pressures, and it is only clear in some of the shots. These features give information about the highest ionization state achievable in substantial amounts in this experiment because it is not expected that a large amount of neon could become fully ionized for the conditions of these experiments.

Within the spectral range, the entire primary He-like neon series is visible. These transitions, indicated in blue in Figure 4.1, arise from the ground state of He-like neon ($1s^2$) and go to states of the form 1s np. Transitions occasionally up to $n = 10$ in

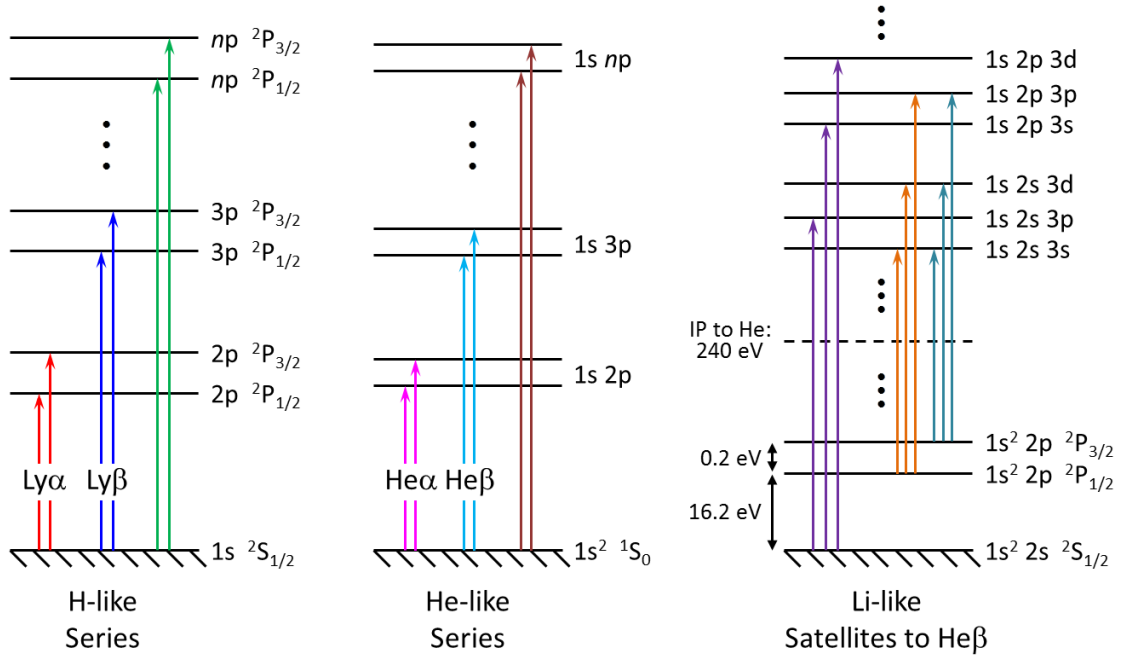

Figure 4.2: A sample of the atomic structure of the H-like, He-like, and Li-like ion stages. Also shown are arrows indicating absorption transitions within each ion stage that can be visible in the spectra. Within the H-like Lyman series, only Ly-α and Ly-β are visible within the spectral range. Transitions with up to $n = 10$ are visible in the He-like series. The transitions shown for the Li-like ion stage are the satellites to the He-β line, which are the Li-2 group in Figure 4.1. These are transitions to autoionizing states lying above the ionization threshold from Li-like neon to He-like neon.

He-like neon can be seen. To refer to these transitions, either the principle quantum numbers in the transition are used (e.g. "He 6 to 1" or "He-6"), or Greek letters are used, as in He-α for the He 2 to 1 transition. For these experiments, most of the neon becomes ionized to the He-like ionization stage. The first few lines in this series are usually saturated, meaning that the absorption of light due to these lines is very strong. Absorption lines begin to become saturated when the optical depth of the plasma for photons near line center starts surpassing a value of 1. What happens in this case is that the sensitivity to the number of absorbing ions along the LOS, which is observable via the absorption line depths, is reduced. This is because adding more particles begins to have a smaller effect on the depth of the transmission line

feature, and when the instrumental broadening and noise are also included it washes out these smaller effects making them difficult to quantify. Essentially there is a loss of information in this case. For this reason, He-α is never used in the analysis, but still, measurements from this series have thus far been problematic. Indeed, part of the subject of this thesis is to address some of the issues regarding measurements from this transition series. This will be discussed further in Section 4.7.

Transitions arising from Li-like neon ions are indicated in purple in Figure 4.1. These transitions originate from one of two states, the ground state, $1s^2$ 2s, or the low excited state, $1s^2$ 2p. The difference in energy between these two configurations is 16.3 eV. The $1s^2$ 2p state is further broken down into two fine structure states, $1s^2$ 2p $^2P_{1/2}$ and $1s^2$ 2p $^2P_{3/2}$, which are separated by about 0.2 eV. There are three separate groups of transitions visible in the spectrum, all of which are satellite transitions to the He-like neon series. Satellite transitions involve transitions between states below the ionization threshold and autoionizing states. These transitions will mirror transitions in a higher ionization stage but will be of a lower energy. The first group of Li-like transitions, referred to as "Li-1", are the satellite transitions to the He-α line. These transitions are from $1s^2$ 2ℓ to 1s 2ℓ $2\ell'$, where ℓ and ℓ' can each be s or p. The second group, "Li-2", are the satellites to the He-β and are from $1s^2$ 2ℓ to 1s 2ℓ $3\ell'$, where ℓ can be s or p, and ℓ' can be s, p, or d. The third group, "Li-3", includes higher members of this series. Namely, these are transitions from $1s^2$ 2ℓ to 1s 2ℓ $n\ell'$, where $n \geq 4$, ℓ can be s or p, and ℓ' can be s, p, or d. The Li-2 and Li-3 groups are further broken down according to the main line features visible in the spectrum. Each of these line features can be composed of many individual but nearly overlapping transitions from each of the three possible lower states. These individual transitions become indistinguishable with the resolution of the TREX spectrometer. The Li-2 group has six main features, labeled from "Li-2.1" to "Li-2.6" in order of

increasing photon energy. The Li-3 group has seven main features between He-β and He-γ which are labeled from "Li-3.1" to "Li-3.7" in the same order. Also associated with this group are some transitions in Li-like neon that overlap the He-γ. When the Li series is strong, this may have a noticeable impact on the He-γ line feature. The most important thing about the Li-like series is that, using the measurements of the populations associated with each of the lower configurations in the transitions, the electron temperature can be inferred under certain assumptions. This is discussed in Section 4.5.

Finally, there are two groups of Be-like satellite transitions that can appear in the spectral range indicated with orange in Figure 4.1. These are labeled similar to the Li groups as "Be-1" and "Be-2". The Be-2 group is very rarely visible in the data and is weak when it is, so it is not used for any analysis. Any information about the Be-like neon population must come from the Be-1 group. The transitions in Be-like neon can arise from three different configurations: the ground state, and the two lowest excited states. These are $1s^2\ 2s^2$, $1s^2\ 2s\ 2p$, and $1s^2\ 2p^2$ respectively. These transitions are similar to the Li series in that they are also satellites to the He-like neon series. The possible transitions are from $1s^2\ 2\ell\ 2\ell'$ to $1s\ 2\ell\ 2\ell'\ n\ell''$, where for the Be-1 group $n = 2$ and ℓ, ℓ', and ℓ'' can each be either s or p in this case. Also, similarly, the measurements of the relative populations of the lower states of the transitions in Be-like neon can be used to infer an electron temperature, though it is slightly more complicated than with the Li measurements. This is discussed in Section 4.5.2. One problem regarding the Be-1 group is that it is contaminated by transitions in Silicon ions due to the Si_3N_4 windows used to contain the gas. The best way, at this point, to account for this is by using the BKGD-Null method of background estimation.

4.2 Analysis Approach

As was mentioned, because one goal of this project as a whole is to provide benchmark data for atomic kinetics codes, it is important that the analysis through which the plasma is characterized be completely independent of atomic kinetics calculations. Information regarding the state of the plasma is written in the spectrum recorded by the TREX spectrometer. The approach taken to avoid dependence on atomic kinetics codes is to calculate a transmission spectrum representing the fraction of the driving radiation that passes through a uniform slab of neon plasma without being absorbed. By varying the parameters of the transmission calculation, the best fit to the experimental spectrum from TREX yields measurements for those parameters.

The simplification to transmission deserves some elaboration. The emergent radiation intensity I_ν at a given photon energy $h\nu$ from a slab of plasma is given by

$$I_\nu = I_{o\nu} e^{-\tau_\nu} + \frac{\epsilon_\nu}{\kappa_\nu}(1 - e^{-\tau_\nu}) \tag{4.1}$$

where $I_{o\nu}$ is the back-lighter (i.e. x-ray drive) intensity at the front side of the slab, τ_ν is the optical depth, ϵ_ν is the emissivity, and κ_ν is the opacity of the plasma. The first term in the sum in Equation 4.1 represents the attenuation of the incident radiation drive as it passes through and interacts with the plasma. The second term represents the amount of radiation due to self-emission of the plasma that emerges from the slab. In the case of these experiments, the intense radiation field from the Z-pinch that back-lights the gas cell is much larger than the amount of self-emission produced by the neon plasma. Thus, the self-emission term is negligible, and Equation 4.1 can be reduced to

$$I_\nu \approx I_{o\nu} e^{-\tau_\nu}. \tag{4.2}$$

With this, the transmission at a given photon energy $h\nu$ is defined as

$$T_\nu \equiv \frac{I_\nu}{I_{o\nu}} = e^{-\tau_\nu}. \tag{4.3}$$

The ability to use transmission simplifies the calculation by not requiring exact knowledge of the shape of the x-ray drive $I_{o\nu}$, but it stills allows for the characterization of the neon plasma. However, it is important to have some knowledge of the x-ray drive for other reasons regarding the interpretation of the analysis results (e.g. where the plasma falls in the photoionization regime), but for the primary measurements it is a significant benefit to not require this information. Another reason that using a transmission helps to simplify the problem is because the filter transmissions will cancel out exactly because they affect both I_ν and $I_{o\nu}$ in exactly the same way as viewed by the spectrometer. Recall that this is the reason they were not considered during the data processing.

The assumption of a uniform slab of neon plasma deserves some elaboration as well. The conditions within the gas cell will vary from the front to the back. The dilution effect on the radiation field as it propagates outward from the Z-pinch, as well as the limiting apertures of the gas cell windows means that the x-ray drive that the neon at the front side of the cell sees will differ from that of the neon at the back side of the cell [33]. Also, there will be shocks through the plasma as the windows expand, causing further non-uniformities in the plasma. This was shown for mylar in the earlier experiments, and it was found that during the time relevant to the absorption spectrum, 80% of the neon plasma is still unperturbed [31]. Nevertheless, a uniform slab geometry is a reasonable place to begin in order to gain some insight into the nature of the plasma created in these experiments. The measurements extracted through these assumptions will provide values that are representative of a space-average along the LOS over the entire extent of the neon plasma.

The time dependent nature of the experimental plasma also creates some issues that must be addressed. As has been mentioned, the focus of the analysis in this thesis is on the time-integrated data. Measurements of the plasma parameters made from time-integrated data will be representative of a time-average of those parameters over the course of the experiment. What would be expected is that those average values would be weighted toward values near the peak of the radiation drive because most of the radiation contributing to the spectrum comes from that time period. Simulations with the atomic kinetics code *Atokin* [48] have been used to get an idea of how the time-integration of the time-integrated spectrum will affect the measurement results, and this is what was found. Further work with the time-resolved data will reveal more information about the time-dependent nature of the plasma created in these experiments.

4.3 Transmission Calculation

The calculation of the transmission spectrum via Equation 4.3 is at the heart of understanding the plasma created in these experiments. All of the complexity required for this goes into the calculation of the optical depth τ_ν. The optical depth relates to the mean-free path ℓ_ν of a photon in the material and the opacity κ_ν of the material as

$$\tau_\nu = \frac{L}{\ell_\nu} = \kappa_\nu L \tag{4.4}$$

where L is the thickness of the slab and the use of the subscript ν indicates that these quantities are photon energy dependent. The most illuminating interpretation of the optical depth comes from its relationship to the mean-free path, the average distance through a material that a photon of a given energy is likely to travel before being absorbed by the material. This interpretation says that the optical depth at

a particular photon energy is the ratio of the length of the plasma to the average distance at which a photon with that photon energy is likely to be absorbed. There are two extreme cases for the optical depth in light of this interpretation. In the case that $L \gg \ell_\nu$, the plasma is "optically thick", in which case nearly all the photons of energy $h\nu$ that pass into the plasma will be absorbed. In the opposite case, $L \ll \ell_\nu$, the plasma is "optically thin" and most of the photons of this energy will pass through unimpeded.

The opacity and mean-free path relate to the cross-section of interaction of a photon with a particle in the material as

$$\kappa_\nu = \frac{1}{\ell_\nu} = \sigma_\nu N \tag{4.5}$$

where σ_ν is the cross-section and N is the particle number density of the material. This is the basic relationship between these quantities. In actuality, there are many line transitions associated with a few different ion stages in plasma. These all have to be accounted for when computing the spectrum.

If one considers the contributions to the transmission at a given photon energy from one line transition at a time, then the total transmission will be the product of all of the different contributions.

$$T_\nu = \prod_i T_{\nu i} = e^{-\sum_i \tau_{\nu i}} \tag{4.6}$$

Therefore, the total optical depth becomes the sum of all its contributions.

$$\tau_\nu = \sum_i \tau_{\nu i} = \sum_i \kappa_{\nu i} L = \kappa_\nu L \tag{4.7}$$

where the slab thickness L is a constant common to all contributions.

For the total opacity κ_ν, one must consider where each contribution comes from. Namely, there are at least four different ion stages in the plasma contributing transitions to the spectrum. The number density N as written in Equation 4.5 can refer to particles of only one particular type. Each contributing $\kappa_{\nu i}$ will have its own number density N_i, which refers to the number density of neon ions of a particular charge-state, and furthermore, to only those ions in the particular lower level associated with the absorption transition being considered in that contribution. These different number densities are ultimately what will be measured in the analysis, but instead of including all of the N_i for all of the fine structure lower levels, some assumptions can be made to limit that number to just the main configurations of the lower levels associated with the transitions. This is only applicable to Li- and Be-like ions, since they are the only ones in which transitions arise from non-ground-state levels. Additionally, in order for these N_i to be useful for relating to the totals of any of the ion species in the plasma, another assumption must be made. Let us briefly discuss these assumptions.

While there are many atomic structure levels available in each ion stage to be populated, an assumption is being made in this analysis that most of the population is in the ground and lowest excited states of each ion stage, and that the population of all upper states is negligible. This assumption comes from the fact that the separation in energy between these lower and upper states is large enough and the electron temperature and density is low enough that the upper states are not populated by collisional excitation. With this assumption, the value of the number density of, for example, the H-like ground state population, is equivalent to the total H-like neon number density. Similarly for the He-like neon population, the only level from which absorption transitions arise in this analysis is the ground state. However, there are multiple levels from which transitions can arise in Li- and Be-like neon.

Recall that Li-like neon has two configurations, one of which has two fine structure levels. There is a number density associated with each of these three levels for Li-like neon; however, while the TREX can resolve line features associated with each configuration, it cannot resolve the fine structure components. Therefore, the number densities associated with the fine structure levels must be combined, which requires another assumption. This assumption is that the fine structure levels which act as the lower levels in the line transitions are statistically populated through thermal equilibrium. This is a good approximation because the difference in energy between these levels is small compared to the electron temperature. What this means for the number density of that configuration is that when computing the contribution to the opacity from one of these fine structure levels, one must use only a fraction of the number density associated with that configuration. That fraction is obtained from the statistical weight $g = 2J + 1$ of the fine structure level that is the lower level of the transition. Thus, the Li-like levels $1s^2\ 2p\ {}^2P_{1/2}$ and $1s^2\ 2p\ {}^2P_{3/2}$ will receive 1/3 and 2/3, respectively, of the configuration number density associated with $1s^2\ 2p$. This applies similarly to the Be-like number densities, except that there are three configurations, in which the two excited states have four and five fine structure levels each. To obtain the total Li- and Be-like neon number densities, the configuration number densities from each can simply be added together. From here forward, the index i will be used to refer to these configurations.

For each of the configuration number densities N_i in κ_ν, there is an effective total cross-section $\sigma_{\nu i}$ as a function of photon energy, itself a sum of the contributions from each of the line transitions associated with that configuration. I use the word "effective" here because within these total cross-sections, I will include the fractions that are to be applied to N_i for a given line transition. Modifying Equation 4.5 to

include the sum over configurations gives

$$\kappa_\nu = \sum_i \sigma_{\nu i} N_i \tag{4.8}$$

The effective total cross-section for a given configuration i is given by

$$\sigma_{\nu i} = \sum_j \frac{\pi e^2}{mc} f_{ij} \phi_{\nu ij} F_{ij} \tag{4.9}$$

where e is the electron charge, m is the electron mass, and c is the speed of light. The presence of these constants in the cross-section along with much of the other information in this section comes from D. Mihalas [49]. Each index j refers to a transition within the set of transitions relating to configuration i. For a given transition ij, f_{ij} is the absorption oscillator strength, $\phi_{\nu ij}$ is the photon energy dependent line profile, and F_{ij} is the fraction that must be applied to the configuration number density N_i. The only time $F_{ij} \neq 1$ is when the lower level of the transition is one of the low excited states in Li- or Be-like neon. The absorption oscillator strengths are obtained from calculations done with the Flexible Atomic Code (FAC) [50].

Before delving into the details of $\phi_{\nu ij}$, the total optical depth can now be summarized as

$$\tau_\nu = \sum_i \sum_j \frac{\pi e^2}{mc} f_{ij} \phi_{\nu ij} F_{ij} N_i L. \tag{4.10}$$

The quantity $N_i L$ at the end of this equation is called the "areal density" or "column density" in an astrophysical context. There is one areal density corresponding to each configuration, which are the main quantities that are varied during the analysis to determine the populations associated with each configuration.

4.3.1 Voigt Line Profiles

The transitions between atomic levels in the ions occur for particular energies determined by the difference in energy of the atomic levels. However, there is broadening of the lines due to multiple effects. These include natural broadening, Doppler broadening, and Stark broadening. Natural broadening comes from the quantum mechanical nature of line transitions and the uncertainty that is inherent to the energy levels involved due to Heisenberg's uncertainty principle. Doppler broadening occurs due to the microscopic thermal motion of the ions. Finally, Stark broadening is due to Coulomb interactions with the electric micro-fields from the other particles in the plasma and becomes relevant for higher pressures. In our first approach, Stark broadening is neglected because the experiments are in a regime of low pressures, but we are finding evidence that this may be important to include in some cases. This will be discussed in Section 4.7. For now, the concentration will be on including natural and Doppler broadening in the calculation of the transmission spectra. The combination of these two broadening mechanisms produces what is known as a Voigt profile.

Line broadening can be included in the calculation of the transmission as the photon energy dependent line profile ϕ_ν for each transition separately. This profile, as it appears in Equation 4.10, is normalized in the frequency domain such that

$$\int_{-\infty}^{\infty} \phi_\nu d\nu = 1 \tag{4.11}$$

which means the photon energy dependent absorption cross-section associated with a particular transition with absorption oscillator strength f is then

$$\sigma_\nu = \frac{\pi e^2}{mc} f \phi_\nu. \tag{4.12}$$

However, the line profiles as we calculate them are normalized in the photon en-

ergy domain, which slightly alters a few of the definitions to follow. This will be summarized near the end of this section.

Natural broadening is described by a Lorentzian profile. This can be derived either by picturing the atom as a damped classical oscillator, or quantum mechanically by considering the finite lifetime of the atomic states involved in the transition. The resulting Lorentzian profile in the frequency domain is [49]

$$L(\nu;\nu_0,\Gamma) = \frac{1}{\pi}\left[\frac{(\Gamma/4\pi)}{(\nu-\nu_0)^2+(\Gamma/4\pi)^2}\right] \tag{4.13}$$

where ν is the frequency, ν_0 is the frequency at line center, and $\Gamma/2\pi$ is the FWHM of the Lorentzian in units of frequency. In the case of a transition between a ground state and an excited state, and if the excited state has only a single channel of decay, then $\Gamma = A_{ji}$, which is the spontaneous decay rate (i.e. the reciprocal of the mean lifetime of the excited state). This can be related to the approximate energy-time uncertainty relation $\Delta E \Delta t \sim \hbar$, which says that the uncertainty of the energy of the excited state is

$$\Delta E = h\Delta\nu \quad \sim \quad \frac{\hbar}{\Delta t} = \hbar A_{ji} = h\frac{A_{ji}}{2\pi} = h\frac{\Gamma}{2\pi}. \tag{4.14}$$

Thus, the width Γ in the frequency domain is related to the width of uncertainty in the energy of the excited state. If there are multiple channels out of the excited (upper) state U, which could include spontaneous decay and autoionization, then $\Gamma_U = \sum_i A_{Ui}$, which includes the rates from all spontaneous channels out of the excited state. Furthermore, if the transition is between two excited states, as is the case for some of the Li- and Be-like transitions, then the lower state L will also have a width Γ_L associated with it of the same form as for Γ_U and the total width Γ will

be the sum of the two,

$$\Gamma = \Gamma_L + \Gamma_U \equiv A_{tot}. \tag{4.15}$$

The A_{ji} that contribute to A_{tot} also come from calculations done with FAC [50].

Doppler broadening is due to the microscopic thermal motions of the ions in the plasma. The absorption by each ion will be Doppler shifted by its velocity relative to the observer along the observer's LOS. The overall effect on the spectrum accounting for all the ions in the plasma is the broadening of the spectral line by the probability distribution of velocities in the plasma along the LOS. Assuming that the velocity distribution of the plasma is Maxwellian with temperature T, then the probability of an ion having a velocity between ξ and $\xi + d\xi$ along one LOS is given by

$$G(\xi)d\xi = \frac{1}{\xi_0\sqrt{\pi}} \exp\left(\frac{-\xi^2}{\xi_0^2}\right) d\xi \tag{4.16}$$

where ξ_0 is the most probable velocity in the Maxwellian distribution and is given by

$$\xi_0 = \sqrt{\frac{2kT}{M}} \tag{4.17}$$

where k is Boltzmann's constant and M is the ion mass. Including this effect will further spread each point of the Lorentzian profile from natural broadening. This can be done through a convolution integral by including the Doppler shifted frequency as seen by the absorbing ion in the ion's frame. At a given frequency ν in the spectrum, an ion with LOS velocity ξ will be absorbing light of frequency $\nu(1 - \xi/c)$ in the ion's frame, and the corresponding absorption cross-section for that event in the ion's frame is

$$\sigma_\nu = \frac{\pi e^2}{mc} f L\big(\nu(1 - \xi/c)\big). \tag{4.18}$$

Thus taking into account all the ions by using the distribution of velocities $G(\xi)$ with

integration over the velocity, the convolution integral for the line profile observed in the spectrum is

$$\phi_\nu = \int_{-\infty}^{\infty} L\big(\nu(1-\xi/c)\big)G(\xi)d\xi. \tag{4.19}$$

The combination of Lorentzian and Gaussian profiles produces the Voigt profile.

To come to the common definition of the Voigt profile, Equations 4.13 and 4.16 are substituted into Equation 4.19. During simplification, the following quantities are defined:

$$y \equiv \frac{\xi}{\xi_0} \tag{4.20}$$

$$u \equiv \frac{\nu - \nu_0}{\Delta\nu_{_D}} \tag{4.21}$$

$$a \equiv \frac{\Gamma}{4\pi\Delta\nu_{_D}} \tag{4.22}$$

where the "Doppler width" $\Delta\nu_{_D}$ is defined as

$$\Delta\nu_{_D} \equiv \frac{\nu_0\xi_0}{c} = \frac{\nu_0}{c}\sqrt{\frac{2kT}{M}}. \tag{4.23}$$

In obtaining the following form, there is also the approximation that $\nu\xi_0/c \approx \nu_0\xi_0/c = \Delta\nu_{_D}$, or in other terms, that $\nu/\nu_0 \approx 1$. The Voigt profile then becomes

$$V(\nu; a, u) = \phi_\nu = \frac{H(a,u)}{\Delta\nu_{_D}\sqrt{\pi}}, \tag{4.24}$$

which is normalized according to Equation 4.11 and

$$H(a,u) \equiv \frac{a}{\pi}\int_{-\infty}^{\infty} \frac{e^{-y^2}}{(u-y)^2 + a^2}dy \tag{4.25}$$

is the common definition of the Voigt function.

The above discussion of the line profile was all in terms of frequency ν; however,

our calculations are all done in terms of photon energy $h\nu$, which requires some slight modifications to the equations above that should be noted.

To start, the line profile ϕ_ν above has units of $[\mathrm{Hz}^{-1}] = [\mathrm{s}]$, and it is normalized in the frequency domain according to Equation 4.11. Our line profile — let us call it $\phi_{h\nu}$ — will have units of $[\mathrm{eV}^{-1}]$, and is normalized in the photon energy domain such that

$$\int_{-\infty}^{\infty} \phi_{h\nu} dh\nu = 1 \tag{4.26}$$

with the result that

$$\phi_\nu = h\phi_{h\nu}. \tag{4.27}$$

This can be used directly with Equation 4.10. The normalized Voigt profile then becomes

$$V(h\nu; a, u) = \phi_{h\nu} = \frac{H(a,u)}{\Delta h\nu_{_D}\sqrt{\pi}}, \tag{4.28}$$

with

$$a \equiv \frac{\hbar A_{tot}}{2\Delta h\nu_{_D}} \tag{4.29}$$

$$u \equiv \frac{h\nu - h\nu_0}{\Delta h\nu_{_D}} \tag{4.30}$$

and

$$\Delta h\nu_{_D} \equiv \frac{h\nu_0 \xi_0}{c}. \tag{4.31}$$

To compute the Voigt profile during the analysis, the analysis code uses a subroutine which follows the procedure of Drayson [51].

4.3.2 Instrumental Resolution

The transmission spectrum as calculated from everything above is representative of the transmission of the radiation drive after passing through a slab of plasma with some given conditions. If the spectrometer used to record the spectrum had infinite spectral resolution and could resolve all the details, this is the spectrum it would see. But the spectrometer itself also affects the spectrum. There are many components in the TREX spectrometer which interact with the light as it passes through and is recorded. This affects the spectrum in a way that can be modeled as an extra convolution of the ideal spectrum from above with an instrumental function.

For the TREX, the instrumental function used is a normalized Gaussian distribution. The final synthetic transmission spectrum would be

$$\widetilde{T}_\nu(h\nu) = \int_{-\infty}^{\infty} T_\nu(h\nu - h\nu')G(h\nu')dh\nu'. \tag{4.32}$$

where

$$G(E) = \frac{1}{\sigma\sqrt{2\pi}} \exp\left(-\frac{E^2}{2\sigma^2}\right) \tag{4.33}$$

with the standard deviation σ related to the FWHM ΔE of the Gaussian distribution by

$$\sigma = \frac{\Delta E}{2\sqrt{2\ln 2}}. \tag{4.34}$$

For this analysis, ΔE is taken to be constant over the range of the spectrum. This assumes that the resolution power R of the TREX varies according to photon energy E as $R = E/\Delta E$.

This instrumental function is directly integrated with the calculated spectrum to produce the final transmission spectrum. This result can be compared to a transmission spectrum that has been extracted from experimental data.

4.4 Areal Density Extraction

The main quantities that are necessary to characterize the plasma in the experiments are the configuration number densities from each ion species and the electron temperature. The densities N_i are obtained from measuring the areal densities $N_i L$ in Equation 4.10 through a least-squares fitting procedure that compares the synthetic spectrum with the experimental spectrum. The temperature, however, is not measured directly from fitting the spectrum, because the dependence of the features in the spectrum on temperature is minor. The method for temperature extraction is explained in Section 4.5. But the temperature T is required for the calculation of the transmission spectrum because it determines the amount of Doppler broadening that there is in the spectrum. Through hydrodynamic simulations and observations from our measurements, a representative value has been arrived upon and used as a constant in the measurements discussed in Chapter 5.

Another parameter whose value is required for the transmission calculation is the FWHM ΔE of the instrumental broadening function. This is taken to be constant across the spectral range. The value used was determined from some tests that involved the Ly-β line feature.

The other information needed for the calculation of the transmission are either well defined constants or are obtained, as discussed above, from calculations of the atomic structure of the neon ions from FAC [50].

With all the necessary information for the transmission calculation, measurements of the set of configuration areal densities can be obtained. The program to perform the fitting for retrieval of the measurements is ran separately for optimization of the configuration densities for one ion at a time. That is, once for H-like, once for He-like, once for the two populations of Li-like, and once for the three populations of Be-like. Initial guesses for the areal densities of all configurations are provided as input to

the program by the user, along with all other values needed for the calculation. Also given as input is a flag telling which ion to run the optimization for, what photon energy ranges to consider during the optimization, and information to create a grid of areal densities to search through for the optimization. The value or values given as the best-fit result will be from this grid.

The code starts by calculating the spectrum using the initial densities. As was mentioned in Section 3.2.3, the line features in the experimental transmission may not exactly match the theoretical photon energy values from FAC, so this initial spectrum is used to align the features in the synthetic spectrum with the features in the experimental data. This is done by using centroids in a very similar manner as explained for the centroids method for fine adjustments in Section 3.2.3, except that there is no human interaction and the ranges necessary for the centroids are provided to the program from an input file. After the line features have been aligned, the optimization phase begins.

The grid of areal density values to be searched is created based on two values giving the range of areal densities to be included in the grid and a value telling the number of intervals in the grid. It will be 1-D for H- and He-like, 2-D for Li-like, or 3-D for Be-like. Each dimension in the grid corresponds to each of the configurations of the ion being fitted and has the same set of possible areal densities. The spectrum is recalculated using the densities of each point in the grid, and for each point a Q^2 value is computed based on the regions of the spectrum that are indicated to be included in the optimization. For example, when fitting the H-like neon series, regions containing the Ly-α and/or Ly-β line features can be included. The Q^2 value for each point is

$$Q^2 = \sum_i \Big(T_\nu(h\nu_i) - T_{exp}(h\nu_i) \Big)^2 \tag{4.35}$$

where $T_\nu(h\nu_i)$ is a value that is interpolated from the synthetic transmission spectrum

at the photon energy $h\nu_i$ in the experimental spectrum T_{exp}, and only photon energies within the regions to be included in the optimization are included in the calculation of Q^2. The point with the minimum Q^2 value is found and the areal densities associated with that point are returned as the best-fit result.

The sequence taken in finding the whole set of configuration areal densities is to begin with the H-like series, because it is isolated from the other series. Next, the He-like series is fitted, since it is mostly isolated. Following this, the Li-like series is fitted. Since the He-like series and Li-like overlap at the He-γ line, if this line is being included in the fitting region for the He-like series, then the He-like and Li-like series may be fitted again to converge toward an improved fit. Generally it converges for two significant figures with just these two iterations. Finally, the Be-like series is fitted last. When working with each series, the range given for the areal density grid starts broad, and multiple fits will be done during which the grid range will be reduced each time, thereby increasing the areal density search resolution with each pass. The time to complete each fitting is directly dependent on the number of areal density grid points in the search. This means that if the number of intervals given as input is N, then for the H-like and He-like series, the time t is proportional to N; for the Li-like series, $t \propto N^2$; and for the Be-like series, $t \propto N^3$. The H-like and He-like series can be done quickly, on the order of minutes, which is another reason they are done first. Due to the fact that each dimension of the multi-dimensional areal density grids are the same, this means that, for example, Li-like fitting can take on the order of hours, depending on the resolution desired. This is because the two configuration areal densities can be quite different, by a factor of up to three, theoretically (see next section). The Be-like fitting, with the current code, can sometimes take on the order of a day or two. This is one aspect of the current code that can be improved rather easily by allowing for individual ranges for each dimension.

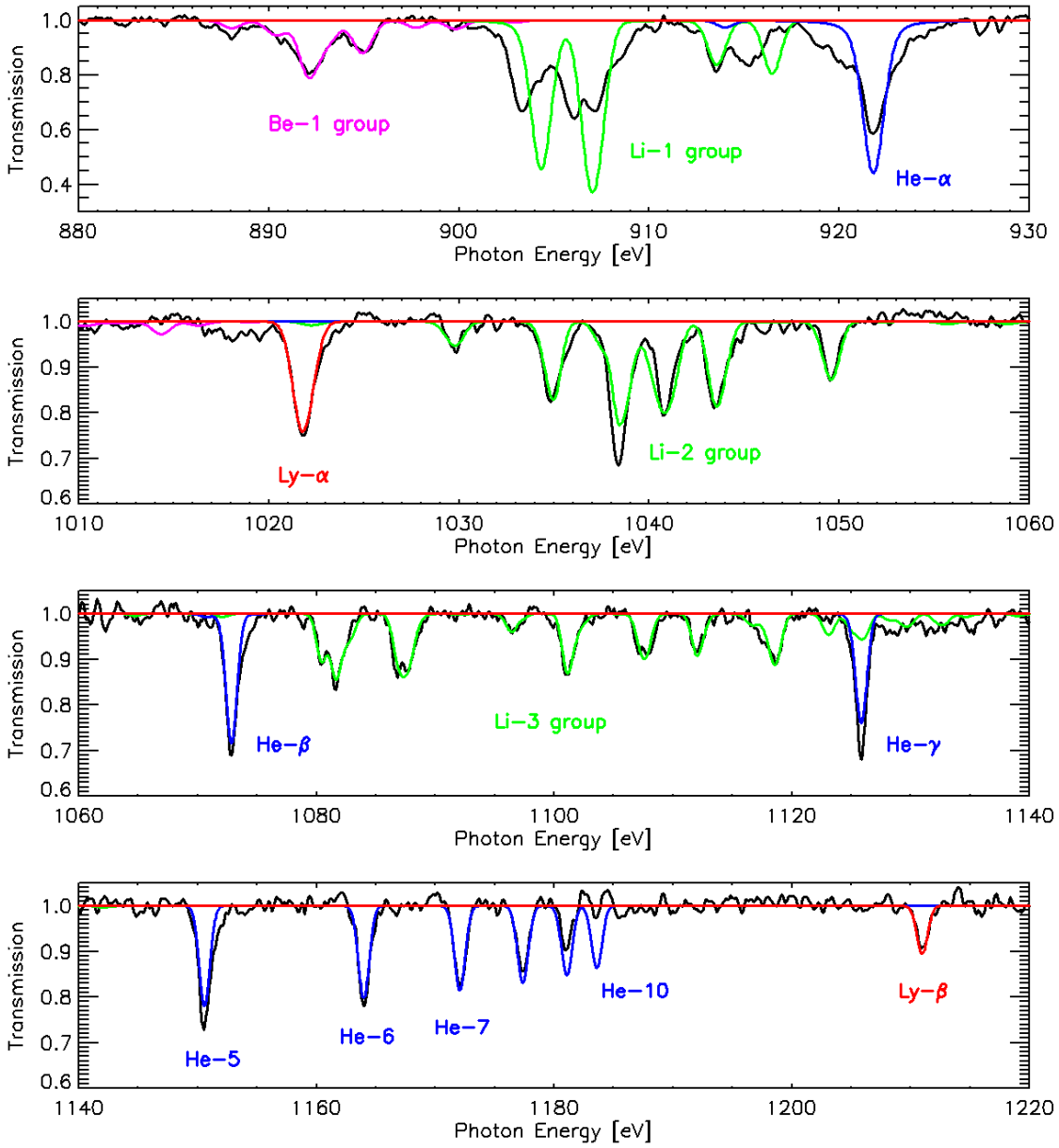

Figure 4.3: Fitted spectrum of shot z2222 side b showing each ion contribution separately. Shown in red is the H-like neon Lyman series, blue is the He-like neon series, green is the Li-like neon satellites, and pink is the Be-like satellites. The experimental transmission is shown in black. Note that He-α and the Li-1 group are not used in the fit. For this particular fit, He-10, Li-2.3, and Li-2.4 were also not included.

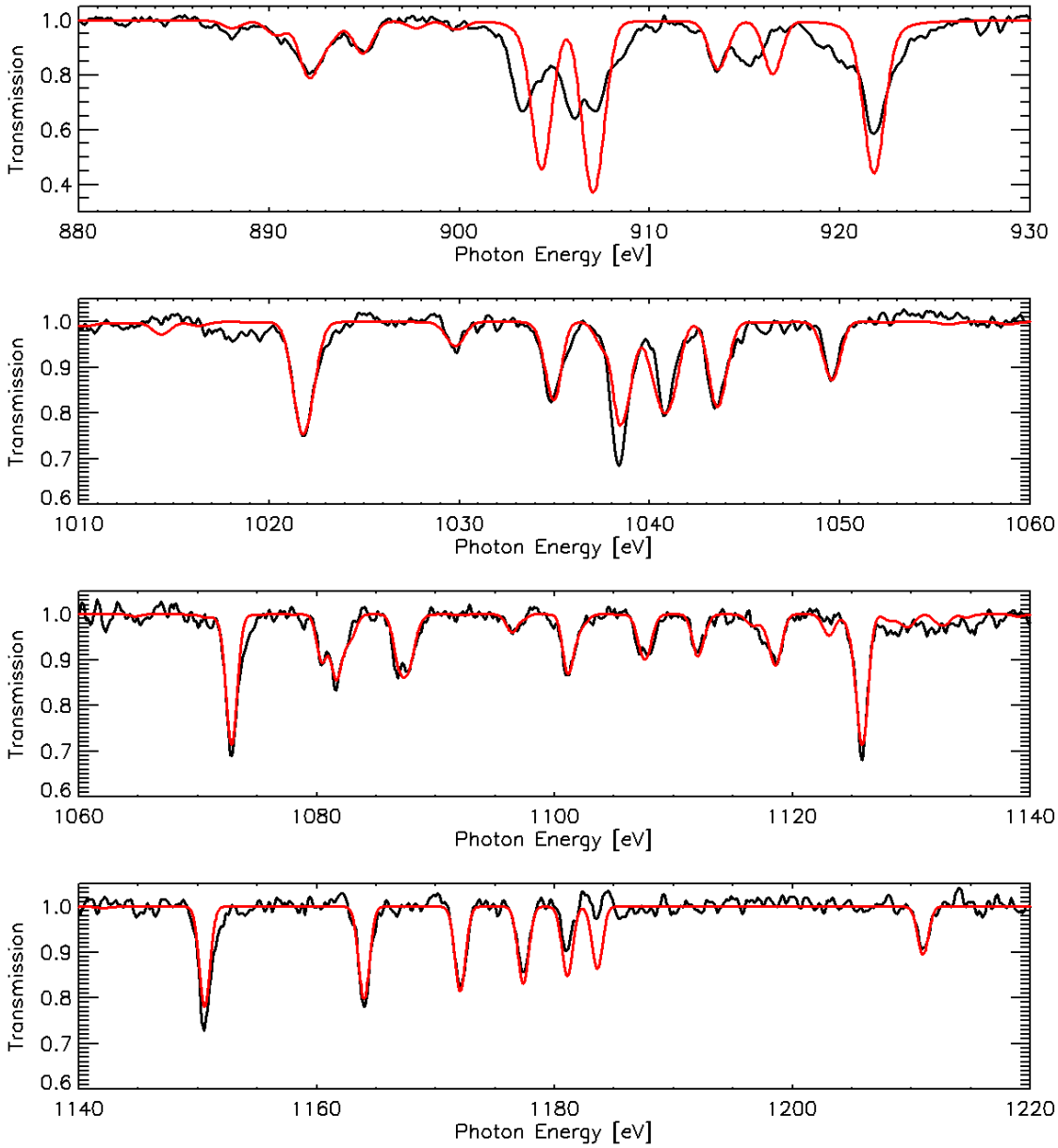

Figure 4.4: Final spectral fit for shot z2222 side b after combining all contributions shown in Figure 4.3.

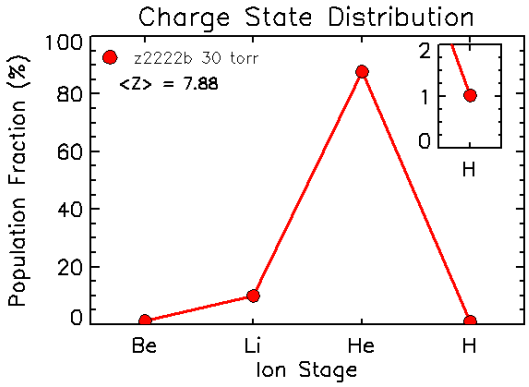

Figure 4.5: Charge state distribution showing the fractional population associated with each ion stage. The average ionization described in Equation 4.36 is shown as $\langle Z \rangle$.

Figure 4.3 shows the fitted spectrum for shot z2222 side b from each ion stage drawn separately. The red trace is the H-like neon Lyman series, blue is the He-like ion series, green is the Li-like satellites to the He series, pink is the Be-like satellites, and the experimental transmission is shown in black. The He-α and Li-1 group, at this time, are never used in the fit because of problems from saturation, a possibly higher level of second order reflection photons, and Si absorption contamination. The latter two of these may also affect the Be-like fit as well and need to be accounted for in future work. Also for this particular transmission He-10 was not included because it may just be noise or an artifact, and Li-2.3 and Li-2.4 were not included because they often significantly mismatch for a hitherto unknown reason. Figure 4.4 shows the final spectral fit combining the contributions from each of the four ions.

In the end, if all four ions are fitted, then seven configuration areal densities will be obtained. The two Li-like areal densities and the three Be-like areal densities can be summed to obtain the total Li-like and Be-like areal densities respectively. Using the total neon areal density, each individual areal density can be related to fractional populations that can be associated with each ion configuration or with

each ion species. This factional distribution of ion populations is referred to as the "charge state distribution". An example of this is shown in Figure 4.5.

Using the fractional populations f_i for each ion species from the charge state distribution and the number of electrons remaining for each ion stage Z_i, one can compute the average ionization, $\langle Z \rangle$ or $\bar{Z}$, of the plasma.

$$\bar{Z} = \sum_i f_i Z_i \tag{4.36}$$

This is a weighted average using the fractional populations as the weights with the condition that $\sum_i f_i = 1$.

The total neon number density can be obtained from measurements of the gas cell pressure by using the Ideal Gas Law at room temperature, which is

$$P = nkT, \tag{4.37}$$

where P is the pressure, n is the particle number density (Note: capital N has been used throughout this thesis to denote this quantity), k is Boltzmann's constant, and T is the temperature in units of Kelvins. The length L of the plasma along the LOS is known from the dimensions of the gas cell, which can be used to relate number densities N and areal densities NL. The total neon areal density can also be obtained by summing all of the individual measured ion areal densities from the analysis with the assumption that the populations of other ion species that were not considered are negligible. Simulations and observations of the experimental spectra have shown that it is a good approximation to assume that ion populations other than those discussed here would be very small. These two independent methods of obtaining totals for the total neon density can be used as a consistency check later on, and may indicate whether other factors may be at play in these experiments.

4.5 Temperature Extraction

As was mentioned in the previous section, the temperature is not measured directly from fitting the transmission. That is, at no time while making general measurements from the data is the temperature varied in the calculation while all the densities are held constant. The reason this is not done is because in the calculation of the spectrum, the temperature only directly influences the Doppler broadening of the lines, and the effect is fairly small as compared with the instrumental resolution of the TREX instrument. There has been a few tests run on the Ly-β line to see if a temperature could be extracted in this way using an isolated line that is not saturated, but the sensitivity of this method was not sufficient enough to be useful.

Instead, the temperature can be extracted by utilizing the balance in the two populations associated with the Li-like configurations. A temperature can also be extracted similarly by examining the three populations of the Be-like configurations.

4.5.1 Extraction from Li-like Populations

For the purpose of the following discussion, let us define the Li-like neon fractional populations associated with the $1s^2$ 2s and $1s^2$ 2p configurations as P_s and P_p respectively. By making the assumption that these two configurations are in thermal equilibrium, the ratio of the two populations can be related to the temperature using Boltzmann factors.

$$R = \frac{P_p}{P_s} = \frac{g_p \exp(-E_p/kT)}{g_s \exp(-E_s/kT)} \tag{4.38}$$

where g_s and g_p are the statistical weights associated with each configuration ($g = 2J+1$), E_s and E_p are the energies associated with each configuration, and kT is the electron temperature, because the electrons are the particles driving the population

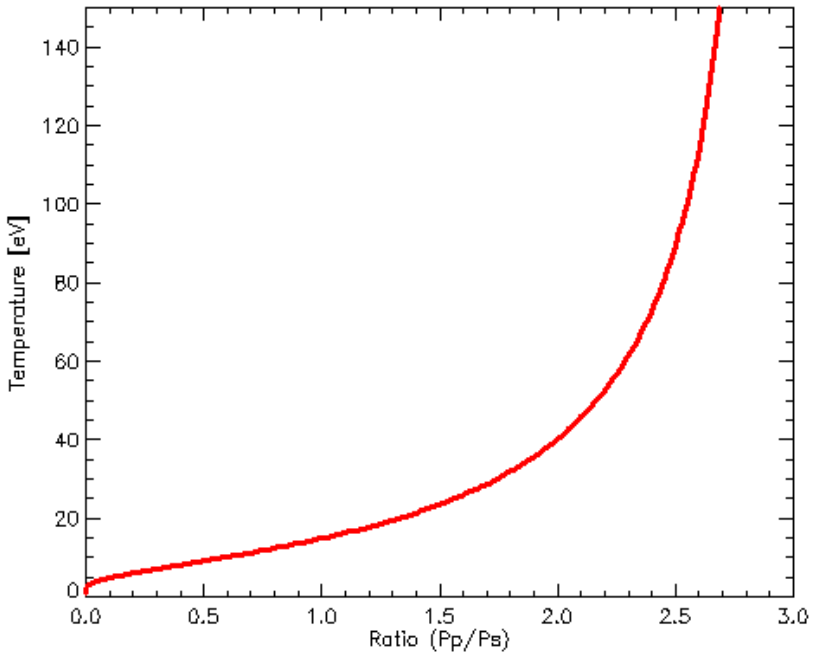

Figure 4.6: Extracted temperature versus Li-like neon population ratio P_p/P_s.

to upper levels through collisions. The statistical weights are

$$g_s = 2 \tag{4.39}$$

$$g_p = g_{p_{1/2}} + g_{p_{3/2}} = 2 + 4 = 6, \tag{4.40}$$

which means that the ratio P_p/P_s tends toward a value of 3 at high temperatures. The difference between the energies $\Delta E = E_p - E_s = 16.3$ eV, using the configuration average for E_p. The temperature kT is then

$$kT = \frac{\Delta E}{\ln\left(\frac{g_p}{g_s}\frac{P_s}{P_p}\right)} = \frac{16.3}{\ln(3P_s/P_p)} \tag{4.41}$$

in units of eV. Figure 4.6 shows the curve of temperatures extracted versus the ratio P_p/P_s. Note that above a ratio of around two, the extracted temperature begins to

rise very quickly, which means that for extracted population ratios in that range, the temperature extracted will have much larger uncertainties. This can be seen in a more quantitative fashion by looking at the relationship between variations in the population ratio and temperature. Defining $g \equiv g_p/g_s$, Equation 4.38 can be rewritten as

$$R = g \exp\left(\frac{-\Delta E}{kT}\right). \tag{4.42}$$

A variation in R will be

$$\delta R = R\frac{\Delta E}{(kT)^2}\delta(kT). \tag{4.43}$$

Rearranging this to give the ratio of variation in temperature with respect to the extracted temperature (i.e. the relative uncertainty) gives

$$\frac{\delta T}{T} = \left(\frac{kT}{\Delta E}\right)\frac{\delta R}{R}. \tag{4.44}$$

This shows that for temperatures measured greater than ΔE, the relative uncertainty of the extracted temperature is amplified linearly with the temperature itself, by the ratio $kT/\Delta E$, with respect to the relative uncertainty in the measured population ratio. This runaway effect in the uncertainty limits the range of usefulness for this temperature extraction method. Table 4.1 gives an illustration of the effect using an example of 10% relative uncertainty in the value of R.

$kT/\Delta E$	kT **[eV]**	R	$\delta R \equiv 0.1R$	$\delta(kT)$ **[eV]**
1	16.3	1.10	0.110	1.63
2	32.6	1.82	0.182	6.52
3	48.9	2.15	0.215	14.7
4	65.2	2.34	0.234	26.1
5	81.5	2.46	0.246	40.8

Table 4.1: Illustration of the runaway uncertainty effect using an example of 10% relative uncertainty in the ratio value.

Label	Level	Energy [eV]	g
0	$1s^2\ 2s^2\ {}^1S_0$	0	1
1	$1s^2\ 2s\ 2p\ {}^3P_0$	13.98	1
2	$1s^2\ 2s\ 2p\ {}^3P_1$	14.03	3
3	$1s^2\ 2s\ 2p\ {}^3P_2$	14.15	5
4	$1s^2\ 2s\ 2p\ {}^1P_1$	27.57	3
5	$1s^2\ 2p^2\ {}^3P_0$	36.46	1
6	$1s^2\ 2p^2\ {}^3P_1$	36.52	3
7	$1s^2\ 2p^2\ {}^3P_2$	36.63	5
8	$1s^2\ 2p^2\ {}^1D_2$	40.56	5
9	$1s^2\ 2p^2\ {}^1S_0$	50.52	1

Table 4.2: Details of the Be-like neon fine structure levels relevant for temperature extraction. The "Label" column indicates the index number to be associated with each level. The "g" column contains the statistical weights for each level.

Simulations with the atomic kinetics code *Atokin* [48], have shown that electron temperatures extracted via this method from both instantaneous and time-integrated synthetic spectra generated by *Atokin* give reasonable results. However, uncertainties related to data quality will have a large effect on the usefulness of this method in practice.

4.5.2 Extraction from Be-like Populations

For the temperature extraction involving the Be-like neon configuration ratios, the approximation using the configuration averages is not as good as it is for the Li-like case. Therefore, a more detailed calculation is preferred.

There are ten fine structure levels associated with the configurations concerned. The relevant details for these levels are given in Table 4.2. Let us label the quantities of each level, as indicated in the table, with a subscript from 0 to 9. The partition function for this system is

$$Z = \sum_{i=0}^{9} g_i \exp\left(-\frac{E_i}{kT}\right). \tag{4.45}$$

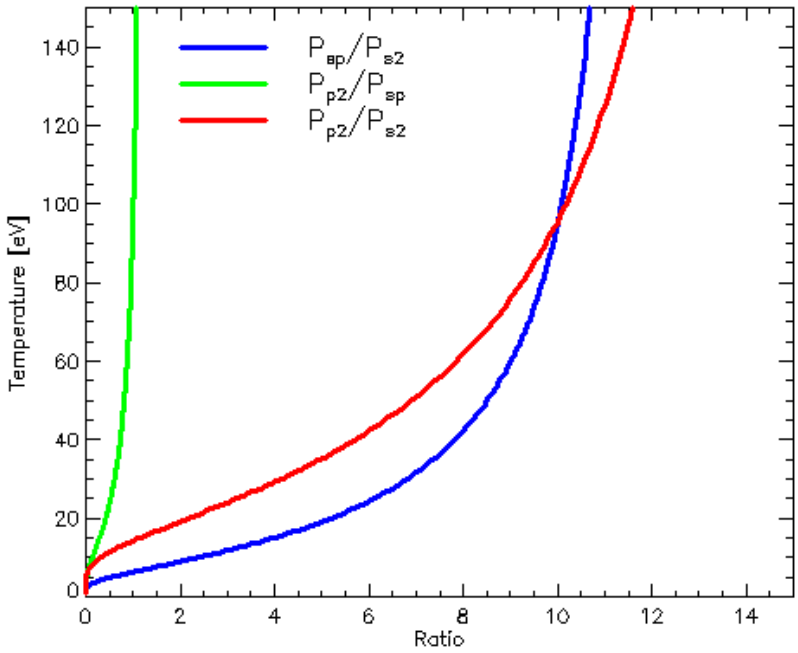

Figure 4.7: Extracted temperature versus the three possible Be-like neon population ratios.

The probability of the ith level being populated (i.e. fractional population) is

$$P_i = \frac{g_i \exp(-E_i/kT)}{Z}. \tag{4.46}$$

Now let us define the total fractional populations to be associated with each of the three configurations as P_{s2}, P_{sp}, and P_{p2} for the $1s^2\ 2s^2$, $1s^2\ 2s\ 2p$, and $1s^2\ 2p^2$ configurations, respectively. These quantities are

$$\begin{aligned} P_{s2} &= P_0 \\ P_{sp} &= P_1 + P_2 + P_3 + P_4 \\ P_{p2} &= P_5 + P_6 + P_7 + P_8 + P_9. \end{aligned} \tag{4.47}$$

There are three ratios possible from this set of fractional populations, namely

$$\begin{aligned} R_1 &= P_{sp}/P_{s2} \\ R_2 &= P_{p2}/P_{sp} \\ R_3 &= P_{p2}/P_{s2}. \end{aligned} \tag{4.48}$$

For a given combination of areal density or, equivalently, fractional population measurements from the experimental data, a temperature can be extracted using these ratios. The extracted temperature is plotted as a function of each of the population ratios in Figure 4.7. The blue trace is R_1, green is R_2, and red is R_3. Out of these, R_3 is the most useful. The reason for this can be seen by recalling Equation 4.44. Each of these ratio-temperature relationships will have uncertainties that, for simplicity and illustration, can be approximated similarly to the way it was done above by using the configuration average for the energies. The energies for the $1s^2$ 2s 2p and $1s^2$ $2p^2$ configurations are 17.46 eV and 38.83 eV, respectively. Ratio R_3 has the largest ΔE and therefore has the largest useful range of the three possible ratios from Be-like populations.

There is an important note that also must be made at this time. Due to the larger energy separation between some of these levels, and because of the fact that low densities are involved, the approximation that these levels are in thermal equilibrium is likely to be less accurate than for the Li-like levels. At this time, simulations have not yet been performed to assess how far from off this approximation might be.

4.6 Ionization Parameter Values

The ionization parameter $\xi = 4\pi I/N_e$ for a given shot is another quantity for which a measurement is desired. In the denominator is N_e, which can simply be calculated

using the filling pressure to get the neon particle number density N and multiplying this by the average ionization value $\bar{Z}$.

$$N_e = \bar{Z}N \tag{4.49}$$

The more difficult value to quantify in this case is the irradiance I due to the complexity of the radiation field and variation of this between shots. Mentioned in Section 2.3 were some simulations that were done in an effort to understand the radiation environment produced by the Z-pinch. Of particular interest are those of Ref. [33]. In these simulations, the spectral distribution and total irradiance was calculated at different times near the time of peak emission using data from shot number z2222. Calculations were done for a hypothetical gas cell placed at both the close and far positions, and the irradiance values correspond to the x-ray flux impingent upon the front window for each of these positions. This provides a good approximation to the radiation field of this particular shot, which happened to be at close position. The value for I for this shot would come from the peak irradiance value from the close position multiplied further by 80% due to the transmission through the heated Si_3N_4 window (Recall the discussion from Section 2.4.). This should provide the best approximation to the ionization parameter value at the peak of the radiation drive.

For the rest of the shots, the value of I from shot z2222 is scaled to more appropriately approximate the conditions in those particular shots. To obtain these scaling factors, time-resolved side-power measurements from the Total Energy and Power (TEP) diagnostic [52] were used. The peak value of the side-power from each shot was found, and the scaling factor for that shot is the ratio of this peak power to that of shot z2222. This provides coefficients for each shot to scale one of the two calculated irradiance values from shot z2222 to better approximate the irradiance

values for each shot depending on its position, as long as the Z-Machine is in the same configuration.

4.7 Stark Broadened Lineshapes

Two types of broadening were discussed above, natural and Doppler broadening, and the standard method of analysis takes into account only these two contributions. But the third broadening mechanism that was mentioned, Stark broadening, may also prove to be important to include in the analysis. Recall that Stark broadening effect is due to perturbations from the electric micro-fields generated by the other particles in the plasma. This has more significance for higher pressures and has a greater influence on higher members of a spectral line series. These higher series members involve higher atomic levels that are more weakly bound to the ion and are more affected by external fields.

The Stark effect is taught in introductory quantum mechanics courses for an isolated atom in a uniform electric field. In this case, there is a shift resulting to each of the atomic energy levels that is dependent on the strength of the field. In a plasma, however, there will be many ions emitting or absorbing radiation inside a pool of electrons all zipping and prancing about. The plasma itself is generally considered to be neutral since there should be a nearly equal number of positive and negative charges, and at a test point within the plasma there will be spherical symmetry on average. Fluctuations about this symmetric configuration will produce small electric "micro-fields" that will have a non-zero average magnitude, but the directions will average out. A given ion in this scenario could see any value of electric field within a certain distribution of possible electric field strengths. Depending on what value of the field is present at the ion when it absorbs or emits a photon, the levels in the ion will be shifted by some amount affecting the allowable energy of the

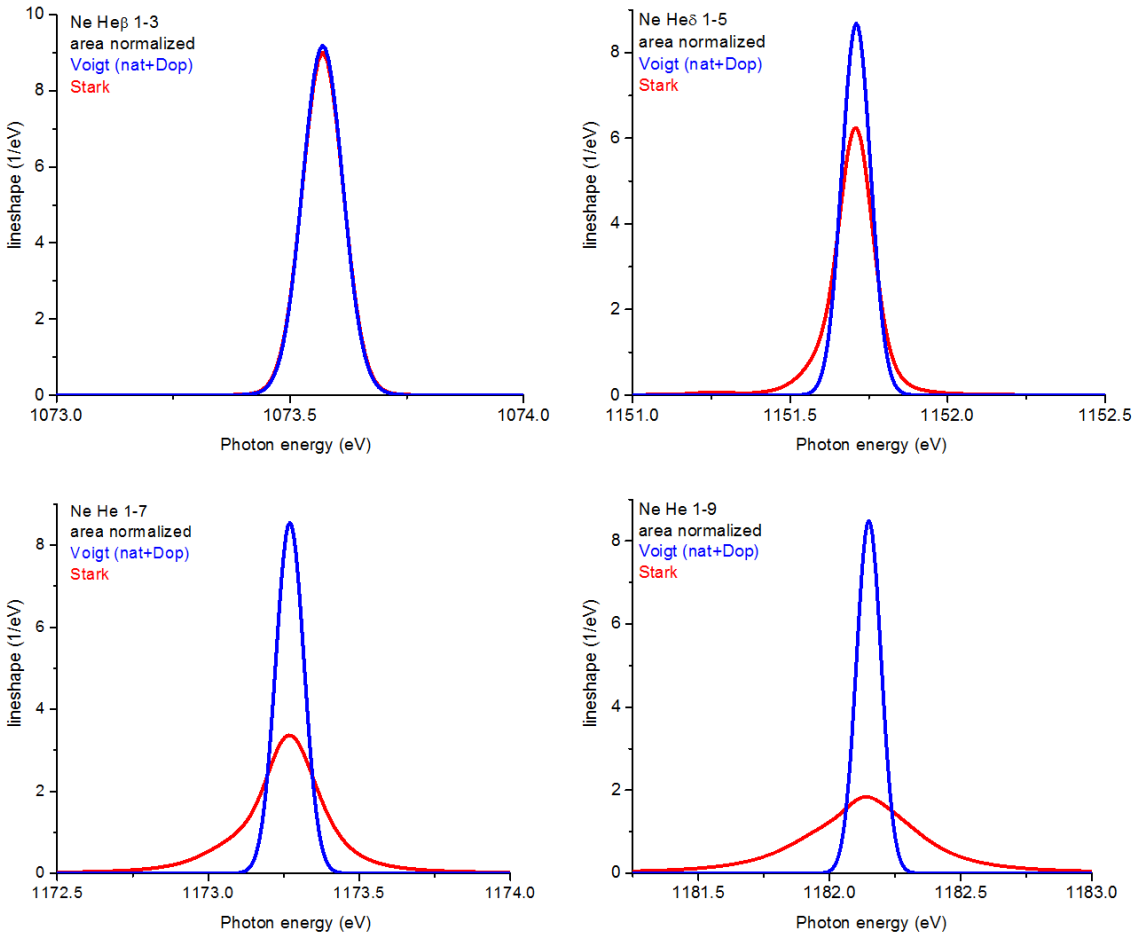

Figure 4.8: Stark broadened line profiles compared to the standard Voigt profiles for four of the members of the He-like neon series [54]. The Voigt profile is shown in blue, and the Stark broadened profile is in red.

photon that is emitted or absorbed. To obtain the Stark broadened line profile for a given transition, one must integrate over the effect of all of the possible electric micro-fields seen by the ions in the plasma, which would further broaden the Voigt profiles discussed above [53].

Four examples of Stark broadened line profiles calculated in the manner described by Refs. [55, 56] and computed by Ref. [54] are shown in Figure 4.8 in red, compared with Voigt profiles in blue. These line features are the He-3, He-5, He-7, and He-9 members of the He-like neon series. The effect of Stark broadening is greater for the

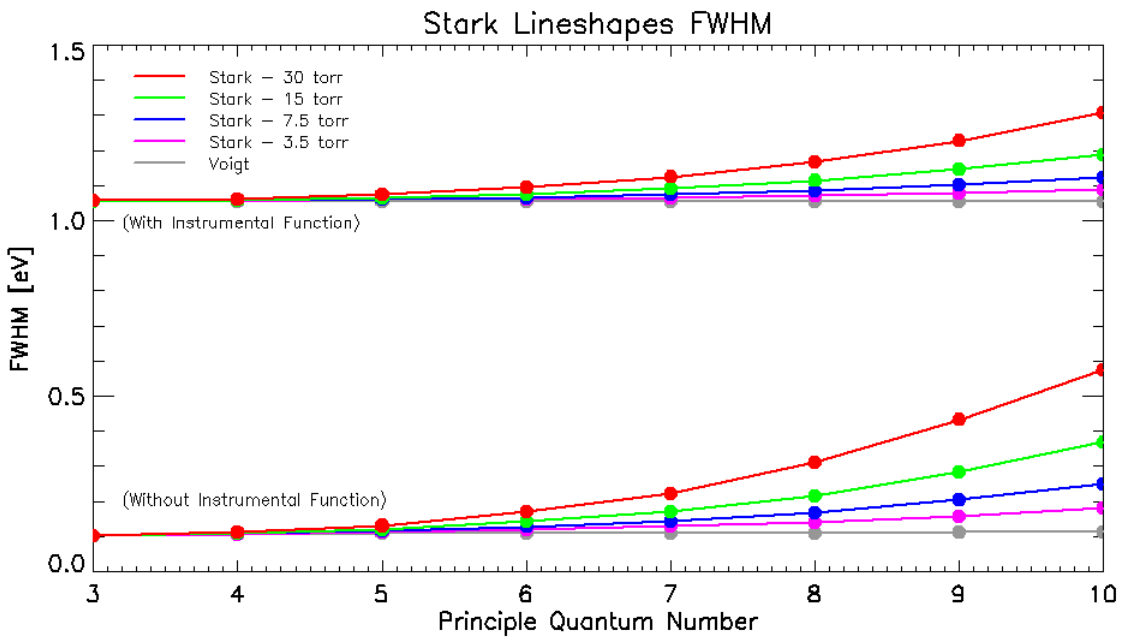

Figure 4.9: FWHM of Stark broadened line profiles for the He-like neon series for different filling pressures. The principle quantum number of the upper level in the transition (i.e. He-3, He-4, etc.) is along the horizontal axis. The lower group is the "pure" Stark broadened line profiles, and the upper group further convolves these with a 1.05 eV Gaussian instrumental function to simulate what would be seen by the TREX spectrometer. Red is for 30 torr, green is 15 torr, blue is 7.5 torr, and magenta is 3.5 torr. The gray trace shows the FWHM of Voigt profiles.

higher members of the series, while the lowest member of these sees very little effect at all.

The broadening also depends on the number density. Figure 4.9 shows a set of curves demonstrating this. On the horizontal axis is the principle quantum number of the upper level in the transition in the He-like neon series (i.e. He-3, He-4, etc.). On the vertical axis is the FWHM of the line in eV, which gives a sense of how much of an effect the Stark broadening has for a given line. There are two groups of traces. The lower group is the "pure" Stark broadened line profiles, while the upper group takes the pure line profiles and further convolves each of them with a 1.05 eV Gaussian instrumental function to simulate what would be seen by the TREX spectrometer.

The different curves within each group show the effect on the Stark broadening for different filling pressures. Red is the highest pressure of 30 torr, whereas magenta is for 3.5 torr. The gray trace shows the FWHM of the Voigt profiles for comparison. The Voigt FWHM stays almost constant throughout the series, while the FWHM for the Stark profiles increase with both higher series members and higher pressures.

For the tests that will be explained in Chapter 5, the Stark broadened profiles were calculated by Ref. [54] for the different filling pressures that appear in Figure 4.9. Each profile is area normalized, and contains all of the fine structure transitions that contribute to a given line feature, so they have to be treated slightly differently. When calculating the optical depth for a given line feature, referring back to Equation 4.10, the profile would be used as ϕ_ν and there would be a single oscillator strength f to go with it, which is the statistically weighted average of the oscillator strengths of the fine structure transitions that contribute to that particular line feature.

Chapter 5

Results

In this chapter, results will be presented from what are essentially test case scenarios for testing the various processing and analysis methods. While these results begin to give a flavor of the characteristics of the plasmas created throughout this experimental campaign, they are not yet considered to be of benchmark data quality. The main purpose of these test case scenarios are to identify areas that must be improved upon in the methods devised for data processing and analysis, in order to provide guidance toward finding the best practices to be used in creating a benchmark-worthy dataset.

While these results are not final, they do begin to paint a picture of the type of plasmas that are being created in this laboratory environment. Of the utmost importance is the evidence that shows that these plasmas are indeed photoionized. Trends are also identifiable which show how the plasma conditions change with changes to the parameters of the ionization parameter ξ. Other trends show where the processing and analysis methods must still be improved.

Shot Number	**TREX Side**	**Distance [cm]**	**Pressure [torr]**	ξ **[erg·cm/s]**
z2219	b	4.3	15.0 *	40.8
z2220	b	5.9	9.0 *	27.5
z2222	b	4.3	30.0 *	16.7
z2268	b	4.3	7.5 *	75.3
z2270	b	5.9	7.5 *	27.0
z2298	a, b	4.3	3.5 *	183.9
z2299	b	5.9	14.4	15.5
z2300	b	5.9	30.6	5.4
z2364	a	4.3	4.4	153.1
z2365	a	4.3	4.7	157.6
z2366	a	4.3	16.5	46.1
z2367	a	4.3	16.5	40.7
z2482	b	5.9	8.1	39.8
z2483	b	5.9	8.1	43.8
z2484	b	4.3	13.0	49.2
z2552	a, b	4.3	6.7	112.9
z2588	a, b	4.3	29.8	22.4

Table 5.1: Z shots included in this dataset organized by shot number and separated by shot series. The 'TREX side' column indicates whether data is used from both sides of the TREX instrument or from which side it came. The distances are from the center of the Z-pinch to the front of the gas cell. The pressures are the measured Neon gas fill pressures [37], except where marked by an asterisk (*); for these the intended fill pressures are given. The last column gives the ionization parameter values.

5.1 The Dataset

The data considered during the work for this thesis comes from experiments at the Z-Machine performed between June 2011 and December 2013, thus they are all of the second generation (GEN2) configuration of experiments. See Table 5.1 for a list of the shots included in this dataset and their basic parameters. The Z shot numbers are in the first column, and the second column indicates whether the data included here comes from both sides of the TREX spectrometer or from which side it comes. The third column shows the distance from the Z-pinch center to the front window of the gas cell. The fourth column shows the measured Neon fill pressures as measured by

	4.3 cm	**5.9 cm**
30 torr	z2222 z2588	z2300
15 torr	z2219 z2366 z2367 z2484	z2299
7.5 torr	z2268 z2552	z2220 z2270 z2482 z2483
3.5 torr	z2298 z2364 z2365	

Table 5.2: The dataset grouped according to the approximate distance-pressure combination for each shot.

Ref. [37]. Prior to shot z2299 — shots indicated by an asterisk (*) — the data required for this pressure measurement was not yet collected, so in these cases the intended fill pressure is given. Finally, the fifth column gives the values for the ionization parameter ξ calculated as discussed in Section 4.6. For the values of ξ, an estimate of $\bar{Z} \approx 8$ was used.

Table 5.2 organizes the shots by their distance and by which intended pressure their measured pressure is closest to. There are two different distances used: 4.3 cm and 5.9 cm, and four different intended filling pressures: 30 torr, 15 torr, 7.5 torr, and 3.5 torr.

The corresponding neon particle number density for a given pressure can be found by using the Ideal Gas Law in Equation 4.37. For example, using room temperature (i.e. 295 °K) for T, these four intended pressures correspond to neon particle number densities of 9.8×10^{17} cm^{-3}, 4.9×10^{17} cm^{-3}, 2.5×10^{17} cm^{-3}, and 1.1×10^{17} cm^{-3}, respectively.

The two distances used result in a radiation flux incident at the front window of

the gas cell that differs from each other by about a factor of two.

The column length L of the LOS through the neon gas is used to convert the areal density measurements into particle number densities. For the GEN2 style gas cells using the Si_3N_4 windows, this value is 1.37 cm.

For the calculations of the synthetic spectra a few numbers need to be provided. For the ion temperature associated with Doppler broadening, a temperature of 30 eV was used. This came from tests using the Ly-β feature as well as past work by Ref. [57]. The instrumental function used to model the spectral resolution power of the TREX spectrometer, is a Gaussian with a FWHM of 1.05 eV. This also came from tests using the Ly-β feature. Also recall that all atomic data (i.e. line positions, absorption oscillator strengths, radiative decay and autoionization rates, etc.) required for the calculation were calculated using the FAC atomic structure code.

5.1.1 General Comparisons

Not every shot in Table 5.1 was used when testing each of the major processing or analysis methods that were necessary to test. Table 5.3 summarizes which shots have associated data points in the results presented in this chapter for which only a limited number of shots were involved. Recall from Section 3.2.3 that there were two different methods for estimating the zero-level of absorption for the spectra. Namely, there was the BKGD and the BKGD-Null methods. Results that came from transmission data for which the zero-level of absorption was estimated by either BKGD-v1 or BKGD-v2 will be grouped together and presented with the label "BKGD", whereas results from transmission data which utilized null data for the zero-level of absorption estimate will be presented with the label "NULL". By far, the largest set of measurements comes from those associated with BKGD, thus most comparisons will be in reference to this set.

Shot Number	BKGD	NULL	Stark
z2219	✓	✓	✓(NULL)
z2220	✓	✓	
z2222	✓	✓	✓(BKGD)
z2268	✓	✓	✓(NULL)
z2270	✓		
z2298	✓	✓(a only)	
z2299	✓		✓(BKGD)
z2300	✓		✓(BKGD)
z2364	✓	✓	
z2365	✓		
z2366	✓		✓(BKGD)
z2367	✓	✓	✓(NULL)
z2482	✓		
z2483	✓		
z2484	✓		
z2552	✓		
z2588		✓	✓(NULL)

Table 5.3: This table indicates for which shots each of the major processing or analysis methods examined in thesis were used.

The He-like neon measurements presented somewhat of a problem, and with this in mind there were a fews ways to extract a value for this fractional population. To discuss these, we'll focus on what will be referred to as the "standard" method of areal density measurements as discussed in Section 4.4. That is, measuring the areal densities by fitting the spectrum using standard Voigt profiles and typically utilizing as many of the He-like line features as possible (except for He-α) in an attempt to constrain the measurement as much as possible. The most obvious method for calculating fractional populations using these measurements is by obtaining the total neon areal density from the pressure measurements and the Ideal Gas Law in order to determine the fractions. This method of finding the total neon density will be referred to as a "pressure total". In addition, recall the second method of obtaining a total areal density, namely by summing up the measured areal densities from each ion, which will be referred to as the "summed total". Using this total provides a

second set of values for the fractional populations, which has been generally found to be different. Of course, in the second method, the fractional populations add up to 1. The fractional populations of the first method generally do not, which leads to a third way to obtain a He-like fractional population, by using a closure relation. In this method, the H-like, Li-like, and Be-like factional populations are obtained by the standard measurements and using the pressure total to calculate the fractions just as in the first method. The He-like fractional population is then obtained by requiring that the fractions add up to 1, such that

$$f_{He} = 1 - f_H - f_{Li} - f_{Be}. \tag{5.1}$$

Additionally, two different types of lineshapes were investigated for use with the He-like neon series. In these tests, the idea was to use the higher members of the series and compare the results when using Voigt profiles versus Stark broadened line profiles. Tests were performed for each line feature individually, as well as for a combination of the upper series members (i.e. He-5 and higher). The results presented in this chapter use the measurement results from the combination of lines unless indicated. The results from these tests for direct comparison are labeled "Voigt" and "Stark". These tests were run on a small sample of five BKGD style transmissions and four NULL style transmissions. These are indicated as such in Table 5.3 under the heading 'Stark'.

Note that for any measurements with the labels BKGD or NULL alone, the standard method of areal density measurements was used (i.e. Voigt lineshapes, and typically as many of the He-like line features as possible, except for He-α).

5.2 Charge State Distribution

The most basic way to look at the results of fractional populations is in the form of charge state distribution (CSD) plots. Several sets of these plots will be shown for comparison amongst each other regarding the different combinations of processing and analysis methods discussed above. Visible trends and expectations will also be discussed.

Figure 5.1 shows a set of CSD plots arranged in the same manner as in Table 5.2. In plots where there are multiple traces, individual shot results are plotted with dashed lines, and the average of these results is plotted with a red solid line. The value of the average ionization for each plot is shown below the legend as $\langle Z \rangle$. The H-like neon fractions, being a key part of this investigation, are blown up in the upper corner of each plot to better show the spread in values for a given plot. This set of CSD plots show results from BKGD transmissions, and they use the closure relation method for obtaining the He-like fractional populations. To date, the most stable and seemingly reasonable results involving the standard method of measurements come from using the closure relation. This will be discussed more later using a different series of plots, but the other two methods for finding the fractional populations produce more scattered results.

The first thing to notice about these plots is that they are all very similar. This is an important result because it shows consistency in the resulting plasmas created in these experiments, while varying the experimental parameters (i.e. by nearly an order of magnitude in pressure and a factor of two in radiation flux). Most of the population is consistently in the He-like ion stage, with a smaller amount in the Li-like stage, and just a few percent each in the H- and Be-like stages. Now the variations between the plasmas should shed light on the physics relating to the plasma conditions and how the parameters affect it.

BKGD

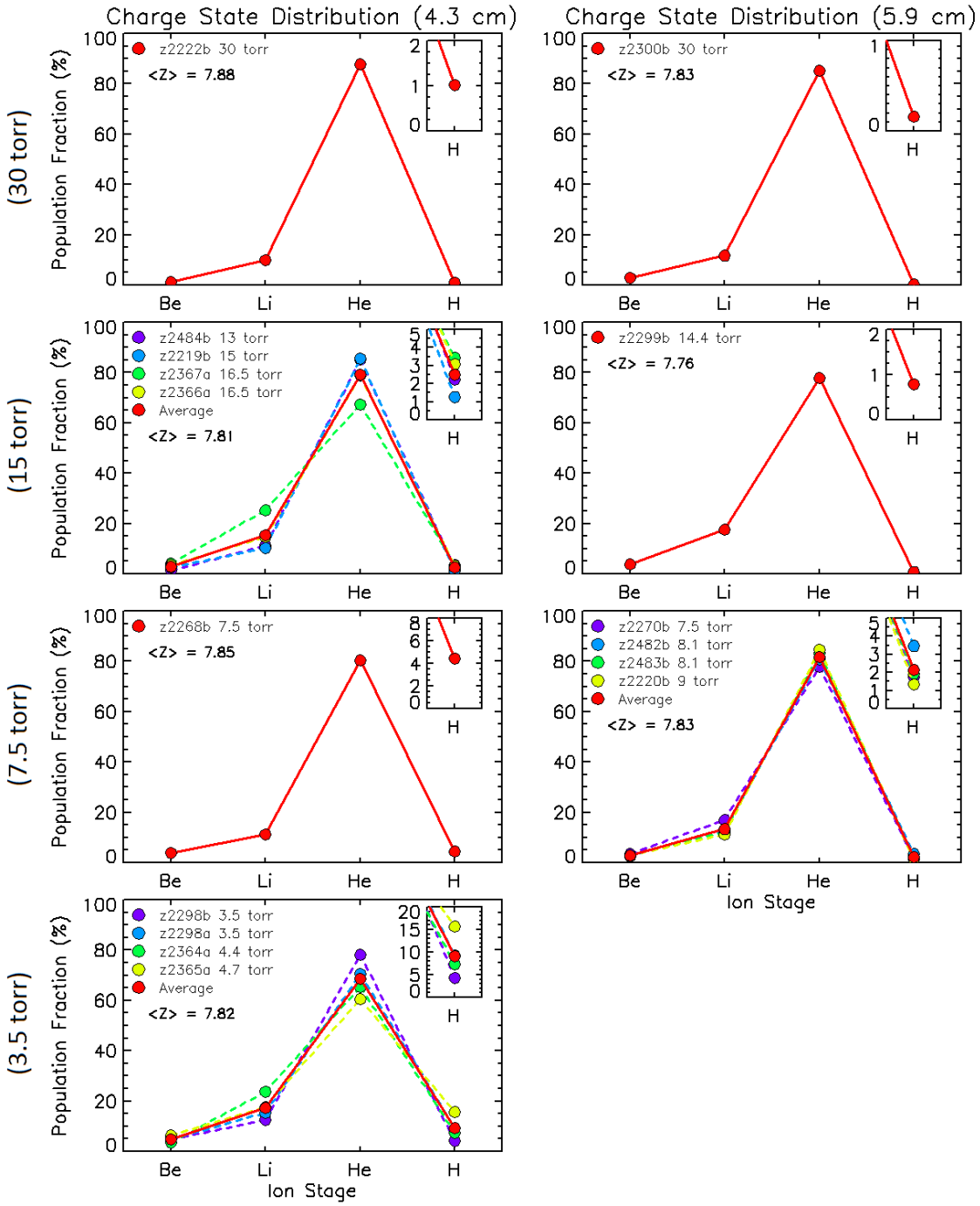

Figure 5.1: Charge state distributions using BKGD transmissions, pressure totals, and the closure relation to obtain the He-like population fraction.

Regarding trends and expectations for this set of plots, one would expect to see more ionization when moving down through the plots to lower filling pressures, and one would expect less ionization when moving to the right to the farther distance. Likely the best gage at this time for observing this is by looking at the values of the H-like population. Due to the fact that these quantities are still small (i.e. a few percent) and are at the upper end of the relevant range of ion stages, they will be more sensitive to changes in the amount of ionization. The Be-like and Li-like populations are not considered to be a good gage due to more uncertainty in their measurement values, and for the He-like population the same reason applies, along with the fact that it is the largest population through which the 'flow' of ion stage population is passing, making this ion stage less sensitive to changes in the level of ionization.

Focusing on the H-like populations, and particularly the averages in red, it is clear that there is an increase in the H-like fractions when going to lower filling pressures. It is also clear that these values decrease when moving to the farther distance. Recall the third way to look at varying these parameters, namely attempting to keep the ionization parameter approximately constant by, for example, moving the gas cell out while lowering the filling pressure. For now, let us approximate that by comparing plots diagonally, downward and to the right. Comparing the plot for 30 torr at 4.3 cm with 15 torr at 5.9 cm, the H-like populations are both in the vicinity of 1%, while comparing the plot at 15 torr at 4.3 cm with 7.5 torr at 5.9 cm, the H-like populations are both in the vicinity of 2%. The average values at least, are following the expected trends.

The average ionization $\langle Z \rangle$ is obviously another way to gage the amount of ionization and would generally be the best way to do so. However note that the uncertainties in each of the ion stage measurements will affect this quantity. The trends expected

for this quantity are the same as for the H-like populations, one would expect it to rise with lower filling pressures, and it should decrease toward the farther distance. In these results, there is indeed a decrease moving from the close distance to the far distance as expected, however the same cannot be said for the compliance in trends along the other axis. There is no clear trend in $\langle Z \rangle$ with regard to the pressures.

Regarding the other ion stages, the Be-like and Li-like populations both have a slight tendency to rise with lower filling pressures, which is exactly opposite of what would be expected for these ion species. This will be discussed in more detail later. The He-like populations stay around 80%, and in fact, purely due to the use of the closure relation and the rising trends of the other three ions with decreasing pressure, the He-like populations here have a slight downward trend with decreasing filling pressure.

Now moving on to Figure 5.2; the only thing that has changed is that these measurements come from transmissions which used the NULL background estimation method. The He-like populations are still obtained from the closure relation. This set of plots can be compared with those of Figure 5.1 to see how the different zero-level of absorption estimates affect the results. The expectation is that using the data from a null shot to estimate the background level will improve the measurements by accounting for crystal artifacts and other related effects. Overall, they produce very similar results, but there are a few notable differences. First of all, note that there is still consistency between the charge state distributions. Next, note that the trends in the H-like populations still align with what is expected. There is an increase with lower pressure and a decrease with further distance. Diagonally, the 7.5 torr at 5.9 cm falls somewhere in between the 15 torr and 30 torr cases at 4.3 cm, which since the ionization parameter has not yet been quantified, this is still along the lines of what is expected. Also note how tightly grouped the three traces in the 30 torr plot

NULL

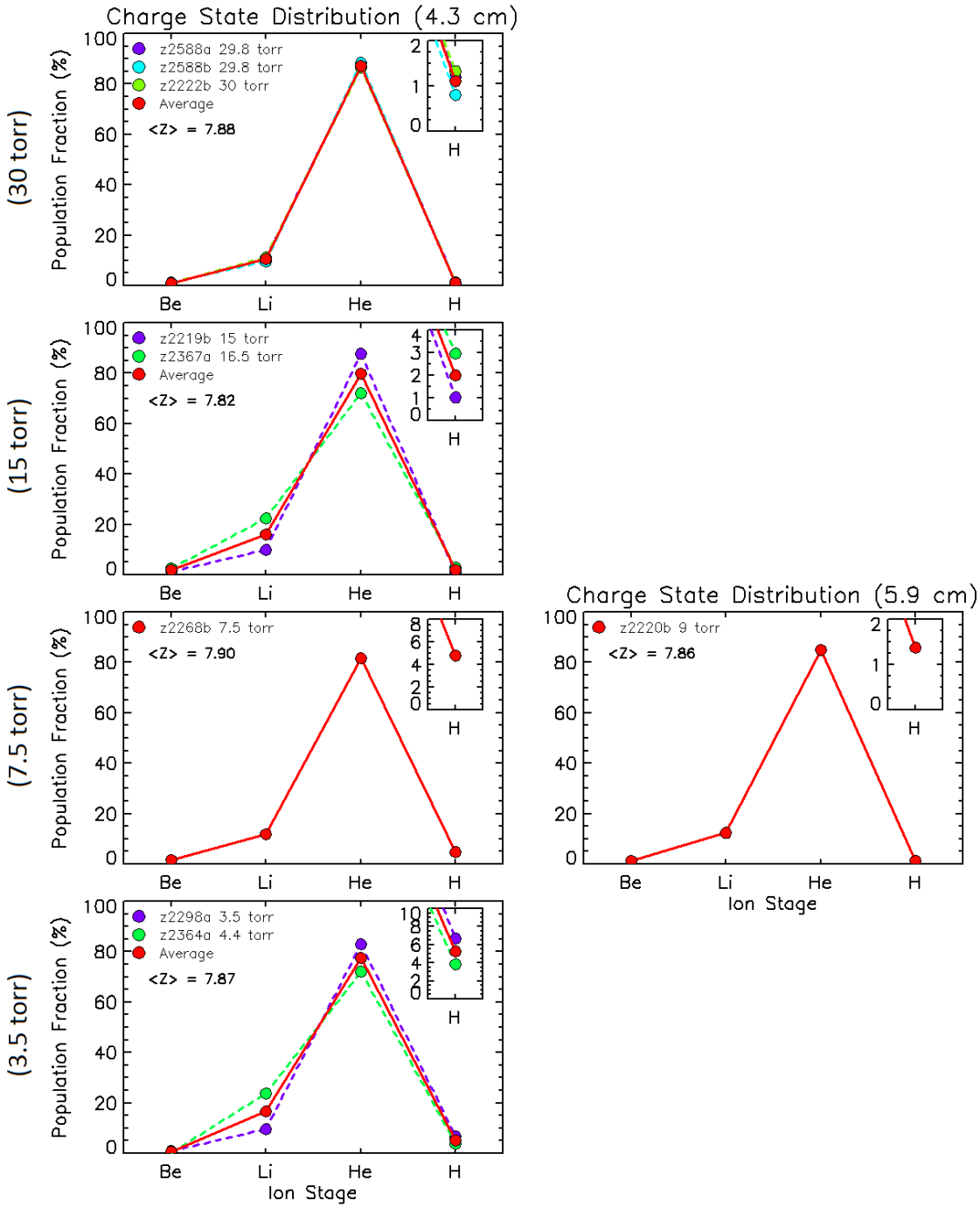

Figure 5.2: Charge state distributions using NULL transmissions, pressure totals, and the closure relation to obtain the He-like population fraction.

are, and that these are nearly the same as for the BKGD case. This is encouraging in the sense that for the highest pressure shots, the measurements seem fairly consistent regardless of this change.

The differences for these CSD plots are most easily seen in the Be-like populations, which drop considerably for the lower pressure shots, which is very encouraging. This will be discussed in more detail later with more detailed plots, but the reason for this drop is due to the fact that the null data helps to account for the contamination of the Be-1 line feature group by absorption from the Si_4N_3 windows. This is certainly a step in the right direction! The Li-like populations do not show any notable change here, and the He-like populations respond to the decreased Be-like populations by being a little more stable around 80%.

Moving on to Figure 5.3, this set of plots show how the shape of the CSD can change when using the summed total to obtain the population fractions. The results in this set use transmissions from BKGD, so this set of plots can be compared with Figure 5.1. To be clear, the same areal densities from earlier are used here, and the only differences are that the He-like fraction actually comes from the measured areal density for that ion and the total for the fractions is now the summed total instead of the pressure total. The plots still show consistency while varying the experimental parameters. The H-like populations show the same overall trends as discussed earlier, with the 15 torr at 4.3 cm case being somewhat of an outlier. Observations regarding other trends are also about the same as before.

The major noticeable point of difference is in the relative values of the fractions. These differences stem directly from the measurement of the He-like population, which shows the importance of getting this measurement correct. Due to the fact that this charge state is where much of the ion population tends to be, it has a large effect on the fractions of the others. Of course, in some cases the Li-like total population has a

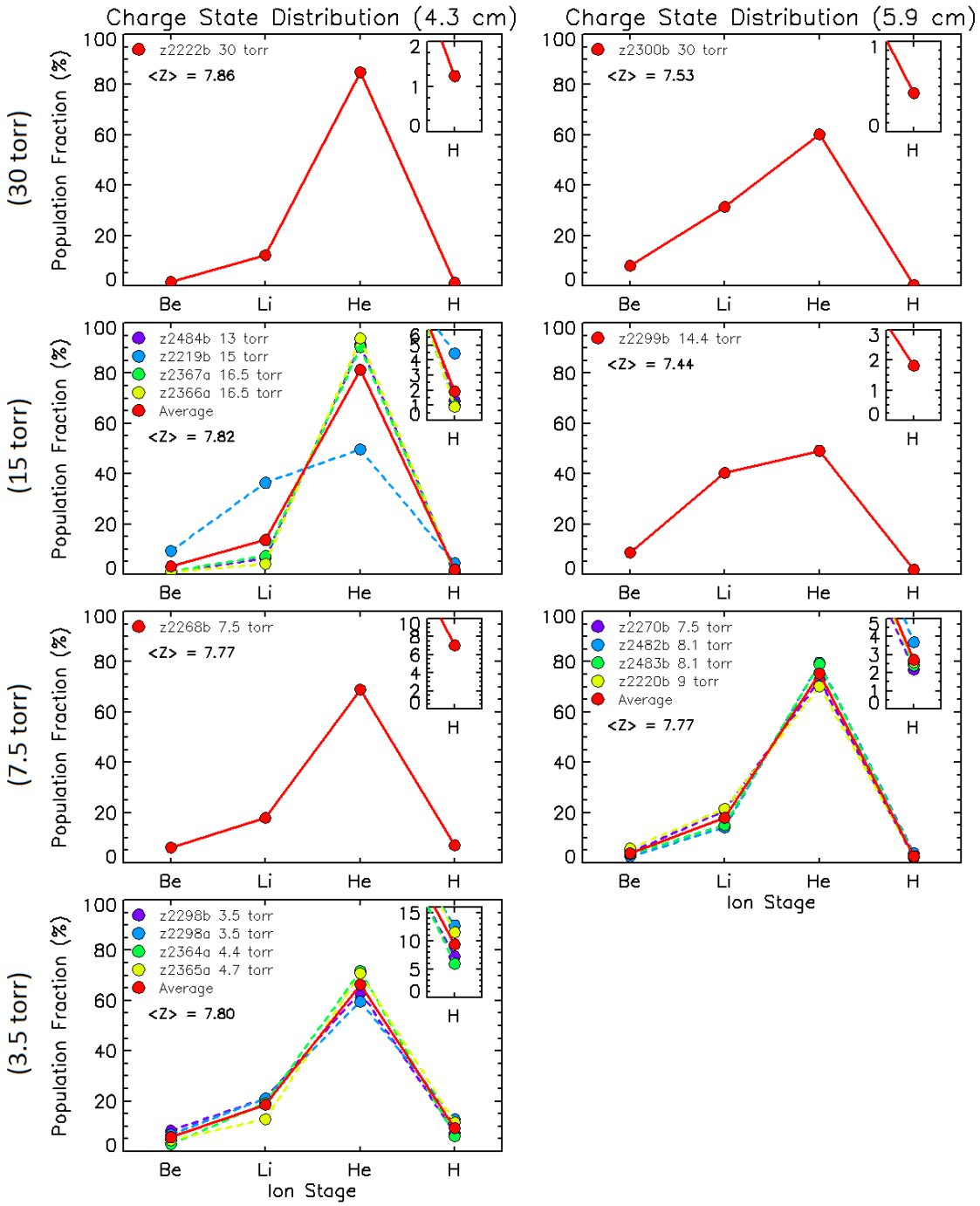

Figure 5.3: Charge state distributions using BKGD transmissions, the measured He-like areal densities, and the summed total for population fractions.

similar level of effect. In this method, generally the He-like population measurement results in a smaller fraction, while the other three fractions tend to be increased relative to when using the pressure total and the closure relation to find the population fractions. This is due to the tendency of the sum of these measurements to come out low relative to the pressure total, but this is not always the case; some come out much higher. This will be further discussed later on. It will also be shown that the spread of values measured in this way is larger than when using the closure relation, at which time the third method of calculating He-like ion fractions will also be discussed.

5.2.1 Summary: CSD

To summarize what was found in this section, the most important result is that the experiments are consistently creating very similar, highly ionized plasmas with around 80% of the ion population in the He-like ion stage and a small fraction in the H-like ion stage.

Another important result is that clear trends in the H-like neon populations are consistently seen following what would be expected in terms of changes to the amount of ionization in the plasma in relation to changes in the experimental parameters. This includes the trends of higher ionization with lower pressures, lower ionization with lower radiation flux (i.e. further distance), and similar levels of ionization when changing both parameters simultaneously.

The average ionization values $\langle Z \rangle$ are somewhat scattered, but they do show the expected trends along the distance axis. No clear trend emerges for this quantity along the pressure axis.

Some issues become apparent regarding the trends in the Li-like and Be-like ion populations. However, the NULL background estimation presents a very encouraging move in the right direction for the Be-like ion populations.

The He-like populations are shown to have substantial effect on understanding the distribution of ion species populations in the plasmas, and that there are discrepancies between the distributions produced by using the two available methods for finding the total neon density.

5.3 Fractional Populations vs Ionization Parameter

To better understand trends that emerge from the measurement results, each ion species can be plotted separately from one another. There are multiple ways of doing this. One way to do it is similar to how the CSD plots were arranged. The CSD plots were arranged according to pressure with two columns for the distances. Similarly, each ion's fractional population can be plotted against the total neon number density, and there would be a separate trace for each distance. An example of this is shown in Figure 5.4 for the H-like neon population fractions with points from the close position in red and the far position in blue. The measurements shown here use BKGD transmissions, and the pressure total is used to find both the fractional population values and the total neon number densities for the abscissa values. Thus, these are the same measurements as in Figure 5.1. This is the set that will be used for the following several results. Hyperbolic curves (chosen because $\xi \propto 1/N$) have been fitted solely to guide the eye. The trends that were observed before in the H-like populations are more clearly visible. The fraction of H-like neon, and thus the level of ionization increases with lower filling pressures. The fractions also decrease when decreasing the radiation flux by moving outward.

Another way of displaying these results is to plot the fractions against the ionization parameter ξ. Since this would take into account both the density and irradiance

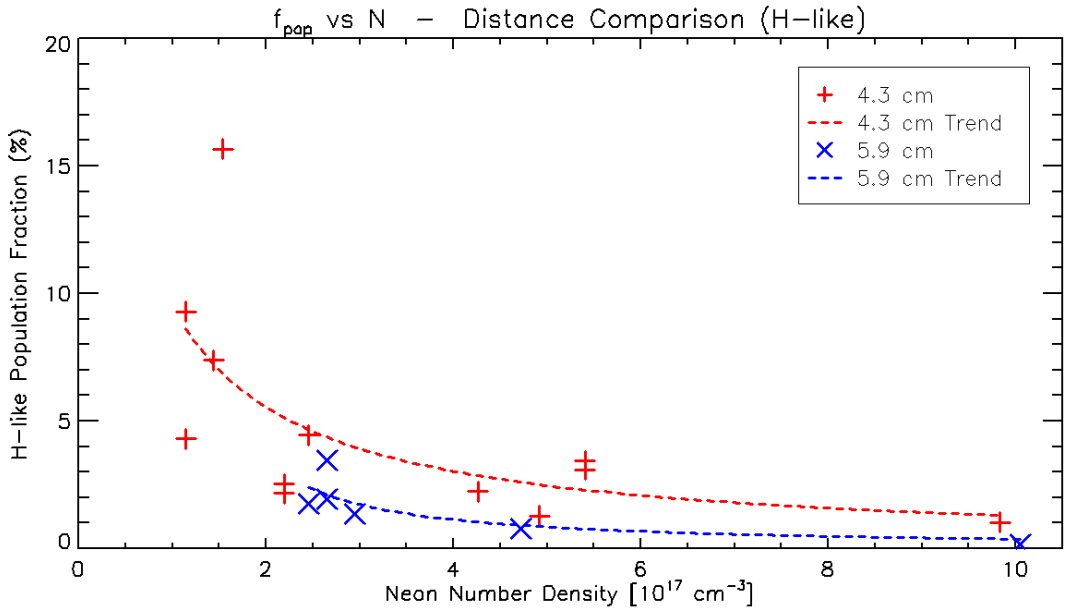

Figure 5.4: Fractional population of H-like neon plotted against total neon number density. Red points are from the close distance, and blue points are from the further distance. Hyperbolic curves are fitted to guide the eye.

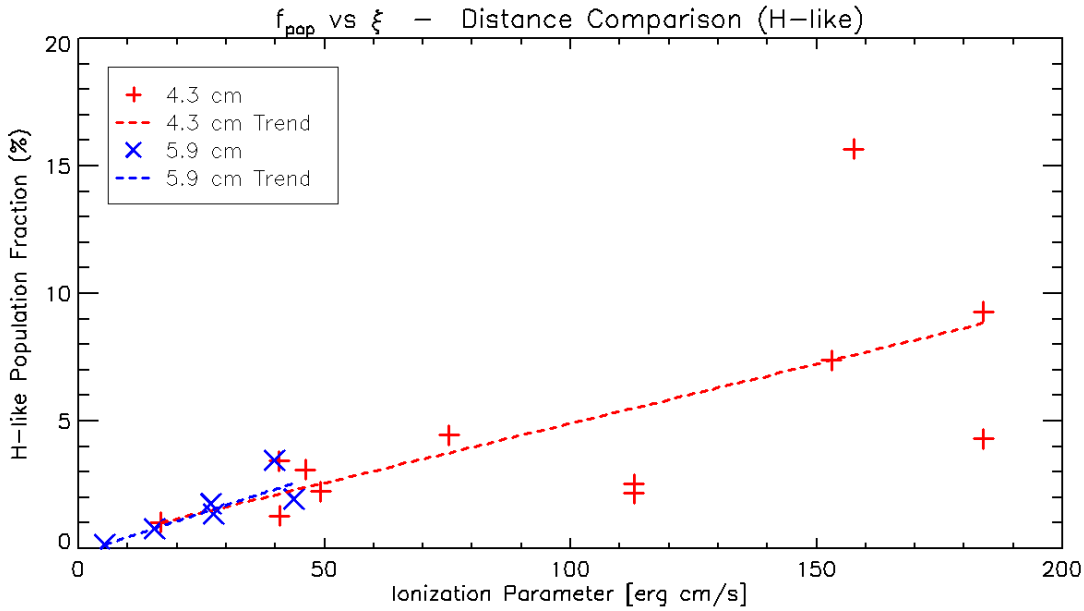

Figure 5.5: Fractional population of H-like neon plotted against the ionization parameter value. Red points are from the close distance, and blue points are from the further distance. Lines are fitted to guide the eye.

simultaneously it would seem to put all the measurements from both distances on a similar footing. Figure 5.5 shows the same measurements the previous plot, plotted against the ionization parameter values, which were listed in Table 5.1. It is clear that the data points from experiments at the further distance end up at the lower end of the ξ range due to the lower irradiance values experienced at this distance, and all of the higher ξ values come from the closer position. The upward trend shown for this ion in this manner seem much closer to being linear in nature, at least for the limited range visible. The lines fitted here show that there is a good overlap of the trends for both distances, at least in the region where data for each is available. This second point gives support to the idea that these data points may be on similar footing with use of this parameter, and that this parameter seems to be a good quantity with which to reference the overall behavior of the plasmas in this experiment.

In continuing, ξ will be the parameter of choice to continue observations. The good overlap seen for the H-like species is also observed in the other three ions. In the future, when pushing the limits of the experiments further, there may be a difference that begins to emerge, but at this time, in this regime, ξ is a good reference quantity. Take note, however, that the amount of ionization caused by the radiation field will also depend on the energy content of the radiation spectrum, that is, it will depend on the color temperature T_C of the radiation field; whereas the way ξ is calculated now really only considers the brightness temperature T_B.

During the course of this experimental campaign, attempts have been made to push toward lower filling pressures, and hence lower neon number densities. These lower neon filling pressures are difficult to achieve with the equipment that is available. With the measurement technique developed by Ref. [37] many of the lowest intended pressures attempted were revised upward, reducing many of the effective ionization parameter values in these experiments. Figure 5.6 shows the affect this had on the

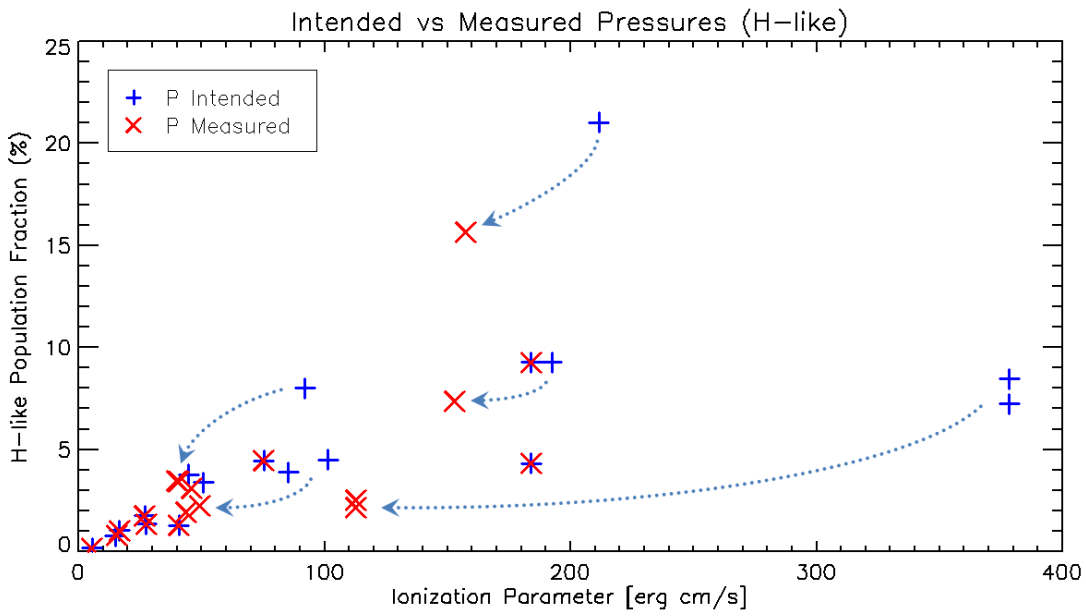

Figure 5.6: Plot showing the affect on the placement of points within the f_{pop} vs ξ space from better measurements in the neon filling pressure. Many of the lowest pressure measurements were revised upward, shifting the points downward and to the left.

placement of many of the points within the fractional population versus ionization parameter space. Arrows indicate the movement of the points due to the upward revisions. Many, but not all, of the points that overlap for both series were from before the new measurement technique was put in place. For example, this is the case for the points at $\xi \approx 185$ and 75 erg·cm/sec, but for higher pressures the measured pressure tended to agreed well with the intended pressure. The message from this observation is that some of the measurements in this dataset, particularly the ones with no pressure measurement, may be wrong due to the uncertainty of the intended pressure. All of the pressures used in the results are the measured pressures, unless explicitly indicated.

The two points paired at $\xi \approx 480$ erg·cm/sec and at $\xi \approx 110$ erg·cm/sec contain anomalies, but are shown for completeness. This shot (z2552) was the first attempt at a filling pressure of 2 torr. The spectral features in the data for this shot were

very weak, indicating that a low pressure may have been reached, and H-like and He-like line features were identified. There was quite a lot of noise and uncertainty about whether any Li-like and Be-like features could be seen; therefore, there are no measurements for those ions. The low signal to noise ratio is likely to have presented a problem for the measurements of the H-like and He-like areal densities as well. The amount of revision to the pressure was also somewhat surprising. Either way, the measurements for this shot are anomalous, but will be included in many of the plots in this chapter for completeness.

5.3.1 Total Densities: Pressure Total versus Summed Total

Another detail that has presented some concern is in the disagreement of the totals obtained from the measured pressures versus the summation of the measured ion densities. The most influential measurement relating to this is that of the He-like ion densities. Recall the three methods of calculating population fractions using the ion densities. The first was to use the pressure total with the measured He-like density to obtain the fractions. This allows for the possibility of the fraction to exceed 100%. The results calculated in this manner are shown in Figures 5.7 and 5.8 as the blue + symbols. The second method used the summed total with the measured He-like density to obtain the fractions, which means the fractions cannot exceed 100%. These are shown as the red $\times$ symbols. Finally, the third method was to use the fractions from the pressure total of the other three ions, and to obtain the He-like fraction from the closure relation. For these experiments, the sum of the H-, Li-, and Be-like densities has had a maximum of near 40%, which means that obtaining the He-like fraction from the closure relation remains between 60% and 100%. These are shown in the figures as green squares.

Regarding the blue points, from the first method, there are three points for which

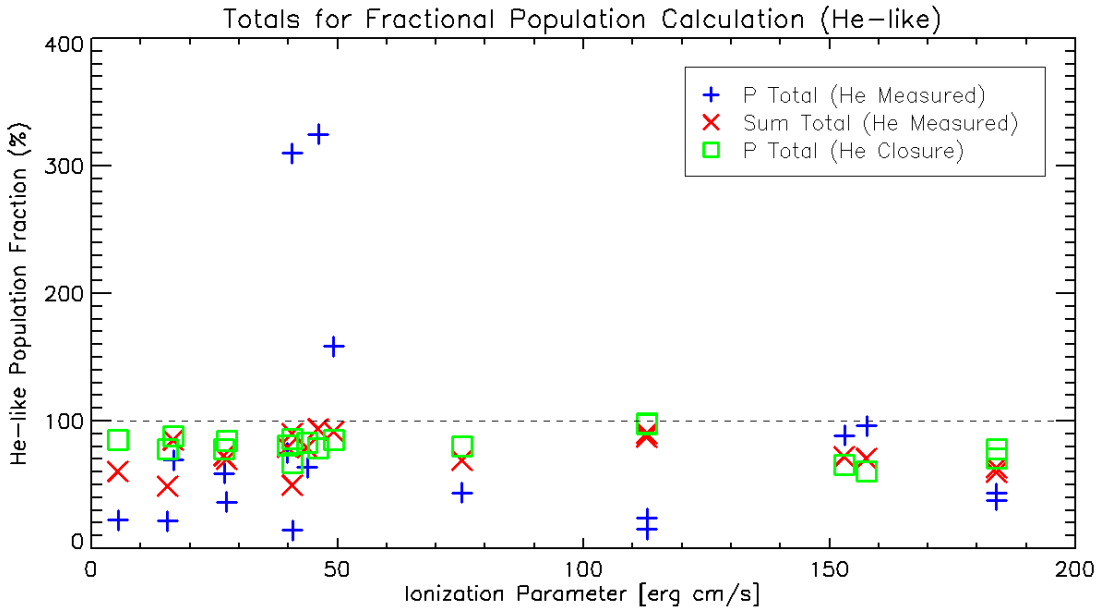

Figure 5.7: He-like fractional populations plotted for the three methods for calculating the fraction values. Blue points represent the fractions resulting when using the measured ion density with the pressure total. Red points represent when using the summed total. Green points are the results of using the closure relation method. The 100% value is indicated by the horizontal dashed line.

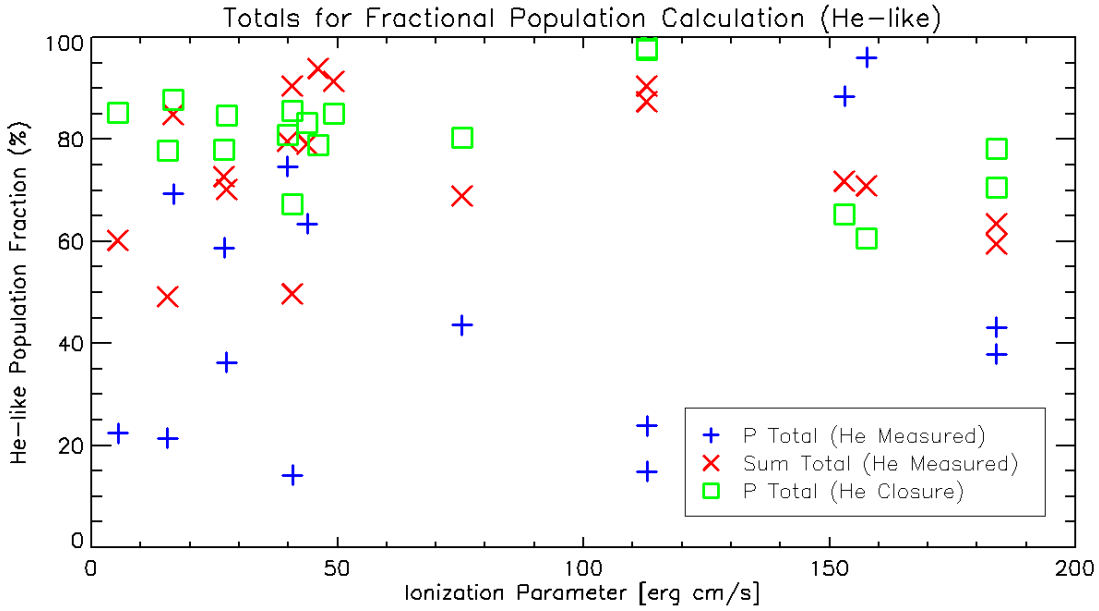

Figure 5.8: Same data as Figure 5.7, but limited to the range of 0-100%.

the He-like fractional populations exceed 100%. There were more than this before the revisions were made to the filling pressures, which is encouraging in regard to those pressure measurements. All three of these points come from after the better pressure measurements began, two of them came from the same shot series, and the third point comes from the following shot series. The data from these two shot series in particular had some subtle differences with respect to the data from other shot series, and the He-like fractions by this method for the other shots of these two series were also among the higher values. This hints to a possibility that this might relate to some overlooked experimental factors during those two shots series. As for the other blue points, they are clearly extremely scattered and unreasonable.

Looking now at the red points, these are far less scattered and slightly more reasonable, but they are still have a considerable amount of scatter, ranging in value from 50% to 95%. The green boxes, however, show much less scatter and begin to show a slight downward trend (excluding the anomalous shot z2552). Note also that the low point at $\xi \approx 40$ erg·cm/sec is one of three shots exceeding 100% in the first method.

For the other ion populations fractions, obviously only the first two methods are relevant, using either the pressure total or the summed total to calculate them. A comparison of results from these methods for the H-like measurements is shown in Figure 5.9. The blue points use the pressure total and the red points use the summed total, just as in the previous plots. There is not a large difference between the two traces for this ion, but some things should be noticed. First of all, much of the red trace is rather tightly packed in a line slightly above the blue points, except for the little bubble of four low points between $\xi \approx 40$ and 50 erg·cm/sec. The three lowest of these are from the shots that exceed 100% using the first method, and the one above them is from the second of the two odd shot series. It is also interesting to note

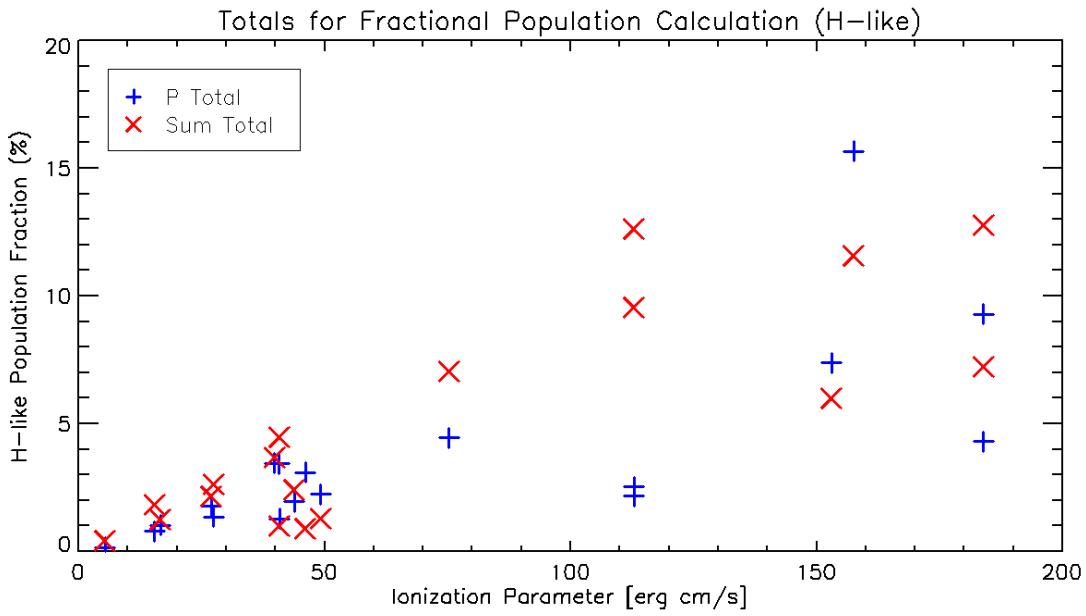

Figure 5.9: H-like fractional populations plotted for the two methods for calculating the fraction values. Blue points represent the fractions resulting when using the measured ion density with the pressure total. Red points represent when using the summed total.

that the two points from shot z2552 near $\xi \approx 110$ erg·cm/sec move up to be more in line with the rest when using the summed total.

As for the Li-like and Be-like fractional populations, shown in Figures 5.10 and 5.11 respectively, the major effects are a reduction in the spread of the results as well as a reduction in the fraction values themselves for the most part, when using the pressure total. Note that all three of the low red points that fall below everything in both of these plots are from the same three shots in which the He-like fractions exceeded 100%.

Now that it has been shown how each ion species measurement affects the summed total and the ion fractional populations of the other ions, it is appropriate to begin directly comparing the total neon densities computed using the pressures versus the total neon densities computed from the sum of ion density measurements. This is shown in Figure 5.12. There are four plots shown that can be compared amongst

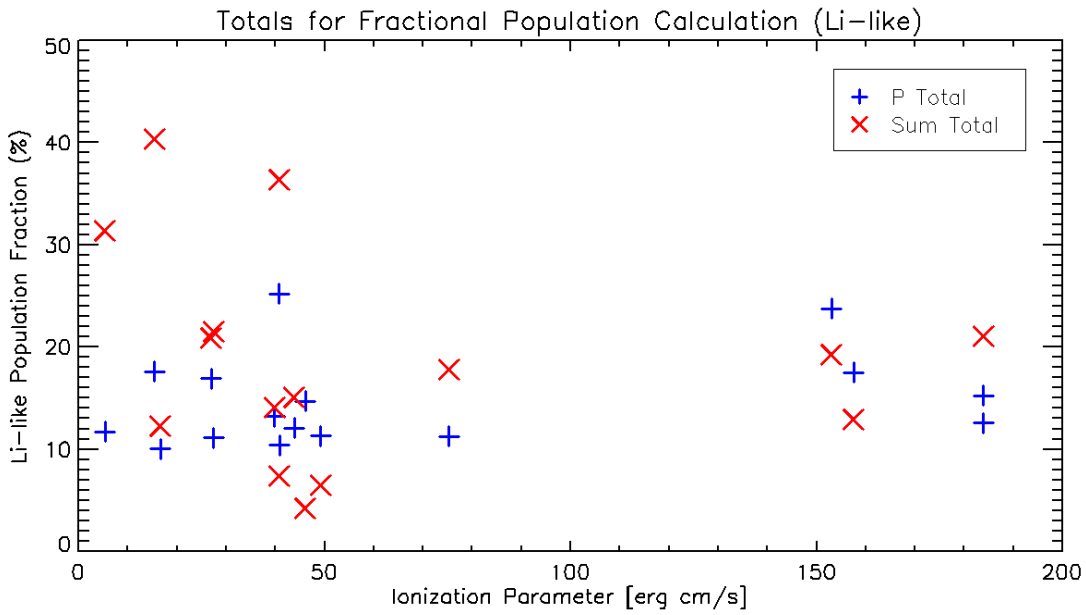

Figure 5.10: Li-like fractional populations plotted for the two methods for calculating the fraction values. Blue points represent the fractions resulting when using the measured ion density with the pressure total. Red points represent when using the summed total.

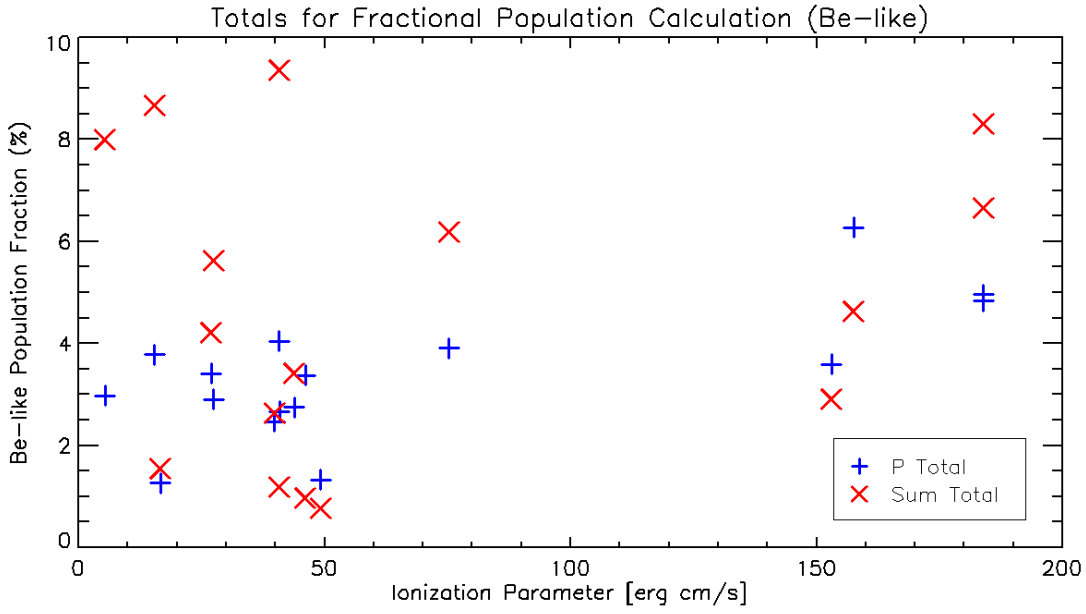

Figure 5.11: Be-like fractional populations plotted for the two methods for calculating the fraction values. Blue points represent the fractions resulting when using the measured ion density with the pressure total. Red points represent when using the summed total.

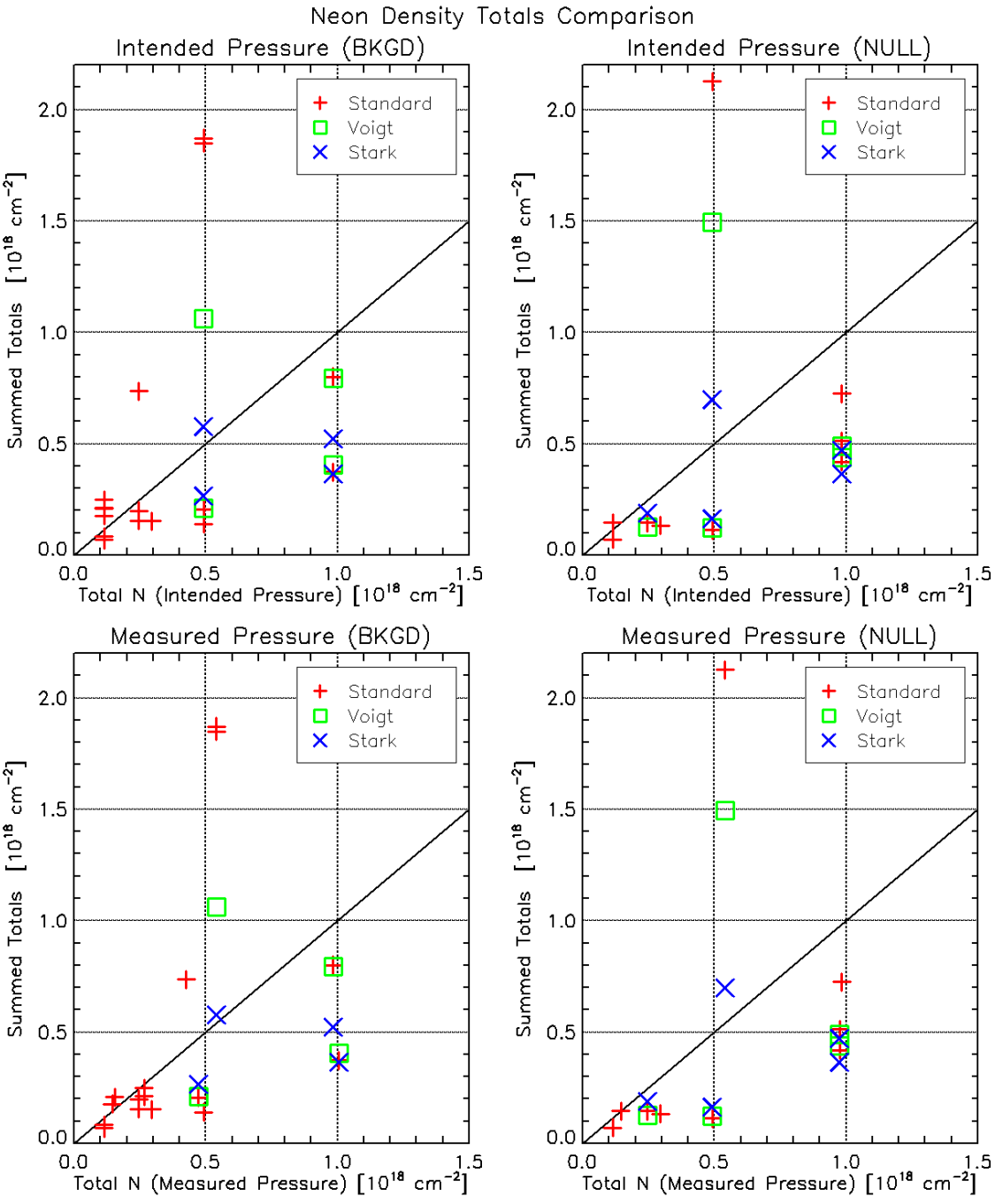

Figure 5.12: Comparison of summed totals (vertical axis) and pressure totals (horizontal axis) from the *Standard* method (red) and from the results of the Stark lineshapes tests (i.e. *Voigt* in green and *Stark* in blue). The line of equality is plotted diagonally. The upper row uses the intended pressures, and the lower row uses measured pressures. The left column is from BKGD transmissions, and the right column is from NULL transmissions.

one another. On the horizontal axis is the total neon density calculated from the filling pressure. In the two upper plots, this filling pressure is the intended filling pressure. In the two lower plots, the measured pressure is used. Along the vertical axis of each plot are the summed totals of ion measurements. The line of equality is plotted diagonally. There are three types of points, labeled *Standard*, *Voigt*, and *Stark*. These refer to three different methods of measuring the He-like ion density (not fractional population). *Voigt* and *Stark* have not been discussed fully yet, so ignore these for now, we will return to these later. *Standard* refers to the standard method of measurement, which we have been discussing up to this point. The values for the densities of H-like, Li-like, and Be-like ions are all identical across the three types of He-like ion density measurement methods. Therefore, the only difference between the three types of points in a given plot is the result of the He-like ion density. Finally, the two columns of plots differ in that the left column includes measurements from BKGD transmissions, while the right column is from NULL transmissions. The BKGD and NULL results comparison is also to be discussed later, in the following section.

Concentrating on the left column (BKGD) and only on the red points, comparing the upper and lower plot and recalling that many of the lower pressures were revised upward, it is apparent that many of the points have moved to the right (i.e. to higher pressure totals) in the lower plot. This is also apparent in the NULL column. The summed totals are not affected by the pressure measurement. For many points, but not all, their horizontal movement with the measured pressures brought them closer to the line of equality. Focusing now on the lower BKGD plot, the three points highest above the line of equality, are the three points from earlier where the He-like measurement alone exceeded 100%. However, there are other points for which the summed total still exceeds 100%, but not by quite as much. Most of the summed totals are less than the pressure totals, some of them very much less, as much as

being only 28% of the pressure total. For the lowest of these, this is a point which needs to be addressed and understood. For the ones that are relatively near the line of equality, there may be an explanation.

While one would expect that as measurements improved the summed total would move toward matching the pressure totals, there is a scenario in which it might be expected that the summed totals would be consistently less than the pressure totals. Recall that the Si_4N_3 windows in these experiments are only 5×5 mm in size, whereas the gas cell dimensions perpendicular to the LOS are 2×2.34 cm. The radiation is blocked from entering the gas cell outside the 5×5 mm area of the front window, leaving a substantial volume of neon gas not being directly heated by the radiation. As the column of neon gas in the volume directly exposed to the radiation is heated, the pressure will also rise (recall the Ideal Gas Law $P = nkT$, holding n approximately constant). This will create a substantial pressure gradient between this heated volume of gas and the cooler gas surrounding it. This will lead to an expansion of the heated gas into the rest of the volume of the gas cell. If this begins to happen before the peak of the radiation drive, the conditions of the plasma as recorded by the TREX might have a lower neon number density. But it is also possible that the time scale with which this occurs is longer than what will show up in the absorption spectra. At this point, this is just speculation, and hydrodynamic simulations will have to be run in order to get a better understanding of what effect, if any, this might have on the plasmas in these experiments and the measurements from them.

A second possibility for low summed totals relative to the pressure totals is that the second order reflection photon correction has not yet been implemented into the data processing procedure. Once this is included, it might have the effect of raising some of the areal density measurements. It is a photon energy dependent correction, so it may affect each ion species differently. The correction will be larger toward

the lower photon energies, so it may affect the Be-like measurements the most, but overall, it is thought that the changes to the measurements should be small.

Either way, with the tendency of the summed totals being low and the He-like ion fraction being the major culprit, the other three ions were seen to be elevated with respect to the pressure total method. This is what was observed in Figures 5.9, 5.10, and 5.11. For each one the summed total fractions were generally above those using the pressure total, while in Figure 5.8, many of the He-like summed total results were below those of the closure relation. In the end, once the measurements improve (i.e. mainly the He-like measurements), one might expect that the summed totals would begin to converge toward the pressure totals, and one would hope that this would also reduce the spread seen in all of the ion population fractions when using the summed totals, though of course there may be something else being missed, which should be kept in mind. One possible solution is to use Stark broadened line profiles, which may help to move it in this direction. This will be discussed in Section 5.5. Before that differences from the two methods of zero-level of absorption estimation will be discussed.

5.4 BKGD vs NULL Zero-Level of Absorption Estimate

As discussed in Section 3.2.3, there are two methods for estimating the zero-level of absorption for converting the spectral data into transmission spectra, referred to in this chapter as BKGD and NULL. What would be expected here is that the NULL method should produce more reliable transmission spectra mainly because it will better take into account crystal artifacts in areas where important line features exist.

Beginning with the H-like fractional populations, Figures 5.13 and 5.14 com-

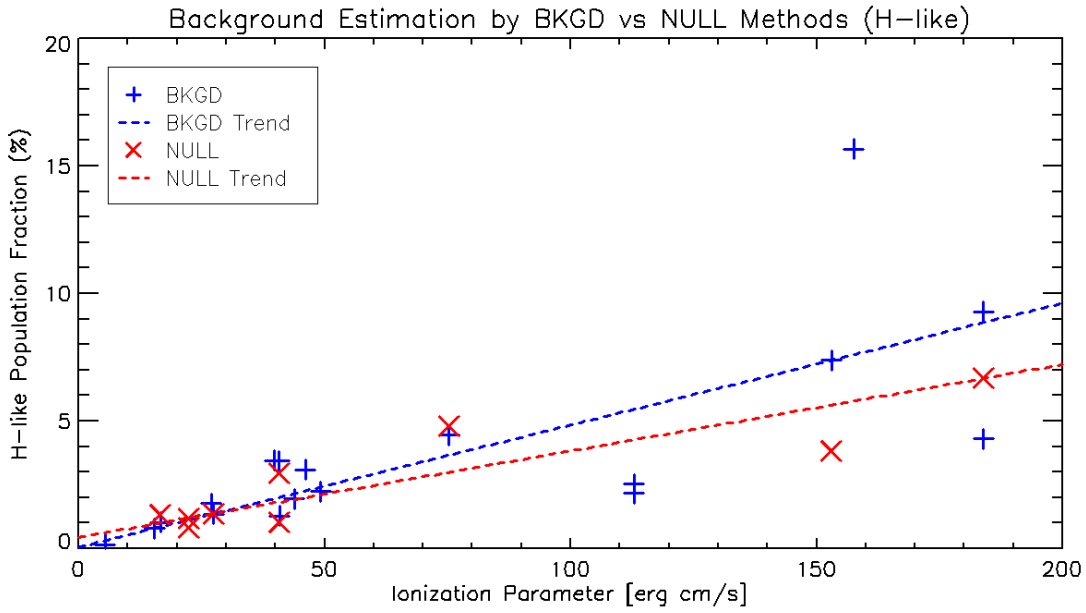

Figure 5.13: H-like fractional populations comparing results from BKGD transmissions and NULL transmission. Lines are fitted to the whole range of points to guide the eyes.

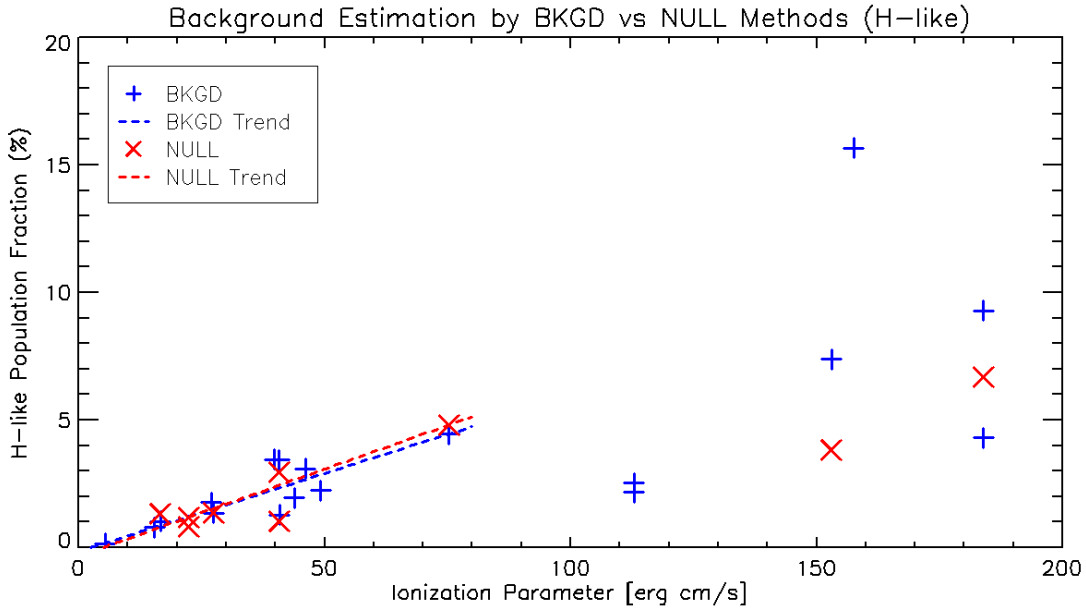

Figure 5.14: Same data as Figure 5.13, but the lines are now fitted only to the lower end of the range where measurements seem more reliable.

pare the results of measurements derived from transmissions produced by the BKGD method and those produced by the NULL method. Here the fractions are calculated using the pressure total, since it seems to produce overall more consistent results. In each figure, trend lines have been fitted using a "robust" least absolute deviation (LAD) method [58] as opposed to the more common least squares minimization method [59]. This method is used because the result is less affected by the presence of outliers in the data. In Figure 5.13 each series has been fitted in its entirety. The trends of both series are very close, varying only slightly in slope. However, the measurements from shots involving the lowest pressures (i.e. higher values of ξ) come from spectra with a smaller absorption signal, and hence larger errors might be expected for these. There are also fewer points at the upper end of the ξ range, so focusing in on the more populous, and more trusted, area of the plot below $\xi \approx 80$ erg·cm/sec, the fitted lines in Figure 5.14 overlap much more closely. Aside from this, the measurement values in this region are only slightly affected by the use of the NULL method rather than the BKGD method. This, along with the other areas of consistency seen in this ion's results, points to the idea that the fractional population measurements for this ion species are rather robust.

Moving on to the He-like fractional populations, Figures 5.15 and 5.16 also show little difference between the results from BKGD and NULL transmissions. Of course, these are results from the closure relation method of obtaining the He-like population fractions, so they are completely dependent upon the results of the other three ions. Both the fits from the entire range and the partial range show a consistent, slightly downward trend in which the NULL transmission results are slightly higher than those of the BKGD transmissions. Recall that the outlier near $\xi \approx 40$ erg·cm/sec is one of the three shots that produced large He-like measurements.

The most significant effects of using the NULL method are seen in the Li-like and

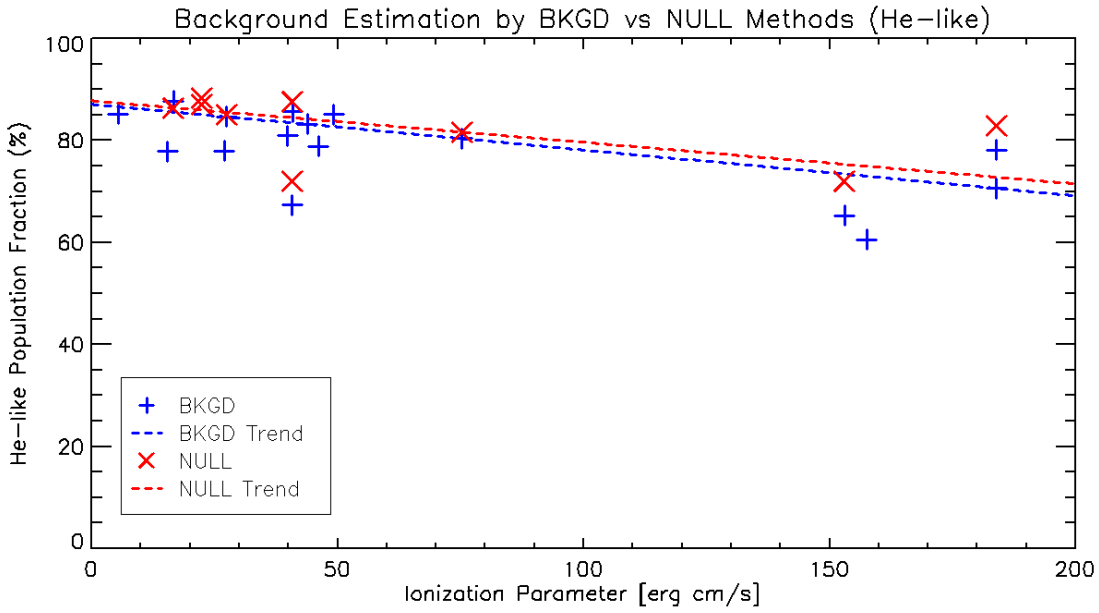

Figure 5.15: He-like fractional populations comparing results from BKGD transmissions and NULL transmission. Lines are fitted to the whole range of points to guide the eyes.

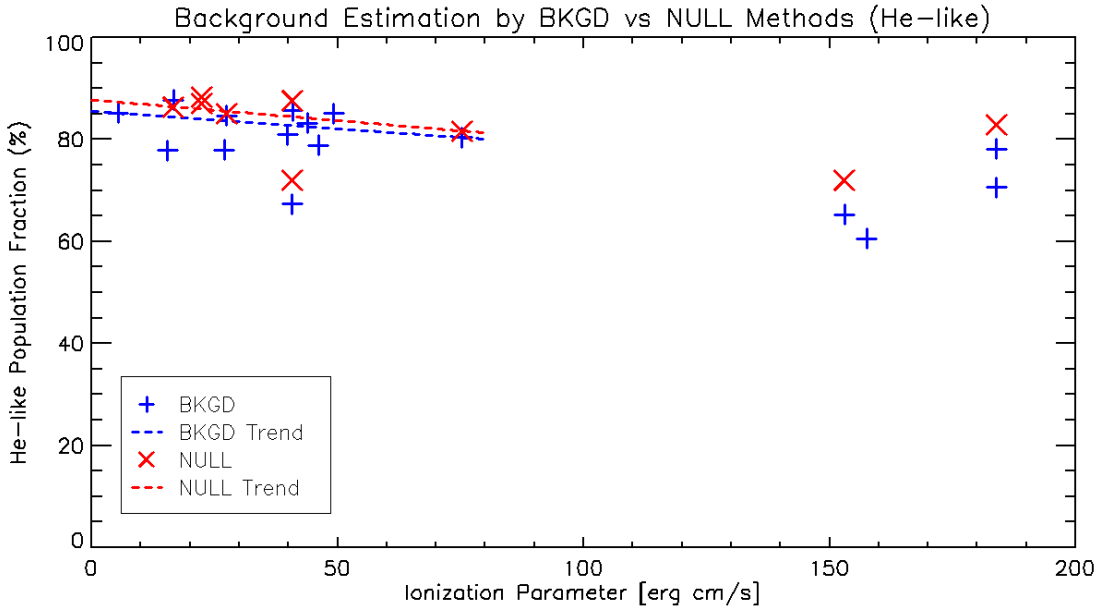

Figure 5.16: Same data as Figure 5.15, but the lines are now fitted only to the lower end of the range as was done in Figure 5.14.

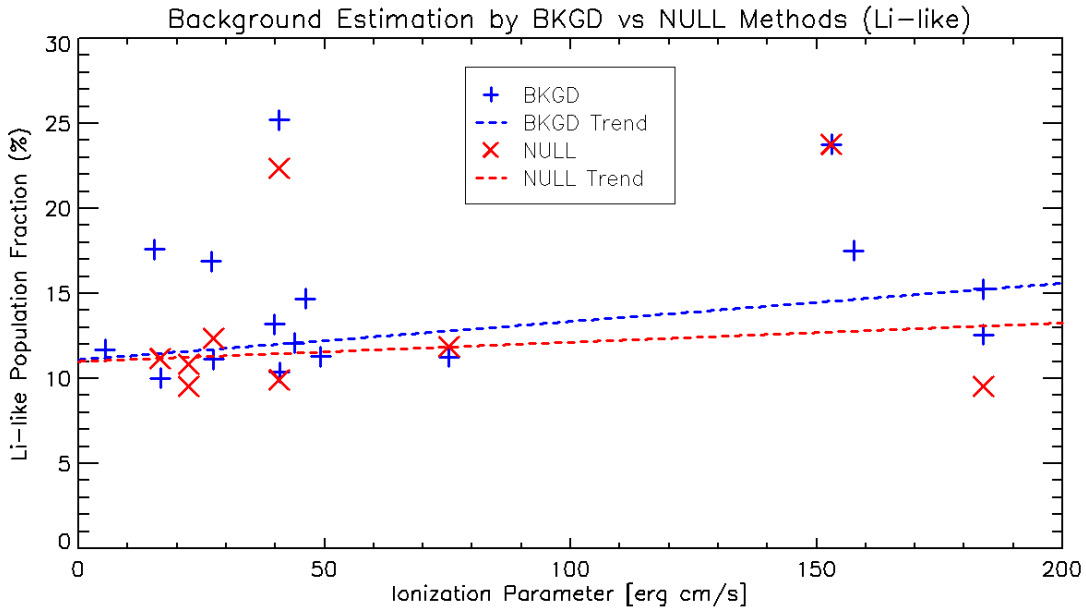

Figure 5.17: Li-like fractional populations comparing results from BKGD transmissions and NULL transmission. Lines are fitted to the whole range of points to guide the eyes.

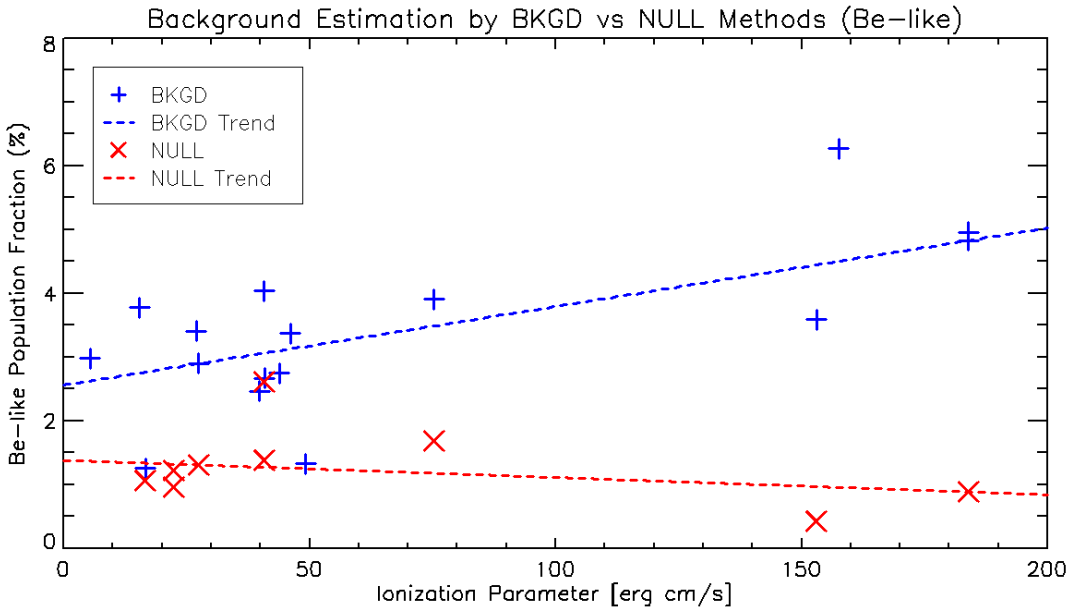

Figure 5.18: Be-like fractional populations comparing results from BKGD transmissions and NULL transmission. Lines are fitted to the whole range of points to guide the eyes.

Be-like fractional populations, shown in Figure 5.17 and 5.18 respectively. In both ions a clear tendency toward small population fractions is observed. This explains the slight rise in the values observed in the He-like populations using the closure relation.

Concentrating now on the Li-like population fractions, along with the reduction in the overall values produced, there is also a clear reduction in the spread of values. This is a further reduction of the spread that was seen before with the use of the pressure totals rather than the summed totals. The trend also goes from being ever so slightly upward to a little more flat, and possibly a tiny bit downward if ignoring the two severely outlying points, both of which come from the first of the two suspect shot series, and the one near $\xi \approx 40$ erg·cm/sec is the same shot as the one in the He-like plots. The other outlier also corresponds the low point in the He-like populations near $\xi \approx 150$ erg·cm/sec, which indicates that, if there were more data points using NULL transmissions, the He-like populations trend might actually flatten out more. Also, keep in mind, that these total Li-like fractional populations say nothing about what happens to the ratio of the two Li-like populations that are used to extract temperatures.

The Be-like populations are affected the most from the use of the NULL zero-level of absorption estimation method. The reason for this is that the null data used for this method will also contain the Si absorption due to the windows that directly overlaps the Be-like line feature used in the measurement, and therefore it will help to account for that extra absorption and remove it. This is a significant improvement. As well as the reduction in values, the upper ward trend seen for the BKGD transmissions turns downward for the NULL transmissions, closer to what is expected for this ion, though one should take note of the upward trend visible in the points just below $\xi \approx 80$ erg·cm/sec. The outlier near $\xi \approx 40$ erg·cm/sec is the same shot as the outliers in the other plots.

At this point, these plots double as showing what are currently considered the best results so far for each of the individual ion fractional populations. For the Li-like and Be-like populations, this is only true for the NULL transmission results, while for the H-like populations, the two methods were very consistent with each other. Regarding the He-like populations, while both the methods are fairly consistent, these are not direct measurements as should be expected to be possible with improved measurement methods for this ion that may include more physics that are not accounted for now, one example of which is the use of Stark broadened profiles. Note also that the NULL transmission results using summed totals still have the spread that was seen with the BKGD transmissions. The spread was slightly reduced in the Be-like fractions, which is promising, but the measurements reported here are still considered to be better.

But, for completeness, let us look now at how the summed totals are affected by the use of one or the other zero-level of absorption estimate. Refer back to Figure 5.12, and compare the red (Standard) points in each column. There are less points from the NULL transmissions, but one can see that they are distributed about the same throughout the plot.

5.4.1 Temperature versus Ionization Parameter

The above results are encouraging regarding the total ion fractional populations for Li-like and Be-like neon, but they say nothing about how the extracted temperatures are affected. Recall from Section 4.5 the method of temperature extraction from the populations of these two ion species, and also that there is a runaway uncertainty effect for higher temperatures relative to the value of the energy separation between the levels being used for the extraction. Keep in mind also that the temperatures being referred to here are the electron temperatures.

The extracted temperatures from BKGD transmissions and NULL transmissions

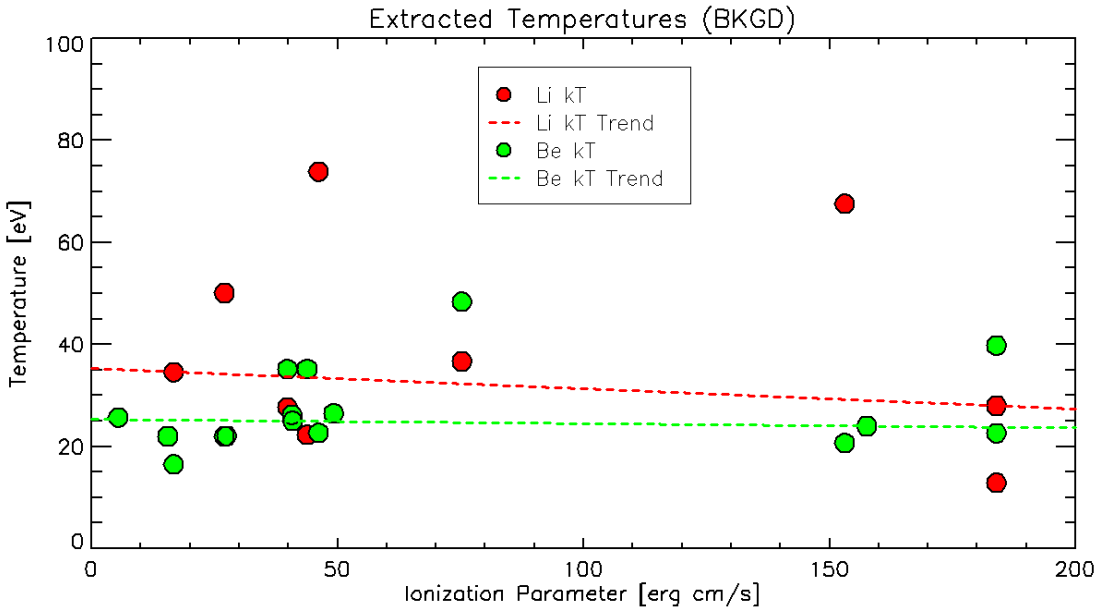

Figure 5.19: Temperatures extracted from the Li-like neon populations (red) and from the Be-like neon populations (green) from BKGD transmissions. Lines are fitted to each to guide the eye.

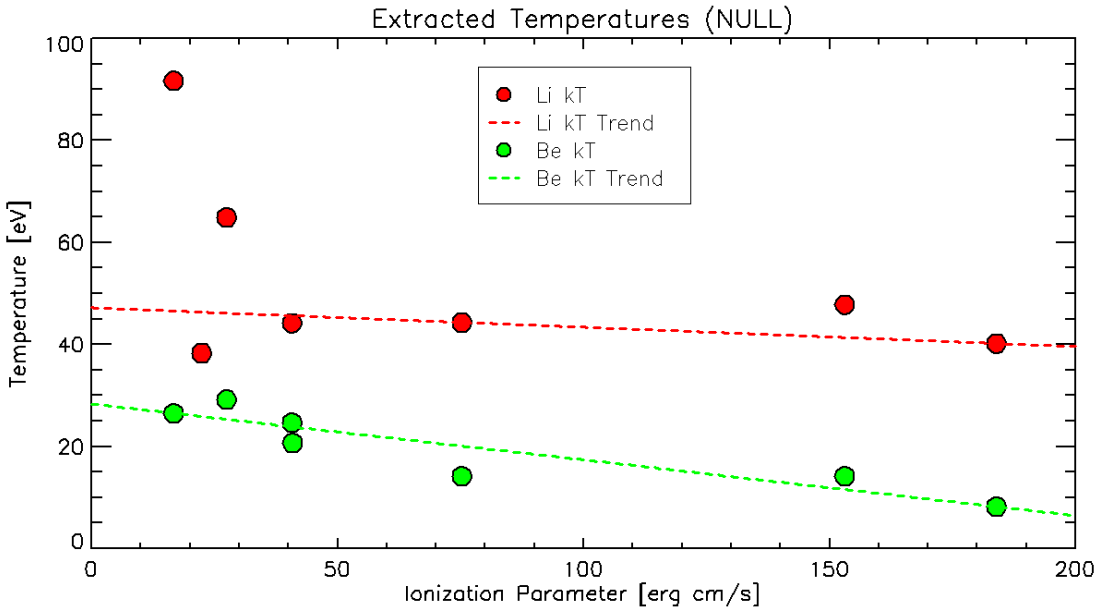

Figure 5.20: Temperatures extracted from the Li-like neon populations (red) and from the Be-like neon populations (green) from NULL transmissions. Lines are fitted to each to guide the eye.

can be seen in Figures 5.19 and 5.20, respectively. The temperature values are plotted against the ionization parameter ξ. The temperatures from the ratio of the two Li-like configuration populations are plotted in red. For the moment, focus on these. Recall that the energy separation for these levels was 16.3 eV, this being the point for 1-to-1 relative uncertainties from Equation 4.44, which begin to runaway above this. Due to this known runaway affect, the temperature scale in these plots have been cut off at a value of 100 eV, arbitrarily. In the set of Li temperature points from the BKGD transmissions, there are five points that have been cut off and ignored, meaning they were also not considered in the fitted trend line. The trend lines again use the LAD method for fitting to reduce the effect of outliers. For the NULL transmissions, two points have been cut off and ignored.

Though the points are somewhat scattered, the fitted trend lines are rather similar in slope, both being slightly downward toward higher ξ values, but the NULL trend is raised about 10 eV relative to the BKGD trend. Whether these observations actually mean anything is questionable at this point. In the BKGD set, there does look as if there is a decrease toward higher ξ values, but one must be cautioned that there are crystal artifacts that affect both the Li-2 and Li-3 groups, from which measurements are derived, and these likely affect the ratio measurement. The measurements from the NULL transmissions are seemingly less scattered, and the points themselves are pretty flat between 38 eV and 48 eV, or possibly slightly increasing, excluding the two highest measurements shown. This seems rather encouraging toward using the NULL zero-level of absorption method to try to mitigate the effects of crystal artifacts. Of course, this is all assuming that this method of temperature extraction is accurate for all of the densities involved. At this point, the method has been tested using atomic kinetics code simulations only at the highest number density in the experiments, and it was found to be in good agreement. But it is possible that the accuracy of this

method might begin to stray with lower number densities because of the assumption that the levels involved are in thermal equilibrium.

The Be-like temperature measurements are shown in green. This measurement comes from the ratio of populations from the $1s^2\ 2p^2$ and the $1s^2\ 2s^2$ configurations, which have an energy separation of 38.9 eV. This allows for a wider range of extracted temperatures before the uncertainties take over. For the measurements from this ion, there are no values that were cut off in the plots. The highest value found was the one near 50 eV in the BKGD set. Overall, the Be temperature measurements are fairly well grouped. In the BKGD set, the trend is flat when considering the whole set, but if only considering those with $\xi < 80$ erg·cm/sec, then the trend is to increase with ξ. Also note that the temperatures extracted from Be are generally lower than those extracted from Li. However, for the BKGD transmission results, it must be noted that the contamination of Si, which was unaccounted for in the background estimate, will likely have an effect on these measurements, likely making them unreliable. But an interesting thing happens in the NULL results. The points are well grouped, consistently lower than those of Li, and clearly there is a trend downward with higher ξ values. But as mentioned for Li, the trend seen here could be related to the decrease in number density that is associated with higher values of ξ, and the possible fall in accuracy of this temperature diagnostic.

The assumption for these two temperature measurement techniques is that the levels involved are in local thermal equilibrium (LTE), that is, electron collisional equilibrium. Briefly, the processes moving population between the states are collisional excitation, collisional de-excitation, spontaneous radiative decay, and since there is a substantial radiation field, also photo-excitation and stimulated emission. In the assumption for the measurements, the three radiative processes have been neglected leaving the collisional rates to dominate the balance of populations, which

results in a ratio that is at its upper limit for the given temperature. The collisional rates, however, are dependent on electron number density, and with lower number densities the collisional rates will decrease leading to a reduction in the upper level population, until the point at which there is no electron density when the radiative rates would completely determine the population balance. Essentially, reducing the density will lead to a reduction of the ratio of the upper to lower level populations, and this will result in an artificially lower extracted electron temperature. This may or may not be what is actually being seen in the Be temperature measurement, and it would apply as well to the Li temperature extraction. Simulations would need to done to find out.

Whether this is the case or not, the general range of temperatures extracted so far lead to an important confirmation. The low temperatures of these results, between 38-48 eV from Li or below 30 eV from Be, indicate that these plasmas are indeed photoionized. The ionization potential from Li-like neon to He-like neon is $\sim$240 eV, while that from He-like to H-like neon is $\sim$1200 eV. These temperatures would not lead to the ionization balance being centered around the He-like ion stage as has been seen. Also, essentially no H-like neon population would be possible by collisional ionization alone at these temperatures.

5.5 Voigt versus Stark Profiles

This section will be dedicated to discussing results from the tests involving the Stark broadened line profiles. A brief discussion of Stark profiles and how they are used was presented in Section 4.7. The idea of these tests is to gage the importance of including Stark broadened line profiles in the analysis. The broadening effect will be more visible in higher members of a series, and the effect will be larger for higher filling pressures. Both the He-like series and the Li-like series have line features that

n	**Voigt** NL [**cm**$^{-2}$]	**Stark** NL [**cm**$^{-2}$]
9	4.54E+17	6.13E+17
8	4.53E+17	5.05E+17
7	1.57E+18	5.87E+17
6	2.65E+18	5.29E+17
5	3.76E+18	5.55E+17
4	2.13E+18	7.08E+17
3	1.23E+18	1.43E+18
5-9	9.24E+17	5.53E+17

Table 5.4: Results for Stark lineshapes tests for shot z2222 side b. The first column is the principle quantum number of the upper level in the individual He-like series line feature. The second column is the result of the areal density N_iL with a Voigt line profile, and the third column is the result from the Stark broadened line profile. The results in the bottom row are from fitting He-5 through He-9 simultaneously.

include transitions to higher principle quantum numbers, and examples were shown for how the He series would be affected by this broadening.

These tests concentrate on the He series. Data from nine shots (Refer to Table 5.3) were used, and both standard Voigt profiles and the appropriate Stark profiles were used to fit line features in each spectrum. Fits were done first on each individual line, separately extracting an areal density value from each line for both Voigt and Stark lineshapes. Table 5.4 lists the results from the test performed with data from shot z2222 side b, which had a filling pressure of 30 torr. The first column is the principle quantum number of the upper level in the individual He-like series line feature. These start from the highest member visible (He-9) and work downward to the He-3 line feature. The second column is the areal density (N_iL) result with a Voigt line profile, and the third column is the result from the Stark broadened line profile. These individual line results are also plotted in Figure 5.21. The test was also run using a set of the line features simultaneously. This result is shown in the bottom row of the table, and for this piece of data the set of line features included all between He-5 and He-9.

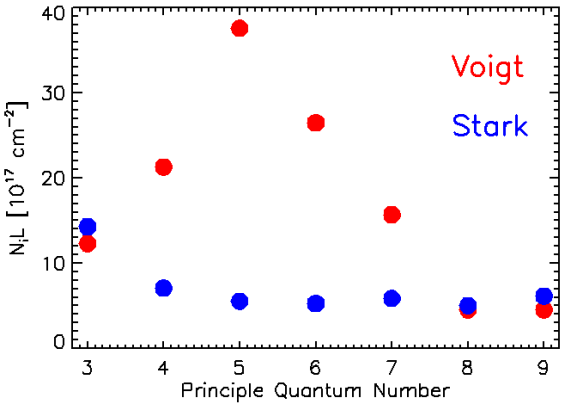

Figure 5.21: Results for Stark lineshapes tests for shot z2222 side b plotted as areal density N_iL versus principle quantum number of the upper level in the individual He-like series line feature. Results using Voigt line profiles are in red, and Stark line profiles are in blue.

These tests show a pretty clear result. Using the Voigt line profiles, beginning with He-9 and working downward, the areal density results increase by nearly an order of magnitude from He-9 to He-5. Then He-4 and He-3 decrease again by about a factor of three. The results from using Stark broadened line profiles, at least for the higher members, are very stable in comparison. The results from He-5 through He-9 are all within 20% of the mean of these five results (mean = 5.58E+17 cm^{-2}). As far as the other two line features, recall that He-4 is known to have an overlap with Li-like features, which explains the slight increase in this result since this was not taken into account. For He-3, it is possible that the effect of saturation is causing bad results. In all of the tests, He-3 and He-4 were always different from the other He series members. When running the test on He-5 through He-9 simultaneously, the result using Stark line profiles came out very close to the mean. The spectral fits are shown in Figure 5.22 showing a clear difference in the shape of the series using the different types of profiles. The top plot shows the series fitted using Voigt lineshapes. The shape of the drop off in absorption clearly does not match, that is, He-5 and He-6 are underestimated and He-8 and He-9 and over estimated in terms of

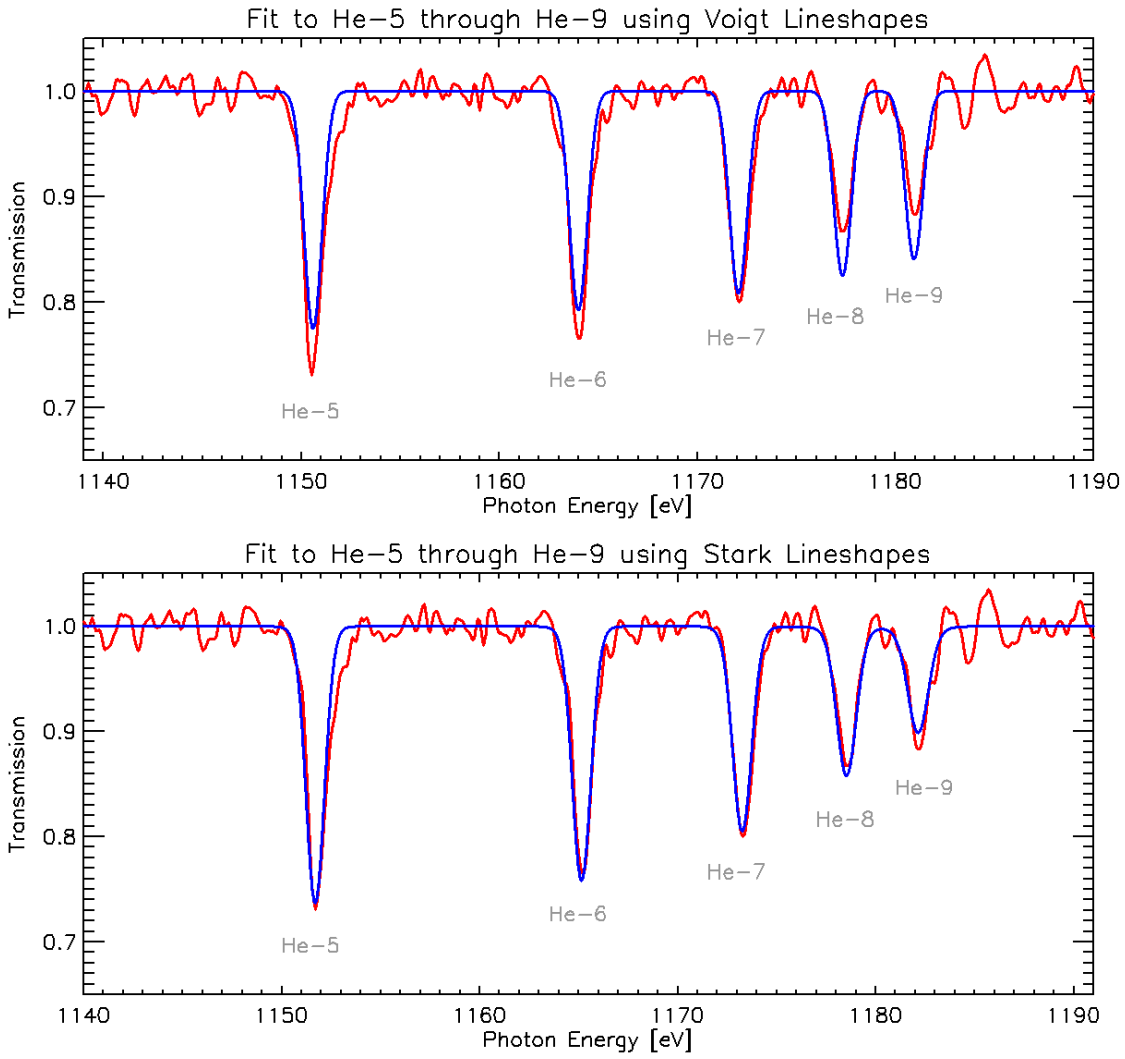

Figure 5.22: Spectral fits to shot z2222 side b transmission data using Voigt line profiles (top) and Stark broadened line profiles (bottom). The spectral fits are drawn in blue overlaid on the experimental data in red.

absorption strength. In contrast, the bottom plot shows the series fitted using Stark lineshapes. The shape of the series matches very closely. Not all of the tests were quite as conclusive as this one, but most of them were. The use of Stark broadened profiles is a necessary addition to the analysis.

The question now remains, how does the use of Stark broadened line profiles affect the results of the charge state distribution, the individual ion population fractions, and the neon total densities inferred from the summed total of measurements?

Two sets of CSD plots are shown in Figures 5.23 and 5.24 comparing the results from all of the Stark tests. They are laid out in the same manner as Section 5.2. The results shown here used the simultaneously fitted measurements, concentrating only on the upper He-like neon series (i.e. He-5 and higher). The summed total is used to calculate the population fractions. The areal density measurements for the H-like, Li-like, and Be-like populations continue to be the same values from the original standard analysis discussed prior to this section, but note that since the He-like measurements change and the summed total is used, the fractional populations of all the ions change as well. However, also note that both BKGD and NULL transmission results are included here, and their respective areal densities come from their respective original analyses. Finally, the Voigt lineshape results are, and should be, similar to the rest of the results when calculating the fractions using the summed totals, therefore Figure 5.23 is very similar to Figure 5.3.

Now, comparing Figures 5.23 and 5.24, one thing that is clear, is that in the plots containing multiple traces, the spread is reduced. This can be seen easily for the CSD of 15 torr at 4.3 cm, but is also true for the 30 torr at 4.3 cm case. There is also a change in the shapes of some of the distributions. Another interesting change is in the average ionization value $\langle Z \rangle$. Notice that in the Stark lineshape set, the $\langle Z \rangle$ values are now consistently as they would be expected, that is, increasing with lower

Voigt

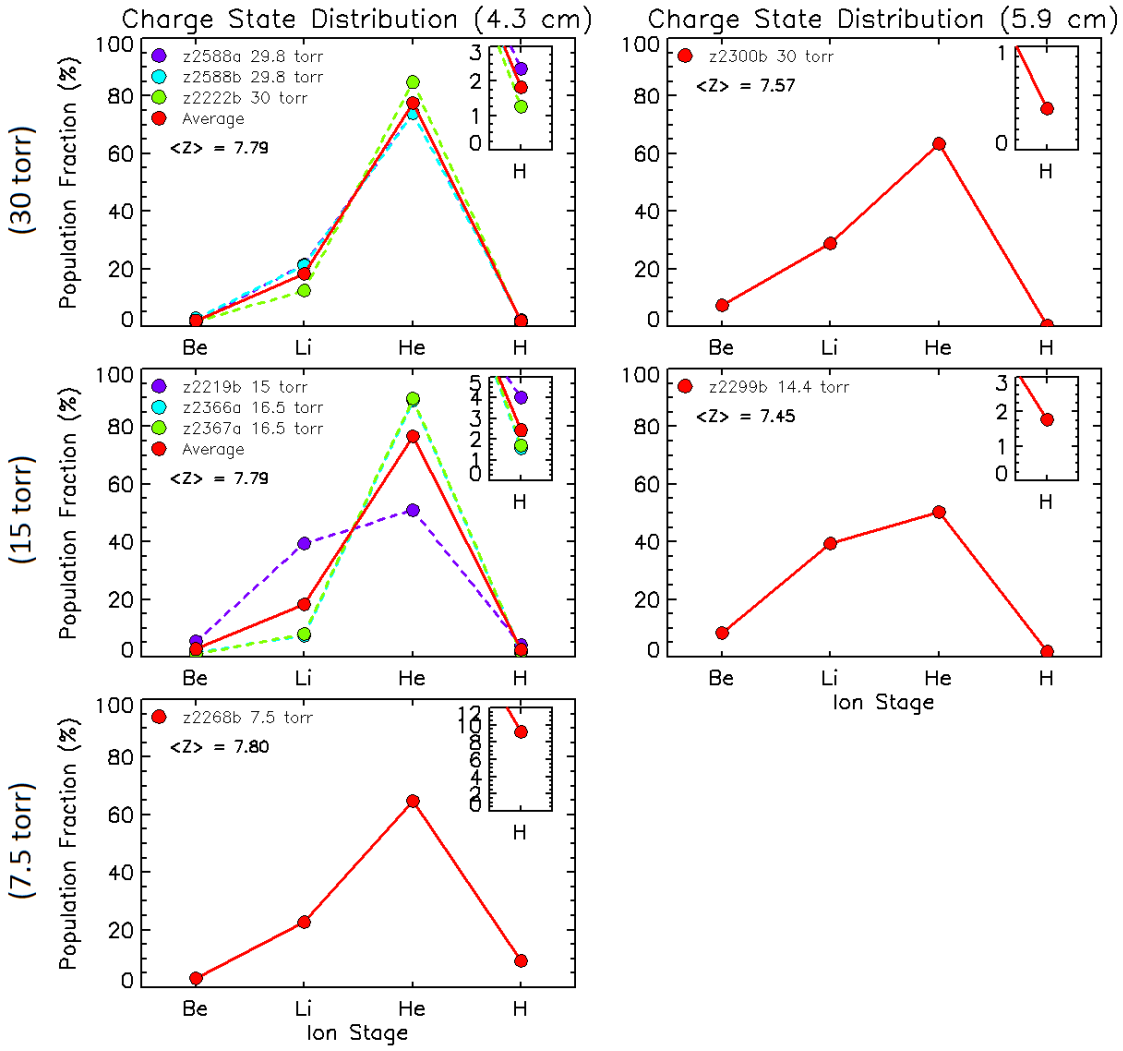

Figure 5.23: Charge state distributions using Voigt line profiles to fit the upper He-like series and the summed totals to obtain the population fractions.

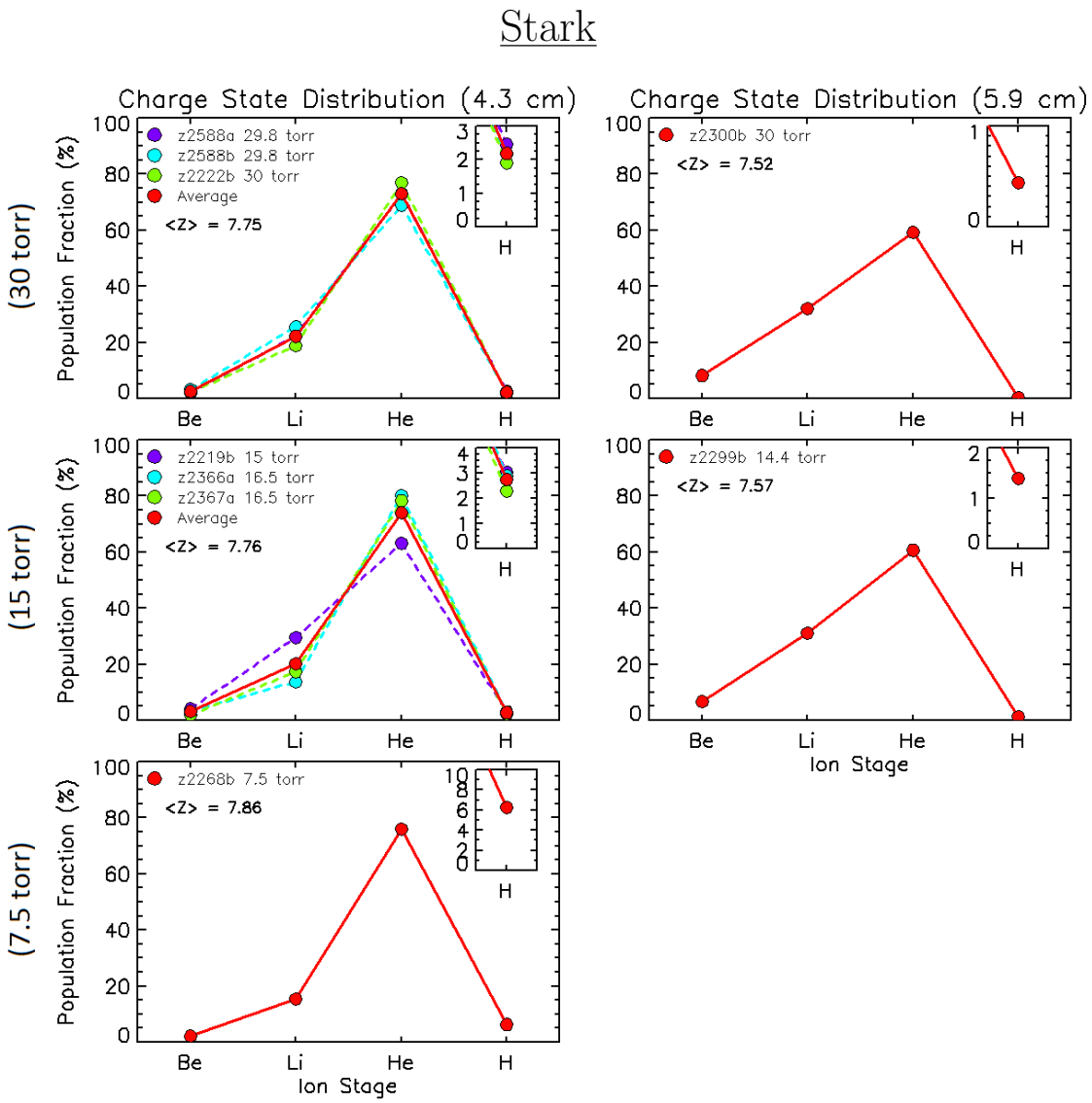

Figure 5.24: Charge state distributions using Stark line profiles to fit the upper He-like series and the summed totals to obtain the population fractions.

pressures and decreasing with lower radiation flux (i.e. further distance). This is the first set of CSD plots in which this is true. This is also somewhat encouraging.

Figures 5.25, 5.26, 5.27, and 5.28 show the individual ion fractional population results, using the summed total, plotted against ionization parameter. Again both BKGD and NULL results are plotted together, but using different colors. Voigt results are plotted as red and blue, and the Stark results are plotted as green and pink. The main thing to notice in this series of plots is that there is a fairly consistent reduction in spread seen in all of the ion fractional population results. This indicates a move in the right direction for all of these results.

Finally, let us return to Figure 5.12 once again to discuss how the totals are affected. Note that between red (Standard), green (Voigt), and blue (Stark), points from a single shot will align along the same vertical line (i.e. same horizontal value). First notice that comparing the Voigt points with the corresponding Standard points from the same shot, most of these points match well, that is, they overlap. However, for the points above the line of equality, there are incremental improvements. A first improvement is seen between the Standard analysis and Voigt results, which concentrated only on the upper series lines, and there is a further improvement when using Stark lineshapes, which brings both of the results for the two shots nearly all the way down to the line of equality. This seems to be a significant improvement to these two shots that have been outliers previously. As for the rest of the points for the Stark test, the summed totals for the three at lower pressures rise slightly toward the line of equality, while the four at the highest pressure all drop slightly away from the line of equality. Given the limited number of points for this test, it is difficult to say with certitude that this is significant, or to explain why it might have happened. One idea might be that it relates to the expanding column of directly irradiated gas in the gas cell.

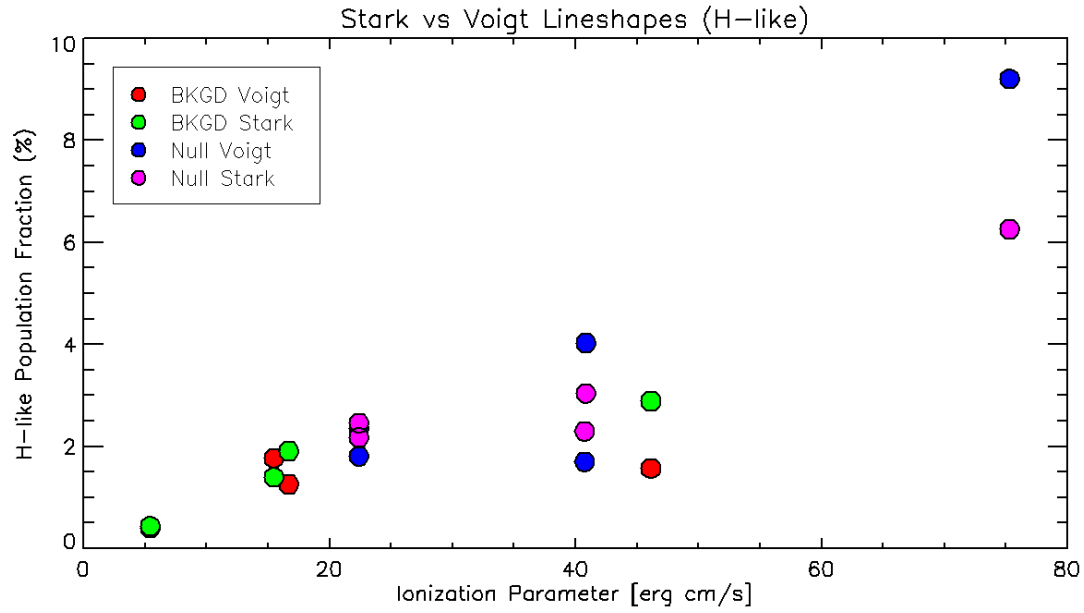

Figure 5.25: Fractional population versus ionization parameter for H-like neon comparing the results from Voigt line profiles and Stark line profiles. Red and blue points are Voigt results, and green and pink points are Stark results.

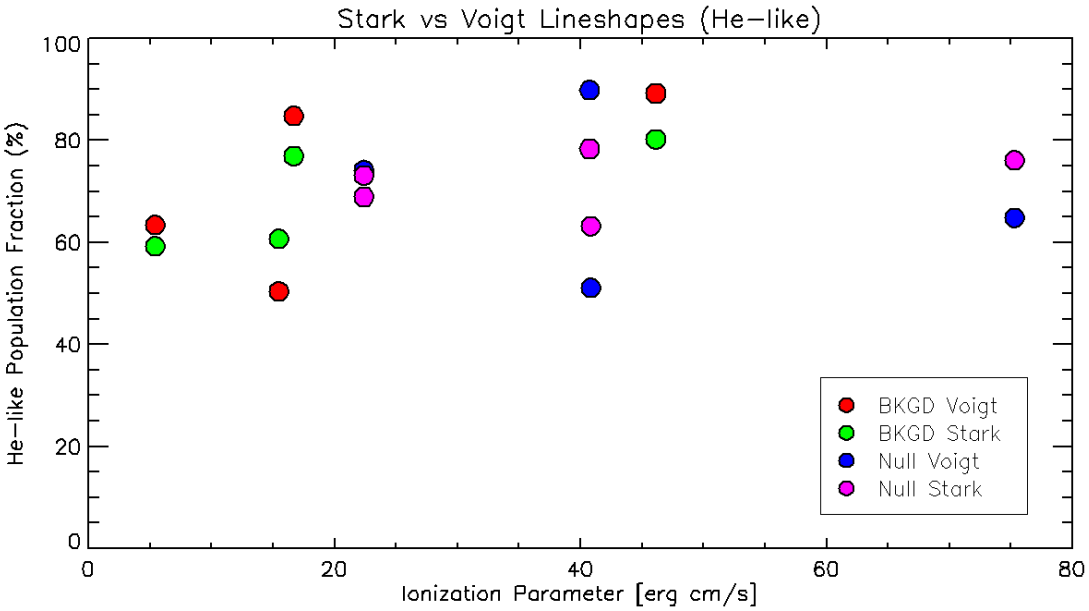

Figure 5.26: Fractional population versus ionization parameter for He-like neon comparing the results from Voigt line profiles and Stark line profiles. Red and blue points are Voigt results, and green and pink points are Stark results.

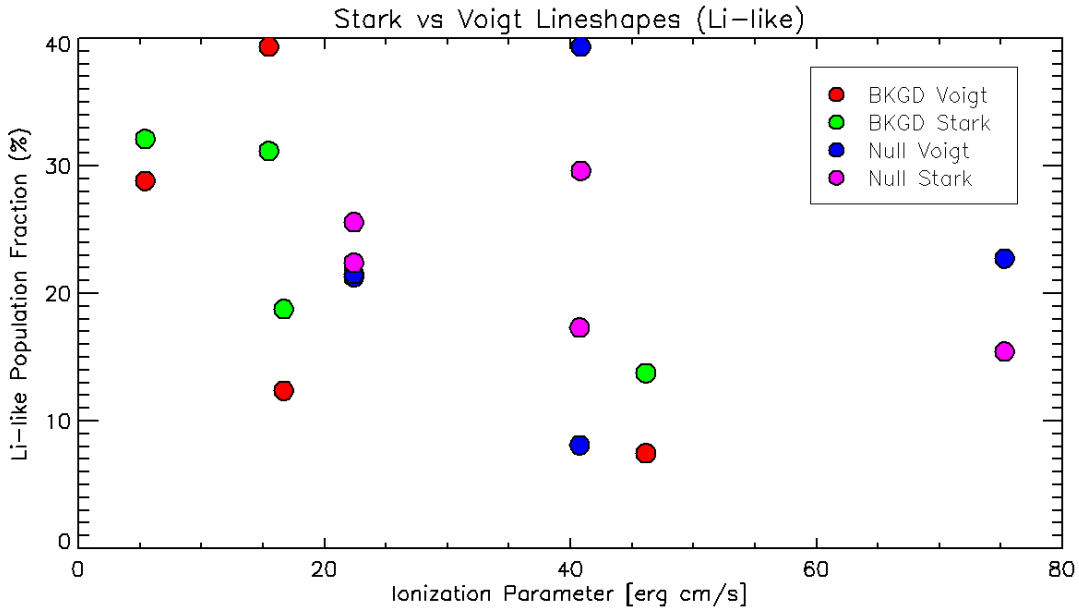

Figure 5.27: Fractional population versus ionization parameter for Li-like neon comparing the results from Voigt line profiles and Stark line profiles. Red and blue points are Voigt results, and green and pink points are Stark results.

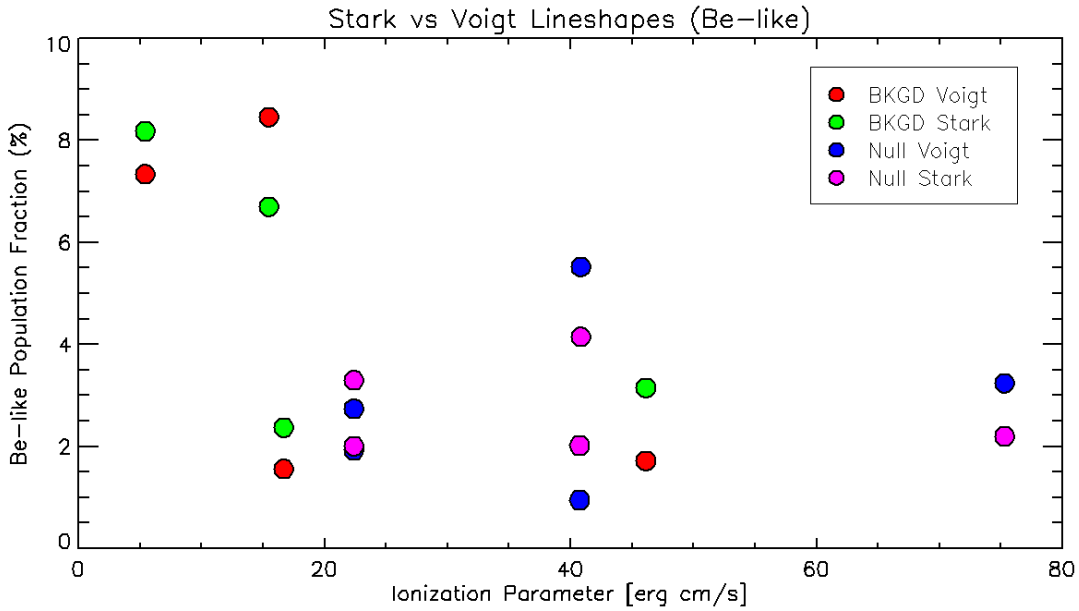

Figure 5.28: Fractional population versus ionization parameter for Be-like neon comparing the results from Voigt line profiles and Stark line profiles. Red and blue points are Voigt results, and green and pink points are Stark results.

5.6 Averaging of Results

At this point in time, the H-like population fraction measurements are clearly the most robust, showing relative consistency across all methods, and showing a clear trend in the fractional populations. Because there is some level of uncertainty associated with each point for different reasons, the idea has arisen of what would happen if some of the points were averaged together. First of all, the focus is going to be on the most populated area of the plot space, below $\xi = 80$ erg·cm/sec, where the measurements are thought to be the most reliable. Figure 5.29 zooms in to this area of Figure 5.13 to show the points more clearly. Both BKGD and NULL results will be considered.

Now, there are two ways to average results. One could go back to the spectral data and average multiple shot spectra, which could be done by either averaging the final transmissions for the shots or by averaging the individual slit spectra from the shots earlier on in the processing. Either way, this is one way of averaging points, which will be referred to as "data averaging". The other way, is by simply averaging the final results as they are, which will be referred to as "point averaging". In this case, both the fractions and ionization parameters would be averaged to produce the final point. To do it either way, there must be some rules established to dictate what can and what cannot be averaged. The general rules are as follows:

1. Data must be time-integrated.
2. Pressures should be similar.
3. Distances must be the same.
4. Incident radiation flux should be similar.
5. Ionization parameter should be similar.

6. Window thickness should be the same.

   * There were two experiments done using 200 nm thick Si_3N_4 windows on the rear side to test whether effects from shocks could be detected.

Additionally, for data averaging, if doing the averaging earlier in the processing, then the crystal used in each spectrum must be the same. Averaging transmissions would be preferred, in which case the particular crystal associated with a piece of data becomes less important.

In the past there were a few data averages done, however, after revising the pressures, only one remained valid according to the rules, and it is included here. The rest of the averages are point averages. There are four of these. Three of these were averages between the BKGD result and the NULL result for a given shot, and one of those included the results from two shots, z2219b and z2367a. The other was an average of the results from the two TREX sides.

Figure 5.30 shows the results after averaging has been done. The scatter in the points is reduced, and the trend becomes even more clear. A parabolic curve is fitted, showing a very slight upward curvature in the trend. Overall, the trend is very close to linear in this region of ionization parameter space where the fraction of H-like neon is still relatively small. The region that is seen here has data points covering more than an order of magnitude in ionization parameter values, this being the first time such an extensive set of experimental data points has been collected for plasma in this regime.

The uncertainties for these measurements are difficult to quantify with all of the factors that are involved. There is uncertainty along both axes. The uncertainty in ξ will come from the uncertainty of the neon filling pressure measurement, average ionization, and radiation intensity. Which of these will contribute the most uncertainty is, at this point, difficult to say. As for the uncertainty in the fractional populations,

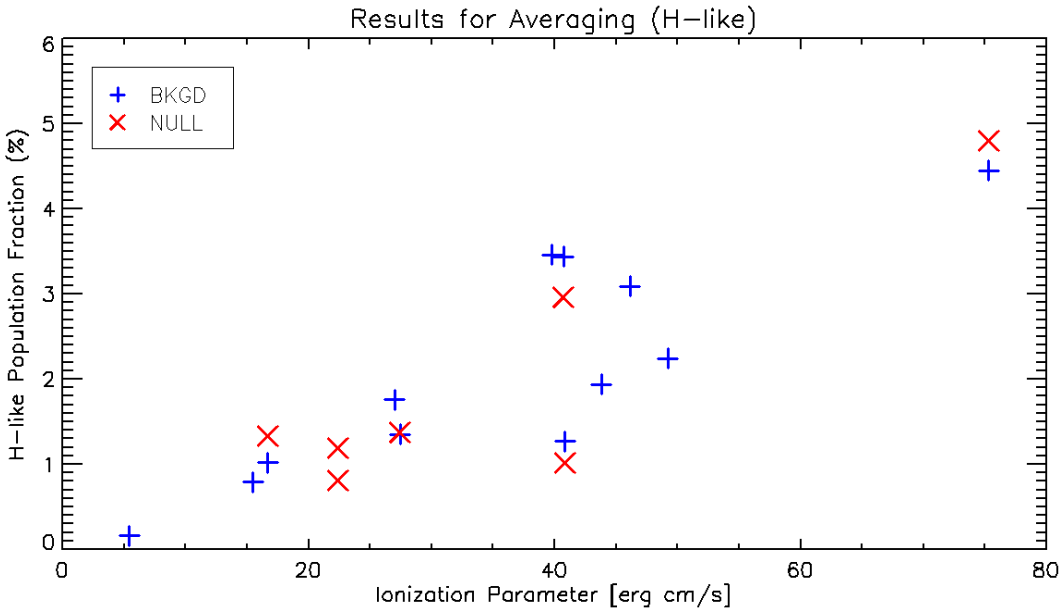

Figure 5.29: Region from Figure 5.13 to be focused on for averaging results.

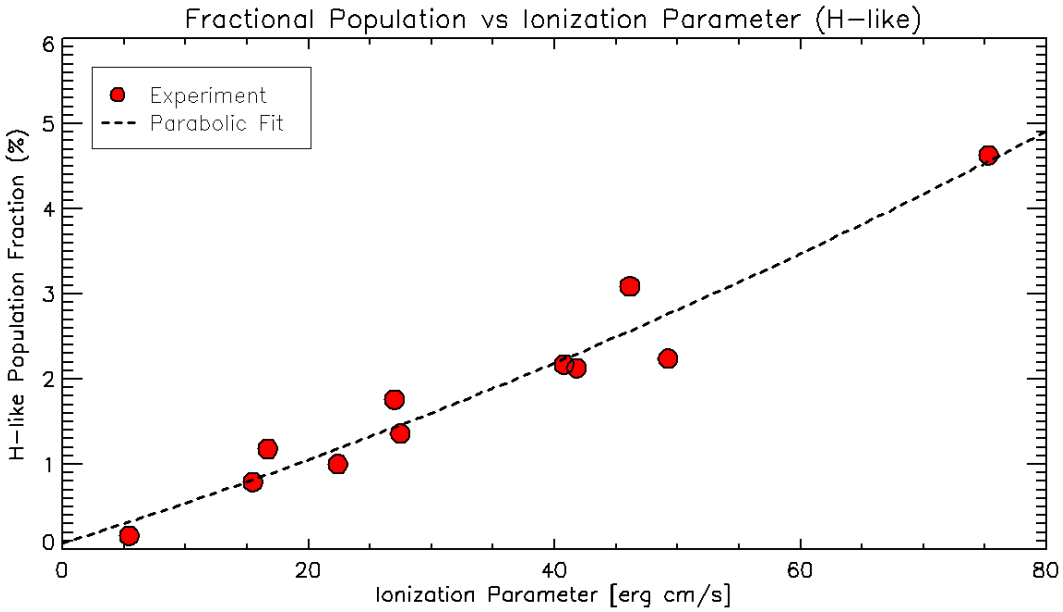

Figure 5.30: Final averaged results for H-like neon fractional populations. A parabolic curve is fitted and shown by the dashed line.

there are many factors that can contribute. The largest of these are likely to be related to the zero-level of absorption estimate, the total neon density used to compute the fraction, and the fact that the second order reflection photon correction has not yet been included in the data processing. The last of these will only raise the measured areal densities, but it may affect each ion stage differently because the correction is photon energy dependent. At this point, it is unknown how large of an effect will result, but it is thought to be small. Regarding the total neon densities used, the discrepancies that were found between the summed totals and pressure totals indicate that something is not fully understood. In this regard, the H-like fractional populations showed robustness in that comparing the values calculated using summed totals and pressure totals showed relatively small variation. Ultimately, the quantification of uncertainties is a work in progress and may be better to do once the new methods have been fully integrated into the data processing and analysis protocols.

Chapter 6

Conclusion

Several results presented here begin to paint a picture of the plasma being created in these experiments at Z and how the different parameters affect it. To begin with, the He-like ion stage dominates the ion populations of the plasma, with somewhere between 50% and 90% of the neon being in this stage, depending on which methods are used. With the closure relation method for calculating the fractional population, a downward trend in ionization parameter appeared in this stage, and the fractions were constrained to above 60% for the BKGD method and above 70% for the NULL method. The downward trend is interesting, if it is real, because atomic kinetics simulations run by Ref. [44] have indicated that the regime these experiments are in may be on a plateau for the He-like fraction but very near a tipping point where the ion population may be beginning to flow more from the He-like stage into the H-like stage. Reaching higher ionization parameter values will shine more light on this.

H-like neon was present and was found to increase nearly linearly with ionization parameter in the range where the data seems most reliable. It increases from below 1% when $\xi < 20$ erg·cm/sec, up to around 3% near $\xi = 50$ erg·cm/sec, and seems to hit 5% before $\xi = 100$ erg·cm/sec. The way the measurements of this series were relatively unchanged throughout all of the different methods suggests that this

measurement is somewhat robust. Though there must be caution in this due to the fact that the contribution to the spectra from second order reflection photons has not yet been accounted for. It is still unsure how much of an effect this will have on the set of ion population measurements; however, it should be a consistent change within each ion species if it is indeed significant at all.

The Li-like and Be-like ion populations are still on the uncertain side. The main reasons for this in the Li-like stage is that there are significant crystal artifacts that happen to affect both main sections of the spectrum where this measurement comes from, and aside from this, the signal for this series drops considerably for lower filling pressures making it much more difficult to distinguish Li-like neon features from noise or artifacts. The NULL method of background estimation clearly helped to reduce the uncertainty somewhat, but it is still far from perfect. I'd like to take a moment to explain this.

Often times, there are mismatches between neon data and null data, which limit how appropriate some pieces of null shot data are for use with neon data. The most important mismatch is in the location of the reflection on the crystal of the slit images. Visible features of the crystal (i.e. dark curved lines, bright and dark spots, etc.) that appear in the spectra can be shifted or not present in other spectra. But many of these features are inherent to the crystal itself and are always somewhere in the image plane. The spectral slit images always contain some area of these crystal features, which can appear as bumps or dips in the extracted spectra, and if they are shifted for different spectra, then the bumps and dips will be shifted in some way or completely different as they appear in the various extracted spectra. One way that this could possibly be accounted for and mitigated to help the usefulness of null data is by creating a "flat-field" image of the crystal surface. This may be able to be done using many pieces of spectral data and aligning them according to these crystal features

in order to combine them to obtain one image with a large portion of these features visible. Then spectral images, including the null spectra, could be corrected using a slice of this master image from the appropriate location. This slice could then be used to raise or lower the intensity values of each pixel in the spectral image to effectively remove the crystal features, just as one would do when using a flat-field image in astronomical data from a telescope. Another way of making a flat-field image of the crystal would require a Z shot (which may be out of the question), in which either wider slits were used, or the slits could be replaced by a filter that would still allow radiation to pass through, illuminating the entire crystal, while also blocking debris.

As for the Be-like ion measurements, these carry uncertainty for a different reason. The spectral features used for this measurement are contaminated by Si ion absorption from the Si_3N_4 windows that have been used in the GEN2 configuration of experiments. Using the NULL method affects this ion stage measurement greatly by helping to remove some of this contamination. This is very encouraging, but more tests are needed to make sure that this is done properly. There are multiple factors here, one of which relates to the photon energy calibration. These line features are on the outside of the major lines used to perform the photon energy calibration, which means that rather than interpolating at this position, it is extrapolating, which carries a greater uncertainty. The positions of the Si features in the null data and the combined Si-Be features in the neon data must be aligned properly for the removal of the Si to be correct. What was presented here was a best effort using what tools were available, but there is more that should be done to improve our confidence. On top of this, accounting for the second order reflection photons may have a larger effect on this ion's measurement than the other three.

The electron temperature measurements depend upon the two ion species measurements that are, at this point, the most uncertain, with the NULL background

estimation method offering a somewhat higher level of confidence. Temperatures extracted from Li-like neon levels seem to give a relatively flat distribution of temperatures between 35-50 eV, but there are many rather high values that came from this measurement as well. Whereas the temperatures extracted from Be-like neon levels are lower and more consistent overall, and they show a downward trend with higher ξ value. This downward trend may be indicative of a possible systematic error in this method that is dependent on density as was explained in Chapter 5. If this is the case, there may be a way of correcting for it by including information about how the collisional excitation and de-excitation rates change with density. This should be investigated through simulations.

There is an important point to make about the level of temperatures that are being seen from the measurements. They are a confirmation that these plasmas are indeed photoionized. The ionization potential from Li-like neon to He-like neon is $\sim$240 eV, while that from He-like to H-like neon is $\sim$1200 eV. If these plasmas were more toward the collisionally dominated end of the plasma type spectrum, they would not lead to the ionization balance being centered around the He-like ion stage, nor would there be the level of H-like neon present as has been seen.

For the value of the average ionization $\langle Z \rangle$, in most of the results presented, the value clearly decreased with the further position (i.e. reduced radiation flux) as was expected. But the expected trend was not observed with density until Stark broadened line profiles were included in the measurement of the He-like areal densities. This is, at the very least, encouraging. However, including the Stark broadened profiles also significantly improved the shape of the He-like neon series in the spectral fit and helped stabilize the areal density values extracted from the series. Overall, a reduction in the spread of values of all ions was seen as a result. Stark broadened line profiles seem to be a necessary addition to the analysis procedure. This will also

require implementing this into the measurement of the Li-like neon series because it also contains spectral features from transitions to levels with relatively higher principle quantum numbers, which will be more affected by external fields.

One issue that was observed in the results was in the comparison between the summed total of the measured ion densities and the densities retrieved from the filling pressures. While it seems that improvements came from using Stark broadened line profiles, it is not entirely clear that it helped regarding this, except for the outliers. Most of the summed totals are less than the pressure totals, which may suggest an interesting side-effect of having a limited volume of the neon gas directly irradiated by the Z-pinch. It seems plausible that due to the pressure gradient created between the irradiated plasma column and the cooler surrounding gas, that there might be an expansion of the plasma column that might lead to this result. This should also be investigated through simulations. The correction for the second order reflection photons could also have an effect on this comparison, so it must also be implemented into the data processing procedure in order to make sure the extracted measurements are correct.

Another issue to point out relates to the time-dependent nature of this experiment, which may be having an effect on the measurements as well. It's true that most of the light contributing to the spectra comes from near the peak of the drive and that the conditions of the plasma during this time should have the largest influence on the absorption spectra. But a lot of the light also comes from areas outside the peak of the drive during which the conditions of the plasma are different. Contributions to the spectra coming from before the peak will have larger amounts of Li-like and Be-like ions, increasing the amount of absorption in these features. Also before the peak there might not be many H-like ions, reducing the amount of absorption in this ion stage. After the peak, the plasma will begin recombining. This will also add

to the amount of Li-like and Be-like absorption seen in the spectrum. So we might expect the measurements of the Li-like and Be-like ion stages to be on the high side, while expecting the H-like measurements to be on the low side. But regarding this, it is difficult to say with certitude whether this affect is actually seen or not, until we work more with the time-resolved data that is available.

It should be reiterated to make clear, that the "results" from the previous chapter are from spectra from what are essentially test results of the different processing and analysis methods that have been explored. At this point, what is essential to do, is to go through all of the data in this dataset once more, along with the data from the GEN1 experiments, using only the newest and best methods that have been found, in a consistent manner, so that all of the results from that "run" are on equal footing. This seems to be essential for trying to get a clear understanding and characterization of the plasmas generated in these experiments.

Bibliography

[1] R. C. Mancini, J. E. Bailey, J. F. Hawley, T. Kallman, M. Witthoeft, S. J. Rose, and H. Takabe. Accretion disk dynamics, photoionized plasmas, and stellar opacities. *Physics of Plasmas*, 16:041001, 2009.

[2] George H. Jacoby, Gary J. Ferland, and Kirk T. Korista. The planetary nebula A39: An observational benchmark for numerical modeling of photoionized plasmas. *The Astrophysical Journal*, 560:272, 2001.

[3] D. E. Osterbrock and G. J. Ferland. *Astrophysics of Gaseous Nebulae and Active Galactic Nuclei*. University Science Books, second edition, 2005.

[4] M. Hanke, J. Wilms, M. A. Nowak, K. Pottschmidt, N. S. Schulz, and J. C. Lee. Chandra X-ray spectroscopy of the focused wind in the Cygnus X-1 system. I. The nondip spectrum in the low/hard state. *The Astrophysical Journal*, 690:330, 2009.

[5] T. Kallman and M. Bautista. Photoionization and high-density gas. *The Astrophysical Journal Supplement Series*, 133:221, 2001.

[6] G. J. Ferland, R. L. Porter, P. A. M. van Hoof, R. J. R. Williams, N. P. Abel, M. L. Lykins, Gargi Shaw, W. J. Henney, and P. C. Stancil. The 2013 Release of Cloudy. *Revista Mexicana de Astronomia y Astrofisica*, 49:1, 2013.

[7] S. J. Rose. The non-LTE excitation/ionization code GALAXY. *Journal of Physics B*, 31:2129, 1998.

[8] J. J. MacFarlane and et al. Simulation of the ionization dynamics of aluminum irradiated by intense short-pulse lasers. In *Proceedings of Inertial Fusion and Science Applications 2003*, La Grange Park, IL, 2004. American Nuclear Society.

[9] J. J. MacFarlane, I. E. Golovkin, P. Wang, P. R. Woodruff, and N. A. Pereyra. SPECT3D – A multi-dimensional collisional-radiative code for generating diagnostic signatures based on hydrodynamics and PIC simulation output. *High Energy Density Physics*, 3:181, 2007.

[10] H. A. Scott and R. W. Mayle. GLF - A Simulation Code for X-Ray Lasers. *Applied Physics B*, 58:35, 1994.

[11] J. E. Bailey, D. Cohen, G. A. Chandler, M. E. Cuneo, M. E. Foord, R. F. Heeter, D. Jobe, P. Lake, D. A. Liedahl, J. J. MacFarlane, T. J. Nash, D. Nielson, R. Smelser, and W. A. Stygar. Neon photoionization experiments driven by Z-pinch radiation. *Journal of Quantitative Spectroscopy and Radiative Transfer*, 71:157, 2001.

[12] I. M. Hall, T. Durmaz, R. C. Mancini, J. E. Bailey, G. A. Rochau, M. J. Rosenberg, D. Cohen, I. E. Golovkin, J. J. MacFarlane, M. E. Sherril, J. Abdallah, R. F. Heeter, M. E. Foord, S. H. Glenzer, and H. A. Scott. Modelling, design and diagnostics for and photoionised plasma experiment. *Astrophysics and Space Science*, 322:117, 2009.

[13] G. A. Rochau, J. E. Bailey, R. E. Falcon, G. P. Loisel, T. Nagayama, R. C. Mancini, I. Hall, D. E. Winget, M. H. Montgomery, and D. A. Liedahl. ZAPP: The Z Astrophysical Plasma Properties collaboration. *Physics of Plasmas*, 21:056308, 2014.

[14] R. E. Falcon, G. A. Rochau, J. E. Bailey, J. L. Ellis, A. L. Carlson, T. A. Gomez, M. H. Montgomery, D. E. Winget, E. Y. Chen, M. R. Gomez, and T. J. Nash. An experimental platform for creating white dwarf photospheres in the laboratory. *High Energy Density Physics*, 9:82, 2013.

[15] J. E. Bailey, G. A. Rochau, R. C. Mancini, C. A. Iglesias, J. J. MacFarlane, I. E. Golovkin, C. Blancard, Ph. Cosse, and G. Faussurier. Experimental investigation of opacity models for stellar interior, inertial fusion, and high energy density plasmas. *Physics of Plasmas*, 16:058101, 2009.

[16] R. F. Heeter, J. E. Bailey, M. E. Cuneo, J. Emig, M. E. Foord, P. T. Springer, and R. S. Thoe. Plasma diagnostics for x-ray driven foils at Z. *Review of Scientific Instruments*, 72:1224, 2001.

[17] M. E. Foord, R. F. Heeter, P. A. M. van Hoof, R. S. Thoe, J. E. Bailey, M. E. Cuneo, H.-K. Chung, D. A. Liedahl, K. B. Fournier, G. A. Chandler, V. Jonauskas, R. Kisielius, L. P. Mix, C. Ramsbottom, P. T. Springer, F. P. Keenan, S. J. Rose, and W. H. Goldstein. Charge-state distribution and doppler effect in an expanding photoionized plasma. *Physical Review Letters*, 93:5, 2004.

[18] M. E. Foord, R. F. Heeter, H.-K. Chung, P. A. M. van Hoof, J. E. Bailey, M. E. Cuneo, D. A. Liedahl, K. B. Fournier, V. Jonauskas, R. Kisielius, C. Ramsbottom, P. T. Springer, F. P. Keenan, S. J. Rose, and W. H. Goldstein. Study of X-ray photoionized Fe plasma and comparisons with astrophysical modeling codes. *Journal of Quantitative Spectroscopy and Radiative Transfer*, 99:712, 2006.

[19] Fei lu Wang, Shinsuke Fujioka, Hiroaki Nishimura, Daiji Kato, Yu tong Li, Gang Zhao, Jie Zhang, and Hideaki Takabe. Experimental evidence and theoretical

analysis of photoionized plasma under x-ray radiation produced by an intense laser. *Physics of Plasmas*, 15:073108, 2008.

[20] Fei lu Wang, Gang Zhao, David Salzmann, Hiroaki Nishimura, Shinsuke Fujioka, Yu tong Li, Hideaki Takabe, and Jie Zhang. Comparison between simulated and experimental emission spectra of photoionizing nitrogen plasma. *High Energy Density Physics*, 5:219, 2009.

[21] E. Hill and S. Rose. Photoionized astrophysical plasmas in the laboratory. *Physics of Plasmas*, 17:103301, 2010.

[22] C. B. Tarter, W. H. Tucker, and E. E. Salpeter. The interaction of x-ray sources with optically thin environments. *The Astrophysical Journal*, 156:943, 1969.

[23] Sandia National Laboratories. Z pulsed power facility. `http://www.sandia.gov/z-machine/`, 2014.

[24] Sandia National Laboratories. How Does the Z Machine Work? `http://www.sandia.gov/z-machine/about_z/how-z-works.html`, 2014.

[25] D. L. Cook, G. 0. Allshouse, J. Bailey, G. W. Barr, J. D. Boyes, E. L. Burgess, W. B. Boyer, J. S. Cap, R. S. Coats, P. L. Dreike, H. G. Fifer, J. P. Furaus, R. A. Gerber, S. Goldsmith, S. A. Goldstein, R. A. Hamil, D. R. Humphreys, R. J. Leeper, D. H. McDaniel, T. H. Martin, C. W. Mendel Jr. and P. A. Miller, L. P. Mix, E. L. Neau, J. N. Olsen, G. D. Peterson, K. R. Prestwich, J. P. Quintenz, G. E. Rochau, S. E. Rosenthal, D. C. Rovang, C. L. Ruiz, L. Schneider, L. 0. Seamons, D. B. Seidel, T. N. Simmons, S. A. Slutz, R. W. Stinnett, W. A. Stygar, M. A. Sweeney, K. M. Tolk, B. N. Turman, J. M. Wilson, and J. P. VanDevender. Progress in light ion beam fusion research on PBFA II. *Plasma Physics and Controlled Fusion*, 28:1921, 1986.

[26] R. B. Spielman, F. Long, T. H. Martin, J. W. Poukey, D. B. Seidel, W. Shoup, W. A. Stygar, D. H. McDaniel, M. A. Mostrom, K. W. Struve, P. Corcoran, I. Smith, and P. Spence. PBFA II-Z: A 20-MA driver for Z-pinch experiments. In *Tenth IEEE International Pulsed Power Conference*, volume 1, page 396, 1995.

[27] R. B. Spielman, C. Deeney, G. A. Chandler, M. R. Douglas, D. L. Fehl, M. K. Matzen, D. H. McDaniel, T. J. Nash, J. L. Porter, T. W. L. Sanford, J. F. Seamen, W. A. Stygar, K. W. Struve, S. P. Breeze, J. S. McGurn, J. A. Torres, D. M. Zagar, T. L. Gilliland, D. O. Jobe, J. L. McKenney, R. C. Mock, M. Vargas, T. Wagoner, and D. L. Peterson. Tungsten wire-array Z-pinch experiments at 200 TW and 2 MJ. *Physics of Plasmas*, 5:2105, 1998.

[28] M. Keith Matzen and et. al. Pulsed-power-driven high energy density physics and inertial confinement fusion research. *Physics of Plasmas*, 12:055503, 2005.

[29] R. J. Leeper and et. al. Time- and space-resolved elliptical crystal spectrometers for high energy density physics research. *Nuclear Fusion*, 39(9):1283, 1999.

[30] G. B. Rybicki and A. P. Lightman. *Radiative Processes in Astrophysics*. John Wiley and Sons, Inc., 1979.

[31] I. M. Hall, T. Durmaz, R. C. Mancini, J. E. Bailey, and G. A. Rochau. Radiation hydrodynamic simulation of a photoionised plasma experiment at the Z facility. *Astrophysics and Space Science*, 336:189, 2011.

[32] J. J. MacFarlane. VISRAD - A 3-D viewfactor code and design tool for high-energy density physics experiments. *Journal of Quantitative Spectroscopy and Radiative Transfer*, 81:287, 2003.

[33] G. P. Loisel. Radiation drive determination for astrophysical plasma experiments on Z. *Review of Scientific Instruments*, 2014. unpublished.

[34] B. L. Henke, E. M. Gullikson, and J. C. Davis. X-ray interactions: photoabsorption, scattering, transmission, and reflection at E=50-30000 eV, Z=1-92, Atomic Data and Nuclear Data Tables, July 1993.

[35] T. Nash. Private communication.

[36] G. B. Zimmerman and W. L. Kruer. The lasnex code for inertial confinement fusion. *Comments in Plasma Physics and Controlled Thermonuclear Fusion*, 2:85, 1975.

[37] T. E. Lockard and R. Falcon. Private communication.

[38] P. W. Lake, J. E. Bailey, G. A. Rochau, T. C. Moore, D. Petmecky, and P. Gard. Time- and space-resolved elliptical crystal spectrometers for high energy density physics research. *Review of Scientific Instruments*, 75(10):3690, 2004.

[39] P. W. Lake, J. E. Bailey, G. A. Rochau, P. Gard, D. Petmecky, M. Bump, N. R. Joseph, T. C. Moore, and L. B. Nielsen-Weber. Time- and space-resolved elliptical crystal spectrometers for high energy density physics research. *Review of Scientific Instruments*, 77:10F315, 2004.

[40] B. L. Henke, S. L. Kwok, J. Y. Uejio, H. T. Yamada, and G. C. Young. Low-energy x-ray response of photographic films. I. Mathematical models. *Journal of the Optical Society of America B*, 1(6):818, 1984.

[41] B. L. Henke, F. G. Fujiwara, M. A. Tester, C. H. Dittmore, and M. A. Palmer. Low-energy x-ray response of photographic films. II. Experimental characterization. *Journal of the Optical Society of America B*, 1(6):828, 1984.

[42] J. L. Wiza. Microchannel plate detectors. *Nuclear Instruments and Methods*, 162:587, 1979.

[43] G. A. Rochau, J. E. Bailey, G. A. Chandler, T. J. Nash, D. S. Nielson, G. S. Dunham, O. F. Garcia, N. R. Joseph, J. W. Keister, M. J. Madlener, D. V. Morgan, K. J. Moy, and M. Wu. Energy dependent sensitivity of microchannel plate detectors. *Review of Scientific Instruments*, 77:10E323, 2006.

[44] T. E. Lockard. Private communication.

[45] I. M. Hall. Private communication.

[46] G. A. Rochau. *Radiative Transfer in Low-Density, Low-Z Foam*. PhD thesis, University of Wisconsin, Madison, 2003. unpublished.

[47] Rafael C. Gonzalez and Richard E. Woods. *Digital Image Processing*. Pearson Prentice Hall, third edition, 2008.

[48] T. Durmaz. *Theoretical study of neon photoionized plasma*. PhD thesis, University of Nevada, Reno, 2014.

[49] Dimitri Mihalas. *Stellar Atmospheres*. W. H. Freeman and Company, San Fransisco, second edition, 1978.

[50] M. F. Gu. The flexible atomic code. *Canadian Journal of Physics*, 86(5):675, 2008.

[51] S. R. Drayson. Rapid computation of the voigt profile. *Journal of Quantitative Spectroscopy and Radiative Transfer*, 16:611, 1976.

[52] H. C. Ives, W. A. Stygar, D. L. Fehl, L. E. Ramirez, S. C. Dropinski, D. L. Wall, J. S. Anctil, J. S. McGurn, J. H. Pyle, D. L. Hanson, B. N. Allison, M. J. Berninger, E. A. Bryce, G. A. Chandler, M. E. Cuneo, A. J. Fox, T. L. Gilliland, C. L. Haslett, R. J. Leeper, D. F. Lewis, M. A. Lucero, M. G. Mazarakis, D. H. McDaniel, J. L. McKenney, J. A. Mills, L. P. Mix, J. L. Porter, M. B. Ritchey, L. E. Ruggles, J. F. Seamen, W. W. Simpson, R. B. Spielman, J. A. Torres, M. F. Vargas, T. C. Wagoner, L. K. Warne, and M. W. York. Measurement of the energy and power radiated by a pulsed blackbody x-ray source. *Physical Review Special Topics ? Accelerators and Beams*, 9:110401, 2006.

[53] R. C. Mancini. HED Plasma Spectroscopy lecture series. 2013.

[54] R. C. Mancini. Private communication.

[55] L. A. Woltz and C. F. Hooper Jr. Calculation of spectral line profiles of multielectron emitters in plasmas. *Physical Review A*, 38:4766, 1988.

[56] R. C. Mancini, D. P. Kilcrease, L. A. Woltz, and C. F. Hooper Jr. Calculational aspects of the Stark line broadening of multielectron ions in plasmas. *Computer Physics Communications*, 63:314, 1991.

[57] I. M. Hall, T. Durmaz, R. C. Mancini, J. E. Bailey, G. A. Rochau, I. E. Golovkin, and J. J. MacFarlane. Absorption spectroscopy of a laboratory photoionized plasma experiment at Z. *Physics of Plasmas*, 21:031203, 2014.

[58] W. H. Press, S. A. Teukolsky, W. T. Vetterling, and B. P. Flannery. *Numerical Recipes in C - The Art of Scientific Computing*, section 15.7. Cambridge University Press, second edition, 2002.

[59] W. H. Press, S. A. Teukolsky, W. T. Vetterling, and B. P. Flannery. *Numerical Recipes in C - The Art of Scientific Computing*, section 15.2. Cambridge University Press, second edition, 2002.